Universidade de Lisboa

Faculdade de Ciências

Departamento de Física

Simulations of an Innovative Time-of-Flight Detector for High-Energy Neutrons

---

Jorge Felizardo Dias Machado

Mestrado em Engenharia Física

2011

UNIVERSIDADE DE LISBOA

FACULDADE DE CIÊNCIAS

DEPARTAMENTO DE FÍSICA

Simulations of an Innovative Time-of-Flight Detector for High-Energy Neutrons

Jorge Felizardo Dias Machado

Mestrado em Engenharia Física

Tese Orientada pelo Doutor

Daniel Galaviz Redondo

2011

"O caos é uma ordem por decifrar."

José Saramago

Agradecimentos

Agradeço a TODOS os que me ajudaram directamente ou indirectamente na realização deste trabalho.

Começo por agradecer ao Doutor Daniel Galaviz, o meu orientador, por ter possibilitado a elaboração deste trabalho, a ajuda e orientação ao longo da realização do mesmo e por me ter permitido fazer várias deslocações possibilitando uma real integração numa colaboração internacional para a construção do detector.

Um agrecidamento especial para o grupo do LIP-Coimbra, ao Professor Doutor Paulo Fonte, ao Professor Doutor Rui Marques, ao Doutor Alberto Blanco e ao Doutor Luís Lopes pelas sugestões, críticas e ajuda na realização do trabalho. Por todo suporte e motivação ao longo de todas as reuniões.

I would like to also acknowledge the NeuLAND Working Group for welcoming me in the collaboration for the development of this innovative detector.

Aos meus colegas de trabalho de trabalho: Ana Henriques, André Ornelas, Micaela Fonseca, Miriam Moreno, Pamela Teubig, Paulo Velho e Pedro Reis pelas muitas vezes em que me ajudaram.

À minha noiva Ana Cunha, por toda a ajuda e motivação. Pela compreensão de alguma ausência da minha parte no decorrer deste trabalho.

A minha família, nomeadamente aos meus pais, Fernando Machado e Ana Maria Machado, por todo o apoio prestado ao longo, não só da dissertação, mas de toda a minha vida.

Aos meus amigos em casa, Cunhadita, Billy e à recém chegada Ariana pelo apoio e muitas vezes ajuda.

A todos os meus amigos, Caeli Gobbato, Catarina Fernandes, Tiago Robalo, Marta Mimoso, Sílvia Barros, Nuno Lima e Rui Caldeira por me tirarem de casa quando mais precisava.

Este trabalho não teria sido possível sem suporte de algumas instituições. O meu agradecimento ao CFNUL por me ter aceite como colaborador, ao Departamento de Física da FCUL por me ter aceite como aluno e à FCT por ter financiado este projecto de investigação.

Abstract

The FAIR (Facility for Antiprotons and Ions Research), a greater improvement compared to current accelerators of the GSI Helmholtz Centre for Heavy Ion Research in Darmstadt, Germany, will become the largest accelerator for nuclear physics in Europe and one of the largest in the world. Among the experiments planned for FAIR, the R^3B *(Reactions with Relativistic Radioactive Beams) collaboration seeks to explain the nuclear properties of unstable nuclei located within the limits of nuclear matter, the so-called "drip-lines". From the consideration of the physics cases to be studied at* R^3B*, the detection of high energy neutrons is essential for the measurement of the many reactions to be observed. A high-resolution neutron ToF spectrometer is required to determine the momentum of high-energy neutrons resulting from the decay of the projectile with energies in the range of 200 MeV to 1000 MeV. One of the concepts for the neutron detector NeuLAND was based on Resistive Plate Chambers (RPCs). The detection principle of the detector using RPCs relies on the detection of the charged particles created by hadronic showers induced by neutrons on materials. For the optimization of a possible large area detector of* 2×2 m^2 *made with RPCs several simulations were performed using the Virtual Monte Carlo framework FAIRROOT. The detector was design as a structure of single RPCs modules with 5 gas gaps grouped one after another into a total of modules enough to reach an efficiency of one neutron detection higher than 90%. Different materials were studied as converters as well different thickness* *of glass plates with different geometrical configurations. The results of the performed simulations, the evaluation of the full detector performance, and the expected performance of a prototype to be tested at GSI in the spring of 2012 are presented.*

Keywords: Nuclear, High-Energy Neutrons, Simulations, RPCs, FAIR, R^3B, NeuLAND

Resumo

O laboratório FAIR (Facility for Antiprotons and Ions Research), uma actualização dos actuais aceleradores do GSI Helmholtz Centre for Heavy Ion Researchem Darmstadt, Alemanha, vai-se tornar o maior acelerador para a física nuclear na Europa e um dos maiores do mundo. Entre as experiências planeadas para o FAIR, a colaboração R^3B (Reactions with Relativistic Radioactive Beams) procura explicar as propriedades nucleares dos núcleos instáveis localizados dentro dos limites da matéria nuclear, as chamadas "drip-lines". A partir da consideração da física a ser estudada na experiência R^3B, a detecção de neutrões de alta energia é essencial para a medição das muitas reacções que deverão ser observadas. É portanto necessário um espectrómetro ToF de alta resolução para determinar o momento dos neutrões de alta energia resultantes da decomposição do projéctil com energias num intervalo de 200 MeV a 1000 MeV. Um dos conceitos para o detector de neutrões NeuLAND é baseado em RPCs (Resistive Plate Chambers). O princípio de detecção do detector usando RPCs baseia-se na detecção de partículas carregadas criadas por chuveiros hadrónicos induzidos por neutrôes em materiais. Para a optimização de um possível detector de grande área de 2×2 m^2 construído com RPCs, várias simulações foram realizadas utilizando o Virtual Monte Carlo framework FAIR-ROOT. O detector foi desenhado como uma estrutura de módulos de RPCs únicos com 5 gaps de gás agrupados um após o outro num total de módulos suficientes para alcançar uma eficiência de detecção de um neutrão supe-

rior a 90%. Foram estudados diferentes materiais como conversores assim como diferentes espessuras das placas de vidro com diferentes configurações geométricas. Aqui serão apresentados os resultados das simulações realizadas assim como a avaliação do desempenho do detector completo e o desempenho de um protótipo que será testado no GSI, na primavera de 2012.

Palavras chave: Nuclear, Neutrões de Alta Energia, Simulações, RPCs, FAIR, R^3B, NeuLAND

Prologue

This document presents the investigations performed during the R & D phase of the future NeuLAND detector of experiment the R^3B at the FAIR laboratory, regarding one of the concepts initially considered for this detector, based on Resistive Plate Chambers (RPCs). During the evolution of the studies performed, the NeuLAND collaboration, after evaluating pros and cons of the two options considered, decided to conclude the R & D for this detector and submitted a Technical Design Report, proposing the construction of the NeuLAND detector with pure plastic scintillator. The main criterium for this decission was the much better efficiency and resolution in the reconstruction of the momentum of several neutrons hitting simultaneously the detector.

This Thesis work summarizes the results obtained considering an alternative concept for the RPC option. It does not intend to become an alterantive to the results presented in the TDR, subscribed by both the author of this Thesis and his supervisor.

Contents

List of Figures

List of Tables

Glossary

ALADIN	**A** **L**arge **DI**pole mag**N**et
ALICE	**A** **L**arge **I**on **C**ollider **E**xperiment
CBM	**C**ompressed **B**aryonic **M**atter
CD	**C**oulomb **D**issociation
ENDF	**E**valuated **N**uclear **D**ata **F**ile
ESR	**E**xperimental **S**torage **R**ing
FAIR	**F**acility for **A**ntiproton and **I**on **R**esearch
FRIB	**F**acility for **R**are **I**sotope **B**eams
FRS	**FR**agment **S**eparator
FWHM	**F**ull **W**idth at **H**alf **M**aximum
GEANT	**GE**ometry **AN**d **T**racking
GFI	**G**rosse **F**iber **D**etector
GINC	**G**eneralized **I**ntra-**N**uclear **C**ascade
GSI	GSI Helmholtzzentrum für Schwerionenforschung GmbH
HV	**H**igh **V**oltage
LAND	**L**arge **A**rea-**N**eutron **D**etector
LIP	**L**aboratório de **I**nstrumentação e Física Experimental de **P**artículas
MIP	**M**inimum **I**Ionizing **P**article
PMT	**P**hoto**M**ul**T**iplier
PPAC	**P**arallel **P**late**A**valanche **C**hamber
PSP	**P**osition **S**ensitive **P**in diode
R^{3}B	**R**eactions with **R**elativistic **R**adioactive **B**eams
RIBF	**R**adioactive **I**on **B**eam **F**actory

ROLU	**R**echts, **O**ben, **L**inks, **U**nten
RPC	**R**esistive **P**late **C**hamber
SIS18	**S**chwer**I**onen **S**ynchrotron
TFW	**T**o**F** **W**all
ToF	**T**Time-o**F**-**F**light
tRPC	**t**iming **RPC**
VMC	**V**irtual **M**onte **C**arlo

1

Introduction

FAIR (Facility for Antiproton and Ion Research) [FAI-web], a greater upgrade of the present GSI (GSI Helmholtz Centre for Heavy Ion Research GmbH) [GSI-web] in Darmstadt, Germany, will become the largest accelerator for nuclear physics in Europe and one of the largest in the world, only comparable to RIBF (Radioactive Ion Beam Factory) in Japan and the future FRIB (Facility for Rare Isotope Beams) in the United States of America. Several experiments are planned for FAIR. One of them is the R^{3}B (Reactions with Relativistic Radioactive Beams) experiment which seeks to investigate the nuclear properties of unstable nuclei located within the limits of nuclear matter, the so-called “drip-lines”. It is expected that the information acquired from the experimental setup will answer many open questions in the fields of Nuclear Physics and Nuclear Astrophysics, and thus performing frontier research at the limits of matter.

The detection of high-energy neutrons is essential to measured many of the reactions that will be performed in the R^{3}B setup. Particularly, all the processes that depend on the reconstruction of the excitation energy trough the invariant mass analysis required accurate measurements of the linear momentum of the ejected neutrons from the projectile. It is planned therefore to install a new Time-of-Flight detector, the NeuLAND detector, to accurately measure neutrons with energies between 200 and 1000 MeV, which is the subject of study of this research work.

1.1 GSI

The GSI Helmholtz Centre for Heavy Ion Research GmbH [GSI-web] is located in the Wixhausen suburb of Darmstadt, Germany. It is a federally and state co-funded heavy ion research center. The scientific research conducted at GSI aims at a better understanding of the structure and behavior of the nuclei. A schematic picture of the facility is presented on the left side of Figure 1.1. GSI operates a unique large-scale accelerator for heavy ions. It is possible to prepare ion beams of all elements up to uranium and accelerate them to a significant fraction of the speed of light.

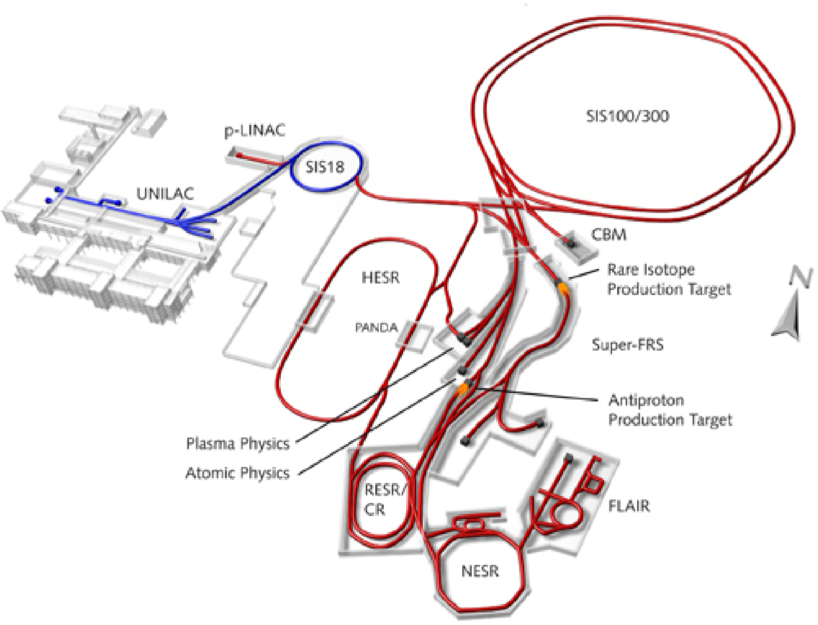

Figure 1.1: Schematic picture of the GSI and FAIR facilities.

A primary beam is generated by ion sources at the left most side of the complex. The beam is injected in the 120 m linear accelerator (UNILAC), where the ions are accelerated up to 20 percent of the speed of light. The beam is then injected in the

GSI synchrotron, the SIS18 (SchwerIonen Synchrotron), where it is further accelerated. After that, shooting the primary beam is extracted and guided towards a light target where unstable nuclides are produced via in-flight fragmentation, and selected in the magnetic spectrometer FRS (FRagment Separator) [FRS-web]. The secondary beams are delivered to several experimental setups (Cave A, B and C) and also to the ESR (Experimental Storage Ring) [GSI-web, FRS-web].The relativistic radioactive beams are used to study the properties of unstable nuclides and to perform nuclear reactions that give insight into the fundamental properties of nuclear matter and nuclear force. These reactions are also essential in astrophysics, since they are expected to take place in stars and exploding stellar environments such as supernovae.

1.2 FAIR

FAIR [FAI-web] is an update of the GSI facility, in which much higher intensities and velocities of secondary beams will be achieved mainly due to a more efficient magnetic spectrometer, the Super-FRS [SUP-web].

State of the art technological concepts will enable the construction of a better, multipurpose accelerator facility. Its core, a double-ring accelerator (SIS100 heavy ion synchrotron) with a circumference of 1100 meters, will be associated with a complex system of cooler and storage rings and experimental setups. The synchrotron will deliver ion beams of unprecedented intensities and energies. Thus also intensive secondary beams can be produced, providing antiprotons and exotic nuclei for groundbreaking experiments. A schematic picture is presented on the right side of Figure 1.1. The whole project is characterized by many technological innovations. This justifies expectations for brilliant beam properties with: higher beam intensities, brilliant beam quality, higher beam energies, higher beam power and a parallel operation [FAI-web].

With this improvement, the existing experimental setups have also to be updated.

The development and construction of new detectors at all experimental setups is on course.

1.3 The Large Area Neutron Detector LAND

The Large Area Neutron Detector (LAND) is a high-efficiency neutron Time-of-Flight detector, designed to measured neutrons with energies ranging from 100 to 1000 MeV [BLAI-92]. The detector is presently located at end of the LAND setup at cave C at GSI. A schematic view of the setup is shown in Figure 1.2. A photograph of the detector is shown in Figure 1.3.

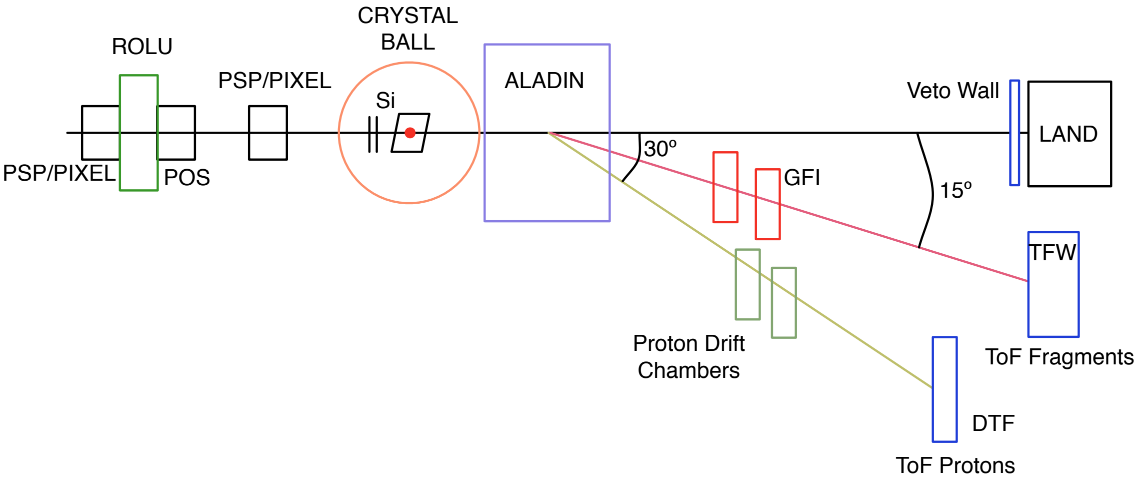

Figure 1.2: Schematic drawing of the ALADIN-LAND setup. This setups aims to measure energies, positions and Time-of-Flight of all particles present in the reactions. The LAND detector is located after the ALADIN dipole magnet.

The detection principle of LAND is based on a sandwich structure of alternating layers of Fe converter material and plastic scintillators. The high-energy neutrons induce nuclear reactions in the converter material producing charged particles subsequently detected by the scintillator. A schematic drawing of the detector is shown in Figure 1.4. The detector has a modular structure. It is structured in 10 planes, build of 20 *paddles* each covering an active area of 2×2 m^2. A paddle is the basic detector unit

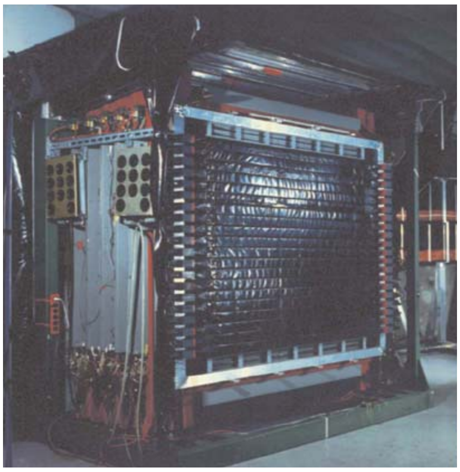

Figure 1.3: Photograph of the Land Detector.

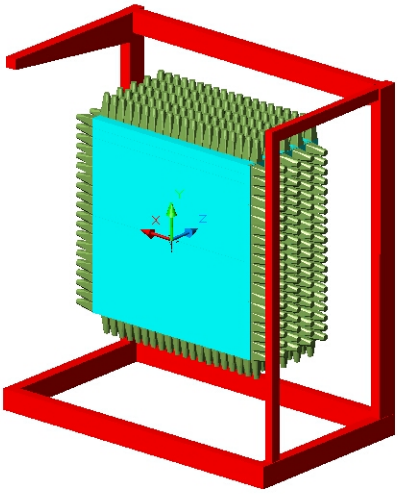

Figure 1.4: Schematic drawing of LAND.

(shown in Figure 1.5), with 10 × 10 × 200 cm^3 active dimensions. Single sheets of scintillator and of iron (5 mm thickness) are alternated to build the paddle structure. All sheets of scintillator belonging to a single paddle are couple at both ends to photomultiplier tubes. Paddles in the consecutive planes are arranged perpendicularly to each other. When a paddle is hit, the position along the paddle is provided by the time difference of the signals measured by the two PM tubes, while the other two positions are defined by the absolute position of the paddle in the detector.

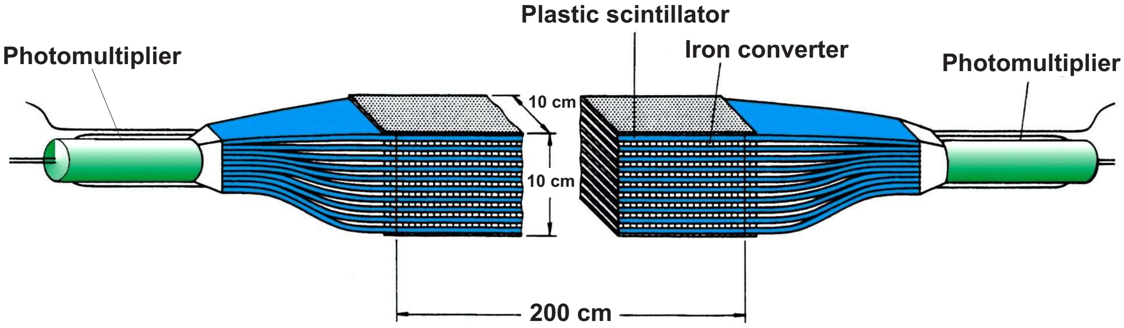

Figure 1.5: Details of construction of a single paddle of the LAND detector.

The depth of 1 m corresponds to about 3 neutron interaction lengths and results in efficiencies of more than 90% for neutrons with kinetic energies above 400 MeV, as shown in Figure 1.6. The optimally working LAND presents a time resolution of $\sigma t \approx 250$ ps and a position resolution of $\sigma_{x,y,z} = 3$ cm.

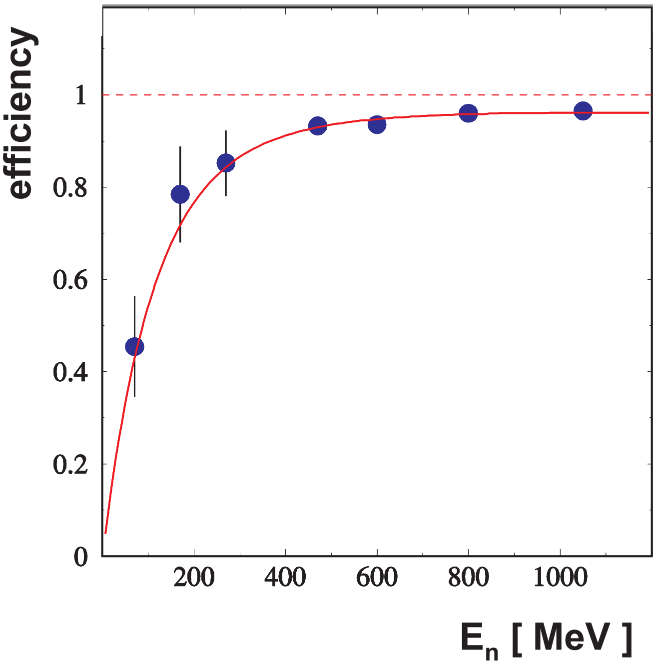

Figure 1.6: Intrinsic efficiency of the LAND detector in function of kinetic energy of the neutron. Figure from [NEU-rep].

1.4 The R^3B experimental setup

The R^3B experience will be part of the FAIR update at GSI, under part of the *high-energy branch*. It is based on a concept similar to the existing LAND experimental setup at the GSI [R3B-web]. As already mentioned, secondary beams of higher energy and intensities will be available at FAIR. The R^3B experiment presents a substantial improvement compared to the current LAND setup respecting in terms of efficiency and resolution. Additional detectors are foreseen for the detection of light recoil particles and for the tracking of heavy-ion trajectories and precise momentum measurements. In Figure 1.7 we can see a scheme of the expected R^3B setup and the involved detectors.

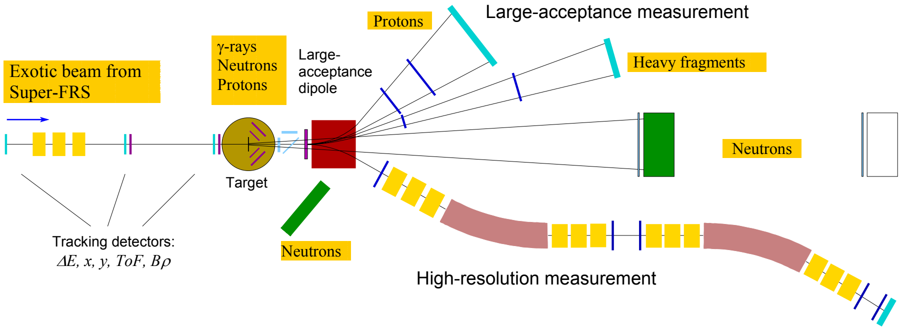

Figure 1.7: Schematic drawing of the R^{3}B experimental setup comprising γ-ray and target recoil detection, a large-acceptance dipole magnet, a high-resolution magnetic spectrometer, neutron and light-charged particle detectors, and a variety of heavy-ion detectors.

During the past decade it has been demonstrated that reactions with high-energy secondary beams are an important tool to explore properties of nuclei, which allows detailed spectroscopic information to be extracted. R^{3}B will cover experimental reaction studies with exotic nuclei far off stability, with emphasis on nuclear structure and dynamics. Astrophysical aspects and technical applications are also in the scientific program. A survey of reaction types and associated physics goals that can be achieved at R^{3}B [R3B-05] is given in Table 1.1.

In order to reach these goals, several detectors and instruments have to be developed and constructed.

Table 1.1: Reaction types with high-energy beams foreseen at R^3B and the corresponding achievable information

Reaction type	Physics Goals
Knockout	Shell structure, valence-nucleon wave function, many-particle decay channels unbound states, nuclear resonances beyond the drip lines
Quasi-free Scatering	Single-particle spectral functions, shell-occupation probabilities, nucleon-nucleon correlations, cluster structures
Total-absorption measurements	Nuclear matter radii, halo and skin structures
Elastic proton scattering	Nuclear matter densities, halo and skin structures
Heavy-ion induced electromagnetic excitation	Low-lying transition strength, single-particle structure, astrophysical S factor, soft coherent modes, low-lying resonances in the continuum, giant dipole (quadrupole) strength
Charge-exchange reactions	Gamow-Teller strength, soft excitation modes, spin-dipole resonance, neutron skin thickness
Fission	Shell structure, dynamical properties
Spallation	Reaction mechanism, astrophysics, applications: nuclear-waste transmutation, neutron spallation sources
Projectile fragmentation and multifragmentation	Equation-of-state, thermal instabilities, structural phenomena in excited nuclei

1.5 The future NeuLAND detector for the R^3B experiment

From the consideration of the physics cases to be studied at R^3B, a high-resolution neutron ToF spectrometer is required to determine the momentum of high-energy neutrons resulting from the decay of the projectile with energies in the range of 200 MeV to 1000 MeV.

1.5.1 Design Goals

The design goals of NeuLAND have been chosen to match the momentum resolution of the charged fragments of $\Delta p/p \approx 10^-3$ [R3B-05]. To achieve this momentum resolution a time resolution of $\sigma_t < 100$ ps and a position resolution of $\sigma_{x,y,z} \approx 1$ cm for flight paths in the range from 10 to 35 m is require.

The Time-of-Flight and positions resolutions given above will result in a energy resolution of about 20 keV at excitation energy of 100 keV above the threshold if the detector is placed at 30 m from the target for a medium-mass nucleus with an incoming energy of 500 AMeV [NEU-rep]. The active area of the detector will remain the same as the LAND detector, 2×2 m^2 which will result in the maximum geometrical acceptance of ±80 mrad at 12.5 m from the target as defined by the gap of the large-acceptance dipole. NeuLAND should also have an efficiency for one-neutron detection $\epsilon > 90\%$ and be capable of resolving up to 5 neutrons per event and reconstruct their momenta correctly [R3B-05].

There were two major detector concepts for NeuLAND, based on scintillation material and on Resistive Plate Chambers (RPC). The RPC concept is very attractive from the cost point, since this type of detector is based on common materials. Since RPCs are used for the detection of charged particles, usually minimum ionizing particles (MIPs), meaning that will be required an effort in R&D to detect hight-energy neutron with RPCs.

Once the RPC concept of the NeuLAND is the subject of this work, it will be further described (see section 3.3) the NeuLAND concept based on RPCs.

2

The physics of the neutron

Before entering in a detailed explanation of the NeuLAND detector, let's first have a look at the physics of the neutron.

2.1 The neutron

The neutron is a subatomic particle with no net electric charge and a mass slightly larger than that of the proton. Nuclei of atoms consist of protons and neutrons, which are therefore collectively referred to as nucleons. The neutron was discovery by James Chadwick in 1932 [CHA-32], although it was theoretically predicted in 1920 by Ernest Rutherford.

2.2 Intrinsic properties

A neutron consists in three quarks, two down quarks with charge $-1/3\,e$ and one up quark with charge $+2/3e$. The quark structure of the neutron is presented in Figure 2.1.

While bound neutrons in stable nuclei are stable, free neutrons are unstable. The only possible decay mode without a change of baryon number is for one of the quarks

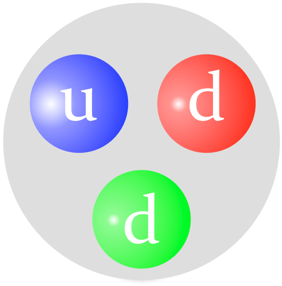

Figure 2.1: The quark structure of the neutron.

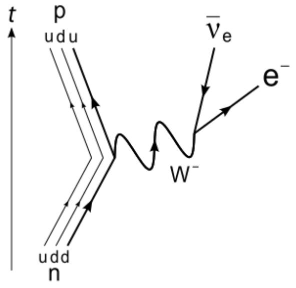

Figure 2.2: The Feynman diagram for beta decay of a neutron into a proton, electron, and electron antineutrino via an intermediate heavy W boson.

to change flavour via the weak interaction. This process is the so-called β^--decay. In Figure 2.2 is presented the Feynman diagram for decay of a neutron. Free neutrons decays into an electron and an electron antineutrino to become a proton by [YAO-06b] with a mean lifetime of about 14 minutes and 46 seconds [YAO-06a]:

$$n^0 \rightarrow p^+ + e^- + \bar{\nu}_e \tag{2.1}$$

2.3 Neutron Sources

As mentioned above, free neutrons are unstable. Therefor they can be obtained only from nuclear disintegrations, nuclear reactions, and high-energy reactions.

- Nuclear reactors are the most copious sources of neutrons. The energy of the neutrons runs between a few keV and more than 10 MeV with a mean energy of 2 MeV. Whit research reactors we can make use of a neutron beam with a large energy spectrum.

- Nuclear reactions are used as well to obtain monoenergetic neutron beams. For example, we can produce neutrons by accelerating deuterons striking on a tritium target in the reaction

$$ {}_{1}^{2}H +_{1}^{3} H \rightarrow_{2}^{4} He +_{0}^{1} n \tag{2.2} $$

and selecting a certain angle for the neutron.

When aiming monoenergetic neutrons by means of nuclear reactions, it is common to use light materials as targets combined with proton or deuteron beams, avoiding the population of resonances in the compound nucleus. Table 2.1 lists a few important reactions used to obtain monoenergetic neutron beams [TUR-07].

Table 2.1: Reactions Used to Produce Monoenergetic Neutrons with Accelerated Protons (p) and Deuterons (d) and the respective Q value

Source	**Q Value (MeV)**
${}^{3}H(d,n)^{4}He$	17.6
${}^{2}H(d,n)^{3}He$	3.27
${}^{12}C(d,n)^{13}N$	-0.281
${}^{3}H(p,n)^{3}He$	-0.764
${}^{7}Li(p,n)^{7}Be$	-1.65

- It is also possible to obtain neutrons with an (α, n) reaction. Mixing together an alpha source (usually radium, polonium or plutonium) and a light metal (beryllium or boron) in powder form and encapsulated we can obtain a neutron source [TUR-07]. Neutrons are emitted as a result of (α, n) reactions, such as the following:

$$ {}_{2}^{4}He +_{4}^{9} Be \rightarrow_{6}^{12} C +_{0}^{1} n \tag{2.3} $$

Light metals are used in order to minimize the Coulomb repulsion between the alpha particle and the nucleus. The neutron intensity from such a source dies off with the half-life of the alpha emitter. Neutrons leave the source with a continuos energy spectrum. Table 2.2 lists some (α, n) neutron sources [TUR-07].

Table 2.2: Examples of (α, n) Neutron Sources.

Source	**Average Neutron Energy (MeV)**	**Half-life**
$^{210}Po\,^{9}Be$	4.2	138 d
$^{210}Po\,^{11}B$	2.5	138 d
$^{226}Ra\,^{9}Be$	3.9	1600 y
$^{226}Ra\,^{11}B$	3.0	1600 y
$^{239}Pu\,^{9}Be$	4.5	24100 y

- Similarly, photoneutron sources, generating neutrons via (γ, n) reactions, are also available. Several examples are shown in Table 2.3. In contrast to (α, n) sources, which emit neutrons with a continuous energy spectrum, monoenergetic photoneutrons can be obtained by selecting a radioactive isotope that emits a single photon.

Table 2.3: Examples of(γ, n) Neutron Sources.

Source	**Neutron Energy (MeV)**	**Half-life**
$^{24}Na\,^{9}Be$	0.97	15 h
$^{24}Na\,^{2}D_2\,^{16}O$	0.26	15 h
$^{116}In\,^{9}Be$	0.38	54 min
$^{124}Sb\,^{9}Be$	0.024	60 d
$^{140}Ra\,^{9}Be$	0.75	40 h

- Some very heavy nuclei fission spontaneously, emitting neutrons in the process. They can be encapsulated and used as neutron sources.

2.4 Classification of Neutrons

As shown above, neutrons can be produced from a variety of nuclear reactions with different energies. They are usually classified according to their energies:

- *Thermal neutrons:* energy of 0.025 eV;
- *"Slow", "intermediate", or "resonance" neutrons:* energies up to 0.01 MeV or 0.1 MeV;
- *Fast neutrons:* energies up to 10 MeV or 20 MeV;
- *Relativistic Neutron:* higher energies.

2.5 Interactions with Matter

Neutrons can interact with matter in different ways. Figure 2.3 shows the types of interaction of neutrons with matter.

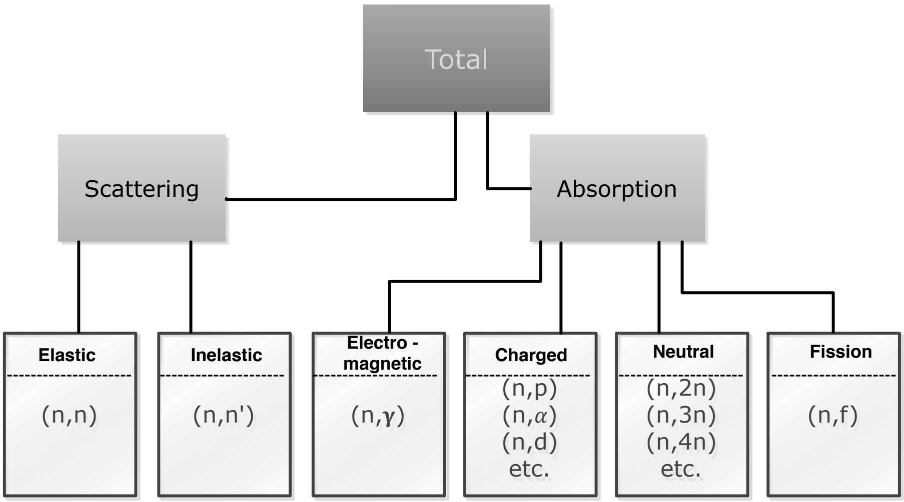

Figure 2.3: Various categories of neutron interaction. The letters represent the incoming particle and outgoing particles.

Since neutrons are neutral particles, they do not electrically interact with the atomic electrons, interacting directly with the nucleus. Thus, they present a high capability of penetration in most materials. As shown in Figure 2.3, the neutrons interact mostly by two process: scattering and absorption.

The scattering process consists in the change of direction after a collision by the neutron with the nucleus and can be of two types:

- *Elastic*: in this collision the nucleus does not suffer any structural change and there is no energy transfer for generation of radiation, the total kinetic energy of the neutron and nucleus is unchanged by the interaction.
- *Inelastic*: inelastic scattering is similar to elastic scattering except that the nucleus undergoes an internal rearrangement into an excited state from which it eventually releases radiation. The total kinetic energy of the outgoing neutron and nucleus is less than the kinetic energy of the incoming neutron.

Instead of being scattered, the neutron can be absorbed or captured. A radioactive emission may follow. As shown in Figure 2.3, the rearrangement of the nucleus may be followed by the emission of several γ rays as well as charged particles. The more common charged particles that can be emitted are protons, deuterons and α particles. Following the interaction, the nucleus may also evaporate several neutrons in the deexcitation process. The emission of just one neutron is indistinguishable from a scattering event.

All the described neutrons interactions have a certain probability to happen. The probability of a particular event occurring between a nucleus and a neutron is expressed by the concept of cross section. Expressed in units of area (1 barn = 10^{-24} cm^2). Each type of event has its own probability and cross section. The sum of all the individuals cross sections gives the total cross section. The cross sections associated with the various interactions described above can be designated by the following notation:

σ_t = total cross section ($\sigma_s + \sigma_a$)

σ_s = total scattering cross section $(\sigma_{el} + \sigma_i)$

σ_{el} or $\sigma_{(n,n)}$ = elastic scattering cross section

σ_i or $\sigma_{(n,n')}$ = inelastic scattering cross section

σ_a or σ_c = absorption or capture cross section

σ_{ne} = nonelastic cross section, $\sigma_t - \sigma_{el}$

$\sigma_{(n,\gamma)}$ = radiative capture cross section

σ_f = fission cross section

$\sigma_{(n,p)}$ = (n, p) reaction cross section

All cross sections described above depend on the neutron energy and on the target nucleus. The magnitude of the cross section depends on the type of reaction (elastic, inelastic) and on the type of interaction associate to the reaction.

The hadronic process associated to the interactions of neutrons with nuclei used in this work are described in section 4.4.

3

RPCs

The *Resistive Plate Chamber* (RPC) is a gaseous avalanche detector and was developed by R. Santonico and R. Carderelli in 1981 [SAN-81]. In this chapter a brief discussion about the evolution of gaseous parallel plate detectors like the RPC as also the inherent detection processes will be given. However, to understand the detection principle of the RPCs is important to describe the physics processes in ionizing gas detectors.

3.1 Physics processes in ionizing gas detectors

In these sections, a brief description of the processes that the different particles interact with the ionizing gas detectors as also the description of the avalanche mechanisms in gases will be given.

3.1.1 Electromagnetic interactions

Most the particles have electric charge and therefore interact electromagnetically. In addition the electromagnetic interaction is well understood.

3.1.1.1 Interactions of heavy charged particles with matter

The interactions of heavy relativistic charged particles are mainly described by the energy loss trough ionizations and excitations in a medium. The average energy loss by per unit length is given by the Bethe-Bloch formula [EID-04]:

$$-\frac{1}{\eta}\frac{dE}{dx} = Kz^2\frac{Z}{A}\frac{1}{\beta^2}\left[\frac{1}{2}\ln\frac{2m_ec^2\beta^2\gamma^2T_{max}}{I^2} - \beta^2\right] \tag{3.1}$$

where m_e is electron mass, z the charge of the incident particle and β its velocity and γ the Lorentz factor. The medium contribution is described by the ratio of its atomic to mass number Z/A, the density η and the mean excitation energy I. The factor K in the equation 3.1 is a constant given by:

$$K = 4\pi\frac{N_A}{m_ec^2}\left(\frac{e^2}{4\pi\epsilon_0}\right) = 0.307075\ MeV\ g^{-1}\ cm^2 \tag{3.2}$$

where e is the electron charge, ϵ_0 the vacuum dielectric constant and N_A de Avogadro's number.

In equation 3.1, T_{max} is defined as the maximum kinetic energy that can be transferred to a single electron:

$$T_{max} = \frac{2m_ec^2\beta^2\gamma^2}{1 + 2\gamma m_e/M + m_e/M^2} \tag{3.3}$$

where M is the mass of the particle.

The total energy loss described by the equation 3.1, can be described however by a sum of the energy loss result from close collisions and the energy loss result from distant collisions.

Distant and close collisions

The atomic differential cross section that a particle with energy E loses an energy between E' and $E' + dE'$ in a collision with an atom is:

$$\left.\frac{d\sigma}{dE'}\right|_{col} \tag{3.4}$$

Therefore, the average number of collisions with an energy loss between E' and $E' + dE'$ per unit length in a material with density η and atomic number A is given by:

$$\eta \frac{N_A}{A} \left.\frac{d\sigma}{dE'}\right|_{col} \tag{3.5}$$

This leads to the average energy loss per length:

$$\left.\frac{dE}{dx}\right|_{col} = \eta \frac{N_A}{A} \int_{E_{min}}^{E_{max}} E' \left.\frac{d\sigma}{dE'}\right|_{col} dE' = \eta \frac{N_A}{A} k \tag{3.6}$$

where k is the energy loss resulting from the collisions. The total energy loss is a sum of the energy loss resulting from distant collisions $k_{b>b_{min}}$ and the energy loss resulting from close collisions $k_{b<b_{min}}$:

$$-\frac{1}{\eta} \left.\frac{dE}{dx}\right|_{col} = \frac{N_A}{A} (k_{b>b_{min}} + k_{b<b_{min}}) \tag{3.7}$$

Distant collisions

Distant collisions take place at large impact parameters ($b > b_{min}$). There is a small transfer of energy and they are responsible for the excitations of the atoms of the medium.

For distant collisions the energy loss is given by:

$$k_{b>b_{min}} = \frac{2\pi Z z^2 r_e^2 m_e c^2}{\beta^2} \left[ln \frac{2 m_e c^2 \beta^2 \gamma^2 \nu}{I^2} - \beta^2 \right] \tag{3.8}$$

valid for charged particles of any kind where ν is the energy release on the collision.

Close collisions

Close collisions take place at small impact parameters ($b < b_{min}$). A large energy is transferred in the interaction. They are responsible for the ionizations in the medium.

The application of principles of conservation of energy and momentum leads to the maximum kinetic energy that can be imparted to a free electron in a collision of a particle, considering however that a close collision of the particle with an atomic electron is not different from a collision between a charged particle and a free electron. Therefore, the energy loss due to close collisions $k_{b<b_{min}}$ is calculated by integration for $\nu << E_{max}$:

$$k_{b<b_{min}} = \int\limits_{\nu}^{E_{max}} E' \left. \frac{d\sigma}{dE'} \right| \tag{3.9}$$

For particles with Spin 0 and mass $m > m_e$ we get:

$$k_{b<b_{min}} = \frac{2\pi Z z^2 r_e^2 m_e c^2}{\beta^2} \left[\ln \frac{E_{max}}{\nu} - \beta^2 \right] \tag{3.10}$$

where r_e is the classic electron radius: $r_e = e^2/4\pi\epsilon_0 m_e c^2$.

The total energy loss for heavy particles given in equation 3.1 is calculated with equations 3.7, 3.8 and 3.10.

The Density Effect

The distant collision contribution to the total energy loss due to ionization and excitation increases for relativistic particles as $\ln(\beta\gamma)$ [HAG-02]. The value of the transverse electric field increases with energy. Thus, materials become polarized and the electric field of the particle is partly screened introducing the density effect correction δ. At relativistic energies δ is given by:

$$\delta = 2\ln(h\omega_p/I) + 2\ln(\beta\gamma) - 1 \tag{3.11}$$

Where $h\omega_p$ is the plasma energy of the medium defined as:

$$h\omega_p/I = \sqrt{4\pi N_e r_e^3}\frac{m_e c^2}{\alpha} \tag{3.12}$$

where N_e is the electron density and α the fine structure constant $\alpha \approx 1/137$. Therefore, with the density effect correction, equation 3.1 becomes:

$$-\frac{1}{\eta}\frac{dE}{dx} = Kz^2\frac{Z}{A}\frac{1}{\beta^2}\left[\frac{1}{2}\ln\frac{2m_e c^2\beta^2\gamma^2 T_{max}}{I^2} - \beta^2 - \frac{\delta}{2}\right] \tag{3.13}$$

In Figure 3.1 is shown the energy loss $-\frac{1}{\eta}\frac{dE}{dX}$ due to ionization and bremsstrahlung for μ^+ in copper as function of $\beta\gamma$.

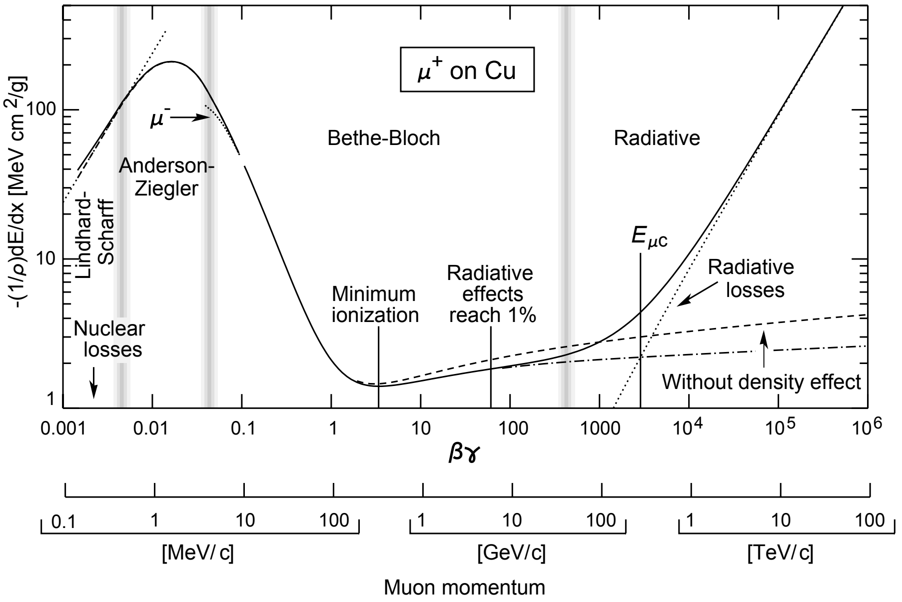

Figure 3.1: Energy loss for μ^+ in cover with nine orders of magnitude in momentum [HAG-02].

For the energy loss by ionization and excitation the curves with and without density effect are shown in Figure 3.1. The critical energy $E_{\mu C}$ is also indicated, where the energy loss due to ionization is equal to the energy loss due to bremsstrahlung. The solid curve indicates the total energy loss which is the sum of the two.

3.1.1.2 Interactions of high energy electrons with matter

Electrons with energy in the range of tenths of MeV start to lose energy via bremsstrahlung. The characteristic distance for this process is the radiation length X_0 defined as the distance over which an electron losses in average $1/e$ of its energy. Approximate formulas for X_0 are given in [GRU-96]. The energy loss by radiation depends strongly on the absorbing material. For each material we can define a critical energy E_c at which the radiation loss equals the ionization loss. For electrons we find that:

in solids

$$E_c = \frac{610\ MeV}{Z + 1.24} \tag{3.14}$$

and for gases

$$E_c = \frac{710\ MeV}{Z + 0.92} \tag{3.15}$$

At hight energies, radiative processes becomes more important than ionization.

3.1.1.3 Interaction of γ photons with matter

The three more relevant manners that photons interact with matter are the following:

1. *Photoelectric effect:* at energies comparable to the binding energies of the electrons in the atom, the photon will transfer all its energy which will result in a ejected electron with equal energy of the photon minus the binding energy:

$$E_e = h\nu - K \tag{3.16}$$

where K is the binding energy and $h\nu$ the photon energy.

2. *Compton effect:* The interaction of a photon with a free electron leads to the Compton effect. The photon transfers a part of its energy and momentum to the electron at rest. The interaction can be evaluated considering the energy and momentum conservation:

$$E_e = \frac{(1-\cos\theta)\frac{h\nu}{m_e c^2}}{1+(1-\cos\theta)(\frac{h\nu}{m_e c^2})} h\nu \tag{3.17}$$

with θ the angle between the photon and the electron after the interaction. The maximum of energy that a photon can transfers to a electrons corresponds to the $\theta = \pi$.

3. *Pair Production:* when a photon exceeds the energy of twice the electron mass ($2m_e \approx 1.022$ MeV) the production of an electron positron pair become energetically possible. The interaction of the photon with the Coulomb field of the nucleus leads to the production of electron-positron pairs. The energy excess over $2m_e$ is shared by booth the particles.

3.1.2 The physics of avalanches in gases

In 1990 Townsend [TOW-10] measured the current between two parallel electrodes while a small numbers of electrons was resealed from the cathode. He observed an exponential growth of the current with the increase of the applied voltage. This fact was interpreted as the result of a multiplication process originated by the drifting electrons and ions when they achieve the necessary energy to induce further ionizations. This phenomenon has been used to produce measurable signals from a small number of gas ionizations and the term avalanche has became popular for the description of this multiplication cascade.

3.1.2.1 Physics processes

When a charged particle crosses the gas volume the gas can be ionized releasing electrons. These electrons are further multiplied due an applied electric field. During the migration of the released charges towards the electrodes, collisions with the gas molecules may occur. The released ions, due to its low mobility, do not acquire significant energy in the collisions, while the electrons are easily accelerated by the applied electric field and can acquire a significant energy when experience a collision. If the energy of the electron is bigger than the ionization energy of the gas molecules, it is possible that an electron-ion pair is released. The process of multiplication starts and takes a cascade shape (Townsend avalanche) where each released electron can release more electrons by the same precess.

The number of electrons per unit length is governed by the Townsend equation:

$$\frac{dN}{N} = \alpha.dx \tag{3.18}$$

where α is the first Townsend coefficient for the gas. The coefficient is zero for electric field values below the limit and increases with the electric field increase. For a constant electric field, the coefficient α is constant in the Townsend equation and is solution predicts that the electrons density exponentially grows with the distance as the avalanche progresses:

$$N(x) = N_0.e^{\alpha.x} \tag{3.19}$$

3.1.2.2 Energy distributions

A free particle in a gas will lose its energy by multiple collisions until the same thermal distribution of the constituents is reached. The kinetic theory of gases provides the thermal distribution of energy:

$$\frac{dN}{d\epsilon} = \frac{2\sqrt{\epsilon}}{\sqrt{\pi}(kT)^{3/2}} e^{-\epsilon/kT} \tag{3.20}$$

with an average energy $\bar{\epsilon} = 3/2kT \approx 0.04$ eV under normal conditions (T≈25°C).

With an external field applied, the energy distribution is a compromise between the average energy lost by collisions and the mean free path of the particle where the particle regained energy.

The ions released by the gas ionized are fast thermalized even in the presence of very high electric fields. For the electrons is a complete different situation, They are both numerical [PAL-75] and analytic [SCH-78] descriptions based on the kinetic theory of gases.

3.1.2.3 Drift velocities and Diffusion

When the charge carriers are under the effect of an electric field they migrate in the direction of the electrodes. The drift velocity results from the average over the distribution of possible energies:

$$v_{e(i)} = \int \cos\theta \sqrt{\frac{2\epsilon}{m_{e(i)}}} \frac{1}{2\pi} \frac{dN}{d\epsilon} d\cos\theta \tag{3.21}$$

where θ is the angle between the particle velocity and the direction of the electric field. In the presence of high electric field the expression 3.21 can be written as [SAU-77]:

$$v_{e(i)} = \frac{2}{3} \frac{eE}{m_{e(i)}} \int \epsilon \lambda_e(\epsilon) \frac{\partial \left(\sqrt{\frac{m_{e(i)}}{2\epsilon}} \frac{dN_0}{d\epsilon} \right)}{\partial \epsilon} d\epsilon \tag{3.22}$$

where $\frac{dN_0}{d\epsilon}$ is the energy distribution in the absence of electric fields.

Expression 3.22 can be analytically solved assuming a constant value for the mean free path λ_e and a thermal distribution:

$$v_{e(i)} = \frac{2}{3}\sqrt{\frac{m_{e(i)e^2}}{2kT}}\lambda_e E = \mu_{e(i)} E \tag{3.23}$$

where $\mu_{e(i)}$ is defined as the electronic (or ionic) mobility.

Due to a larger mass, the ions have drift speeds about 1000 times lower than those presented by electrons under the same conditions.

Superimposed on the drift speed of carriers due to the electric field is the thermal motion in all directions. The greater the distance to go before reaching the anode, the more the electrons that will suffer diffusion.

If we assume that at a distance x a cluster of N_0 particles is located, they will diffuse by multiple collisions expressed in one dimensional medium by:

$$\frac{dN}{dx} = \frac{N_0}{\sqrt{4\pi Dt}} e^{-x^2/4Dt} \tag{3.24}$$

Which is a Gaussian distribution whose width is going to increase with time as $\sqrt{2Dt}$. The parameter D is the diffusion coefficient which governs the diffusion process. The diffusion coefficient can be obtained by the kinetic theory of gases[PAL-75] as:

$$D = \frac{1}{3}\int \lambda_e(\epsilon)\sqrt{\frac{2\epsilon}{m}}\frac{dN}{d\epsilon}d\epsilon \tag{3.25}$$

3.1.2.4 Avalanche propagation

The equations for the progression of densities of electrons and ions with an electric field applied can be described as a function of the parameters v_e, v_i, D_e, D_i and the first Townsend coefficient α as [DAV-73]:

$$\frac{\partial n_e(x,y,z,t)}{\partial t} = \alpha n_e|v_e| - \nabla(n_e v_e) + D_e \nabla^2 n_e \tag{3.26}$$

$$\frac{\partial n_i(x,y,z,t)}{\partial t} = \alpha n_e|v_e| - \nabla(n_i v_i) + D_i \nabla^2 n_i \tag{3.27}$$

Assuming that transversal and longitudinal diffusions coefficients are equal and assuming N_0 electrons released together at instant $t = 0$ from some point in the cathode (actually the electrons are produced between 0 and x independently from each other. Thus, it can be assumed in a first approximation that they are released simultaneously from the origin), the solution of equations 3.26 and 3.27 is given by [MEE-78]:

$$n_e(x,y,z,t) = N_0 e^{\alpha v_e t} \frac{1}{(4\pi D_e t)^3/2} exp(-\frac{x^2+y^2+(z-v_e t)^2}{4 D_e t}) \tag{3.28}$$

Therefore, the average increase in the number of charges in the avalanche can be described, in first approximation, by the Townsend amplification theory:

$$n_e = N_0 e^{\alpha v_e t} \tag{3.29}$$

After collection at the anode, at a distance d from where the avalanche started, the average increase of initial particles is given by $g = e^{\alpha d}$.

3.1.2.5 Avalanche statistics

The number of primary ionizing collisions in a gap of width d follows a Poisson distribution:

$$P(k) = \frac{n_0^k}{k!} e^{-no} \tag{3.30}$$

where the average of the distribution $n_0 = d/\lambda$, being λ the mean free path for the primary particle ionization.

Therefore, there is a stochastic process for the ionizing probability of the electrons (ions) of the avalanche. If the released of charges is very large, this effect will be small. However, this effect becomes important in the early stages of the avalanches (will affect the avalanche gain).

The distributions of gains for avalanches, initiated at a distance d by a single electron is given by the Furry law:

$$\frac{dN}{dg} = \frac{1}{\bar{g}} e^{-g/\bar{g}} \tag{3.31}$$

with $\bar{g} = e^{\alpha d}$ as the average gain.

3.2 Evolution of Parallel Plate Detectors

A Parallel Plate Chamber (PPC) consists in 2 parallel metallic electrodes operated at high voltage providing an uniform electric field in between them. The gap between the plates is filled with gas. The passage of a charged particle in the volume delimited by the 2 electrodes creates electron-ion pairs with a certain density (primary ionization). In a later stage, the released electrons are accelerated towards the anode acquiring sufficient energy for inducing further ionizations in a cascading process called avalanche (a detailed explanation was given in section 3.1.2). In this way it is possible to produce a measurable amount of charge from a few number of initial charges. The very fast drifting electrons create a signal that can be used for timing purposes.

3.2.1 Spark Counter

The first application of a parallel plate geometry for timing dates back to 1948, the so-called Keuffel Spark Counter [KEU-48]. It showed a time resolution of 1 ns by far better than any Geiger-Müller Counters that were commonly used at time (100 ns). This development allowed the construction of accurate timing systems to measure the velocity of fast charged particles.

Spark Counts generally consists of 2 planar electrodes with a high voltage applied. The volume in between them is filled with gas. The passage of charged particles in the gas leaves a trace of free charges in the gas that produces avalanches of charged carriers in the electric field. When a avalanche reaches a certain size they transform into a streamer. A streamer is defined as a state where photons contribute to the spread of free charge carriers. Then, a conducting plasma filament connecting the two electrodes is formed. Through this channel the electrodes are discharged creating a spark. The fast voltage signal created from the rapidly growing anode current can be taken as a time flag for the arrival of the charged particle. In this process is created an enormous amount of charge released by the spark which leads to no need to further amplification. The counting rate of this type of detector is limited by the time that is needed to recharge the electrodes. The recovery time needed by the detector is typically some milliseconds.

To overcome the limited count rate, in 1971 [PAR-71] a new type of spark counter operated with electrodes covered by high resistivity materials (glass) was developed. With resistive plate electrodes the voltage breakdown was prevented ,i.e., the resistivity of around 10^9 Ωcm of the electrodes leads to a limitation of the discharge to the area around the primary avalanche. Because the high voltage drops only locally, the detector is still sensitive to particles in the remaining area. The Pestov Spark Counter has achieved a time resolution down to 25 ps [PES-98] with a 0.1 mm gass gap. However, this detector have a high technical complexity; a very small gas gap combined with high values of electric field and the large overpressure of 12 bar required for high efficiency makes the mechanical requirements very demanding.

3.2.2 Parallel Plate Avalanche Chambers

A Parallel Plate Avalanche Chamber (PPAC) is a single gap gaseous detector. This type of detector is very similar to the Spark Counters, but in contrast to them the PPAC is operated in avalanche mode avoiding discharges. It commonly consists of two planar metallic electrodes. Its advantages are the fast response and increased rate capability [AKI-94]. However, the signals are very small [CHA-91] which gives a low signal-to-noise ratio. A low signal leaves to use a low noise and very sensitive electronics which contradicts with the fast rise time needed for timing purposes.

3.2.3 Resistive Plate Chambers

As mentioned, the RPCs were first developed by R. Santonico and R. Carderelli in 1981. Similar to the Spark Counter and the PPAC, the RPC consists of two parallel plate electrodes. The first RPC had 2 copper electrodes covered with high resistance plates made of Bakelite. In Figure 3.2 a schematic drawing of the compounds of the first RPC is shown. With a sensitive area of 85×13 cm ^{2} and a gap of 1.5 mm filled with a gas mixture Argon/iso-C_4H_{10} (iso-butane) in a proportion 1:1, the detector was operated in stream mode and the gas circulate at atmospheric pressure.

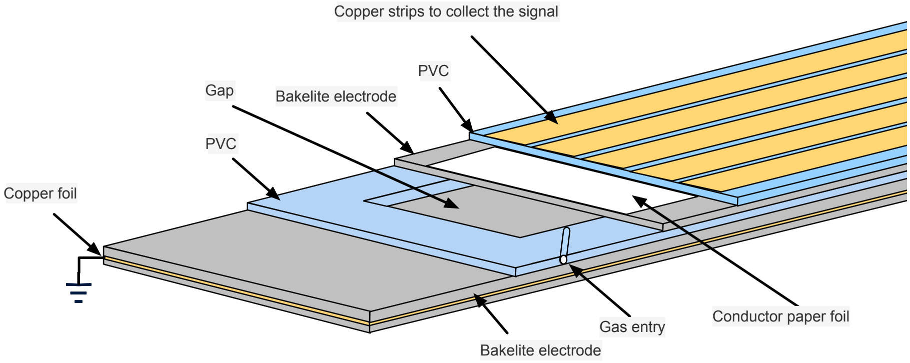

Figure 3.2: Schematic drawing of the first RPC

This design has achieved a 97% efficiency and a time distribution of 1.2 ns FWHM.

From this moment on, the RPCs entered in a continuous state of evolution, the achievement of these performance made the RPCs an alternative to plastic scintillators.

3.2.4 Double gap RPC

The double gap geometry was introduced in 1988 [CAR-88] with an increase of the gap for 2 mm. In Figure 3.3 a schematic illustration of the double gap RPC can be seen. It had a symmetric geometry with the ground electrode in the center and HV applied over the out layers. This detector had a increase in the efficiency and time resolutions similar to the one gap RPC.

3.2.5 Operation modes

The RPC can be operated in two different modes, streamer mode (discharge mode) or avalanche mode. In avalanche mode, after the release of primary charge by the incoming ionizing radiation, it will be generated in the amplification volume a Tonwsend avalanche with the propagation and multiplication of the electrons. If the gas gain is further increased, photons can start to contribute to the propagation of the avalanche and streamers appear. At a later stage, a conductive channel can be formed between the two electrodes, through which the local electrode surfaces are discharged. A spark may be created. In avalanche mode, streamers are unwanted. Streamer mode RPCs make use of the large current induced by the streamers which simplifies the read-out electronics compared to the avalanche mode.

In the stream mode the signals are quite large (between 50 pC and a few nC), there is no need to preamplify the signals and can be discriminated directly. In the avalanche mode we can consider one average charge of 10 pC.

RPCs operated in avalanche mode often use gas mixtures of tetrafluoroethane ($C_2H_2F_4$) with 2% to 5% of isobutane (iso-C_4H_{10}) and with sulfur hexafluoride (SF_6)

with a percentage between 0.4% to 10%. The adition of SF_6 difficult the transition of an Tonwsend avalanche to a streamer, enabling the avalanche mode operation to higher charges. In streamer mode gas mixtures of argon, isobutane and tetrafluoroethane with several proportions are used.

3.2.6 Multi-gap RPC

In 1996 [CER-96] appeared a new design by the M.C.S Williams's group consisting in 3 gaps of 3 mm delimited by bakelite plates (fig. 3.4). According to the developers, this design had a similar time resolution as the single-gap 2 mm chamber and a increase of the efficiency plateau.

One approximation for the efficiency increase can be given by:

$$\epsilon = 1 - (1 - \epsilon_N)^N \tag{3.32}$$

where N denotes the number of gaps and ϵ_N the efficiency per single gap. Assuming that at least one of the gaps must provide a detectable signal with the independence of the others, the expression 3.32 is exact. The time resolution can be given, in a first approximation as:

$$\sigma_T = \frac{\sigma_{T,N}}{\sqrt{N}} \tag{3.33}$$

which is aspected if the time response is Gaussian. However, it was observed that the time resolution improves with the decrease of the gaps width[FON-02]. The multi-gap configuration of a RPC can therefore provide the good time of a narrow RPC and a high efficiency as a characteristic of a wide RPC.

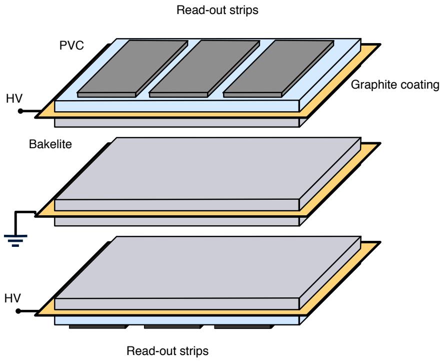

Figure 3.3: Schematic drawing of a symmetric double-gap RPC according it original design.

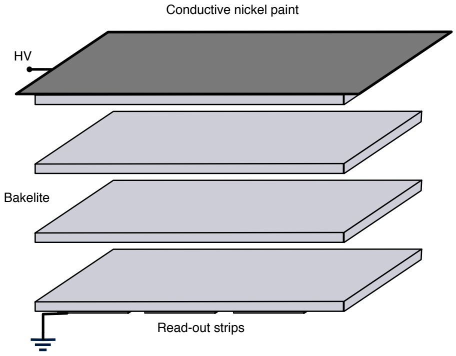

Figure 3.4: Schematic drawing of the 3-gap design according to [CER-96].

3.2.7 Timing RPC

In the year 2000, P. Fonte, A. Smirnitski and M.C.S. Williams [FON-00b] accomplished to operate a multi-gap RPC in avalanche mode with gaps of 300 μm and glass electrodes with a field of 100 kV/cm. This development as achieved a time resolution of 120 ps and was proved the decrease down to 50 ps for small detectors [FON-00a]. The application of this technology in large size tRPCs (timing RPCs) was also been confirmed [BLA-02] with timing resolution below 100 ps. The original gas mixture that was used was $C_2H_2F_4/SF_6$/iso-C_4H_{10} (85/10/5) based on results for wide-gaps RPCs. It seems that the addition of small fraction of SF_6 improve the stability, the efficiency plateau and reduce the amount of streams.

3.2.8 Properties of the tRPC

As the main subject of this work is the simulations of a detector based on tRPCs, in this section will some proprieties be discussed, in particular the ones more important to this work, efficiency and time response.

3.2.8.1 Efficiency

The intrinsic efficiency of an RPC is given by:

$$\epsilon_i = 1 - e^{-d/\lambda} = 1 - e^{-n_0} \tag{3.34}$$

where d is the gap width, λ the mean free path for ionization of the primary particle and n_0 the average number of clusters. The efficiency is directly related to the number of ionization clusters per unit length:

$$\frac{n_0}{d} = \frac{1}{\lambda} \tag{3.35}$$

The theoretical description of the efficiency is bigger than the measured one. There is two main reasons for that: the lowest value achievable for the threshold of the comparator is limited by the noise level and there is always a probability that the electrons in a cluster are attached and no electron signal is collected.

3.2.8.2 Time response

In [BLA-03] a model that uses the the main dependencies of the intrinsic time response of an RPC is available. This model allows to obtain the time response as a function of n'_0 which is related with the measured efficiency and with the growth coefficient $S = (\alpha - \mu)v_e$ where v_e is the drift velocity.

$$\rho_T(t) = \frac{n'_0}{e^{n'_0 - 1}} \frac{e^{(T_{th} - St) - exp(e^{T_{th} - St})}}{\sqrt{n'_0 e^{(T_{th} - St)}}} I_1 \left(2\sqrt{n'_0 e^{(T_{th} - St)}} \right) \tag{3.36}$$

where $T_{th} = \ln[m_t(1 - \mu/\alpha)]$ and I_1 is the modified Bessel function. The rms (Root Minimum Square) can be extracted from equation 3.36 to:

$$rms_T = \frac{K(n'_0)}{S(V)} \tag{3.37}$$

where $K(n'_0)$ has an analytic expansion as a function of n'_0.

3.3 The pre-design of the RPC-based NeuLAND

As already mentioned, it was shown that a large tRPC (160 cm × 10 cm, 2 strip readout) [BLA-02] can provide good time resolutions of $\sigma t \approx 50 - 70$ ps and a position resolution of 1.2 cm along the strips. Besides that, an efficiency of more than 95% for minimum ionizing particles (MIPs) was reached. With those resolutions, efficiencies and a relative low cost when compared to scintillators, RPCs appears to be an very good choice for the detection of the charged particles resulting from the hadronic showers induced by neutrons.

The pre-design of NeuLAND based on RPCs relied on the LAND structure (see section 1.3), a sandwich structure of converter material (iron, tungsten) and RPCs arrays [NEU-rep]. The modular structure of the NeuLAND pre-design is presented in Figure 3.5, one detector plane with 4 modules of 200 × 50 cm^2 each.

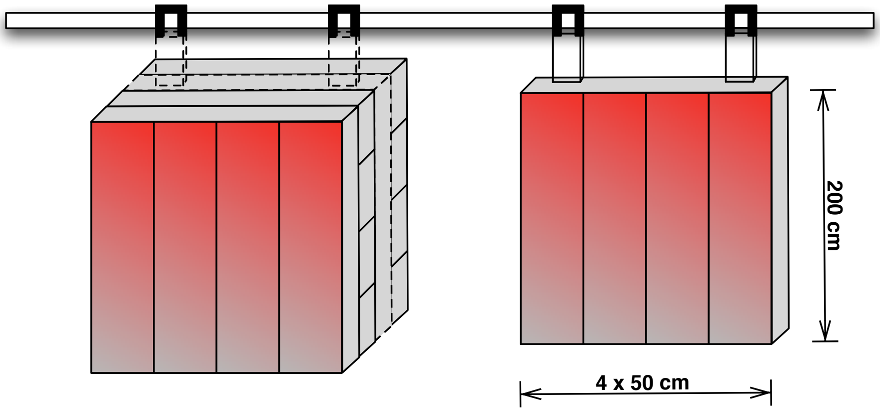

Figure 3.5: Schematic drawing of the modular structure of the NeuLAND detector based in RPCs.

In Figure 3.6 is shown a schematic drawing of a RPC prototype developed at GSI. As it can be observed, the converter material is included in the RPCS structure using 4 mm and 2 mm thick iron plates as anode strips and electrodes, respectively. The area of 200 × 50 cm^2 is subdivided by individual read-out anode strips of approximately 3 cm with and 200 cm length [NEU-rep]. The time signals induced by charged particles produced by hadronic showers are taken from the anode for both far sides of the RPC chambers, thus allowing for mean time information and for position information within the length of the chamber via the time-difference method. The depth of one RPC plane will depend on details of inserted materials and number of gas gaps required. However, with iron as converter material, it will be required about 90 cm of total thickness depth to reach a material depth of more than 3 interactions lengths necessary to reach high efficiency for the detection of neutrons, being the interaction length of about 17.3 cm for iron [R3B-05].

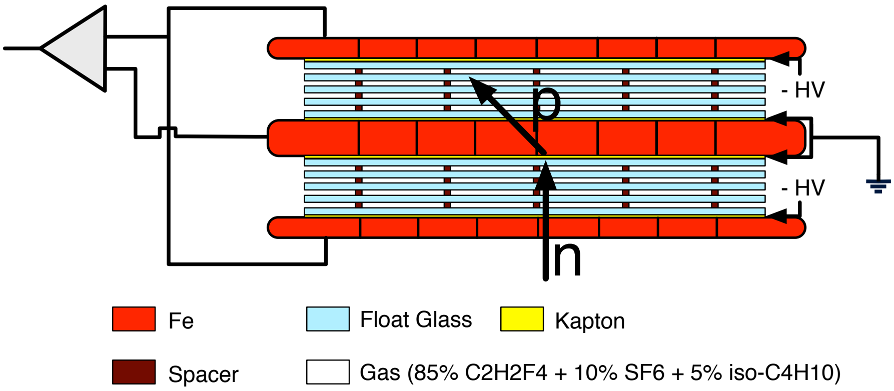

Figure 3.6: Schematic drawing of the pre-design NeuLAND RPC prototype developed at GSI with Fe as converter material.

The main constraint of using RPCs for the design consideration was that RPCs are usually used for the detection of MIPs. One of the open questions was if the excellent timing and efficiency properties of the RPCs would persist for the detection of slower protons resulted from the hadronic showers. To prove the performance of RPCs in this respect an experiment was carried out by the NeuLAND collaboration using existing RPCs from other collaborations exposing them to proton beams of various energies.

This experiment was performed with proton beams at different energies (190 MeV, 120 MeV) at KVI in Groningen (Netherlands). Two different types of RPC were investigated, one from the FOPI collaboration and other provide by the LIP-Coimbra. The FOPI RPC showed a time resolution of ≈ 45 ps (Fig. 3.7) and a efficiency of about

90% [NEU-rep] for all the proton energies used. The LIP-Coimbra RPC showed a time resolution of ≈ 80-100 ps and efficiencies of nearly 100%.

These results proved the feasibility to detect one neutron with the concept of using converter plus RPCs for charged particle detection.

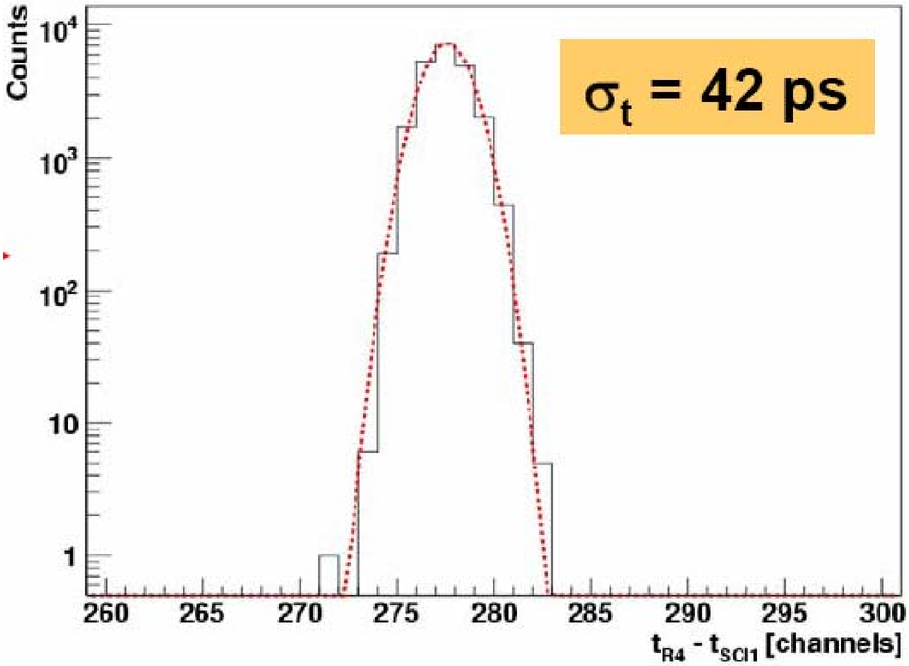

Figure 3.7: Time resolution of a FOPI RPC strip with 120 MeV protons. Figure from Technical status report NeuLAND [NEU-rep].

4

Simulations

In this chapter the frameworks where the simulations were performed, as well as the methods and software packages used will bw described.

Simulations were performed using FairRoot [FAR-web], a Virtual Monte Carlo (VMC) framework developed aatt GSI.

4.1 Virtual Monte Carlo

The concept of VMC was first developed by the ALICE (A Large Ion Collider Experiment) Software project [ALI-web, HRI-03].

With the VMC concept the user Monte Carlo application can be defined independently of a specific transport code (see Fig. 4.1). It can be run with all the supported VMCs without changing the user code for the geometry definition, the detector response of the detector and the input or output formats. The selection of a concrete Monte Carlo transport (GEANT3 [GEA-web], Geant4 [GEA4-web] or Fluka [FLU-web]) is made dynamically at run time.

The VMC is based on the ROOT system [ROO-web], which is used mainly for scripting and dynamical loading of libraries. Once the VMC application has been

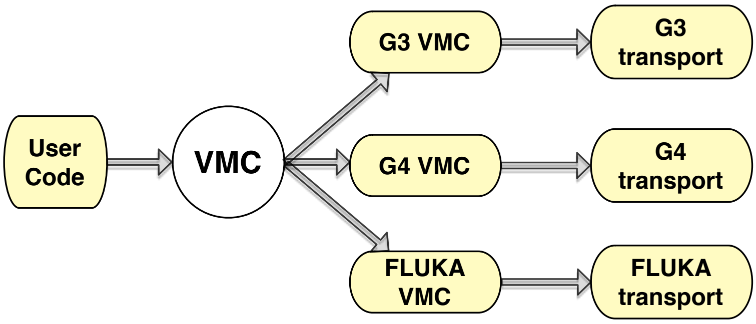

Figure 4.1: The Virtual Monte Carlo concept.

defined, simulations can be run using ROOT macros.

4.2 The FairRoot framework

The FairRoot framework is fully based on the ROOT system and is the simulation, reconstruction and data analysis framework for the FAIR experiments. In Figure 4.2 the different implementations of FairRoot for different experiments of FAIR (CBM, PANDA, R^{3}B) are shown.

The FairRoot base libraries allow users to construct their detectors and analysis tasks in a simple way using a common date structure based on Root Trees as well as the use of a common geometry description based on the ROOT Geometry Modeler. Users can control the functionality of tasks and also the functionality of the whole framework using standard ROOT macros. The main class of the framework is the run manager class which includes methods to set the different [BER-08]:

- input/output files
- primary event generators
- monte carlo transport engines
- material and geometry definition

- magnetic field map definition
- active and inactive detectors
- tasks configuration parameters

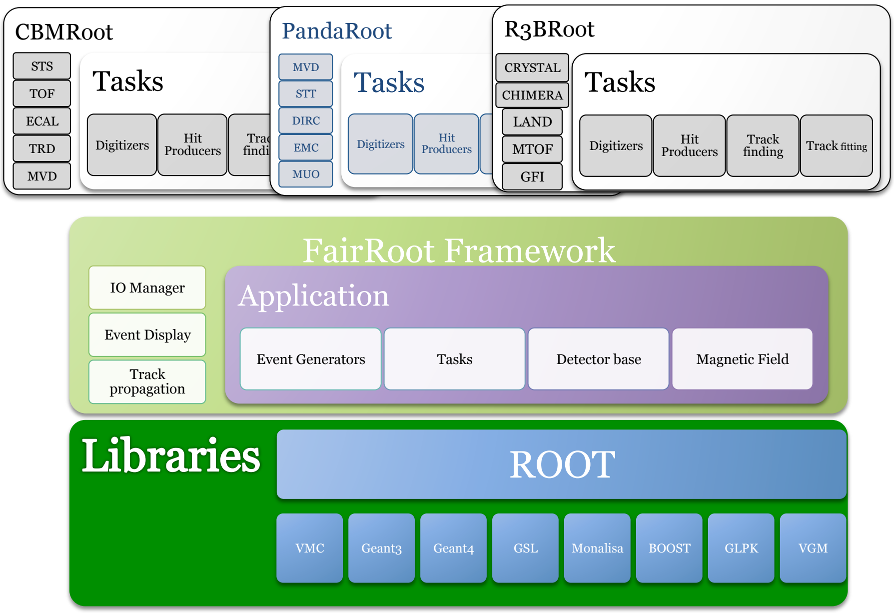

Figure 4.2: Schematic design of FairRoot for different experiments. Figure from [ALT-10].

The FairRoot base classes also provide a generic event display based on Eve and Geane and a track propagation based on Geane.

The FairRoot uses the services of the ROOT VMC to define the actions at each stage of simulation run like the geometry construction and the geometry initialization.

The storage of all information collected by the different sensitive detectors is done event by event bases. The data is storage in ROOT files and organized by the ROOT class TTree.

4.3 The R3BRoot framework

R3BRoot is a ROOT based simulation and analysis framework for the R^{3}B experiment. In Figure 4.3 is represented schematically the structure of the framework. It uses the FairRoot libraries to implement the specific parts needed for the R^{3}B experiment simulation.

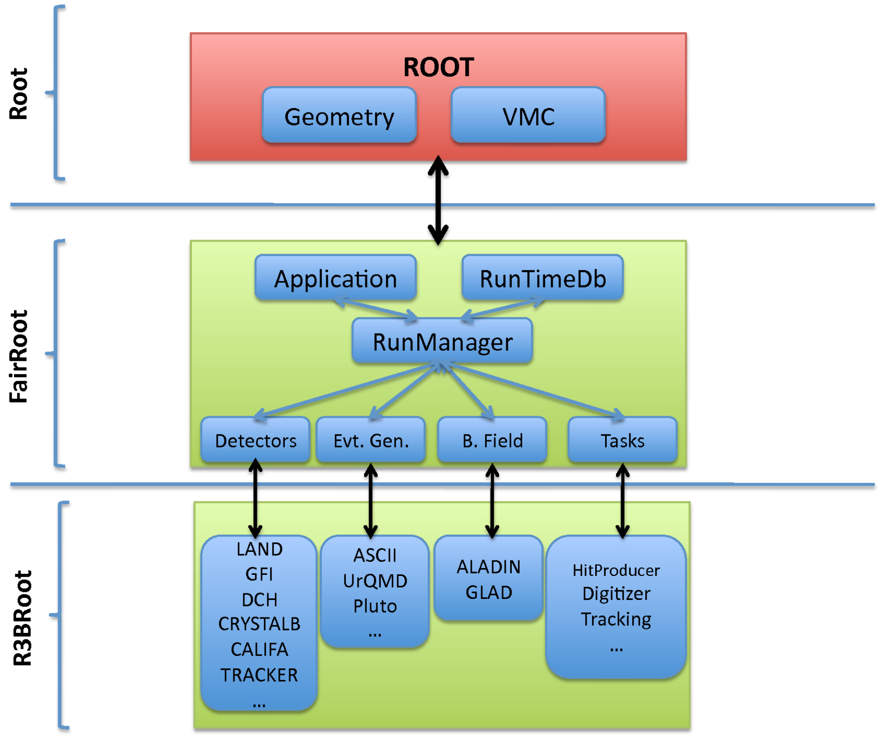

Figure 4.3: Schematic design of the R3BROOT structure based on FairRoot and ROOT libraries. Figure from [BER-09].

The main class *RunManager* handles the overall program flow and the communication between the different modules. The user can choose at runtime which engine, event generator and detectors to use for the simulation. As it can be seen in Figure 4.3, are described several detectors and several event generators. In Figure 4.4 the event display for a simulation of the complete R^{3}B experimental setup is shown.

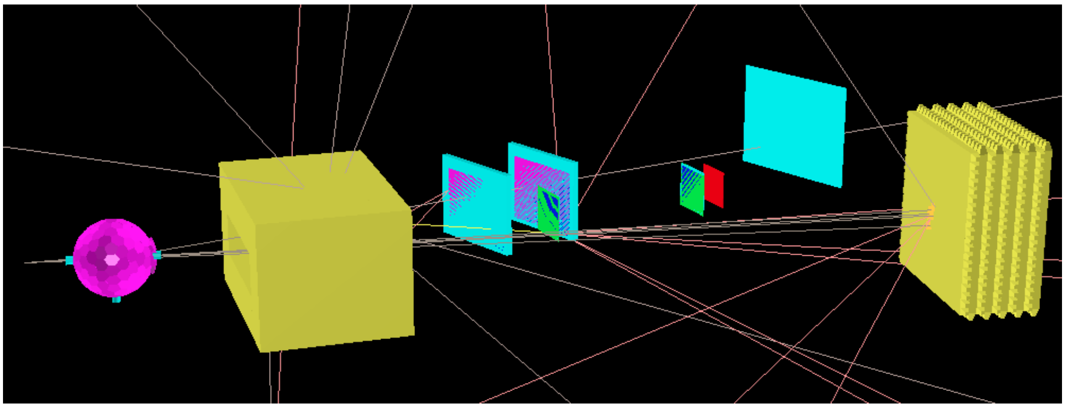

Figure 4.4: Event display of a simulation with all the R^3B experimental setup.

4.4 Hadronic processes

In the simulations performed in this work, the simulation package GCALOR [GCA-web] for hadron interactions was used.

The GCALOR package contains the CALOR [CAL-web] simulator code and a interface to utilize the code in the framework of GEANT. CALOR is a Monte Carlo code system that incorporate several programs to determine the energy and direction of incident hadrons, leptons, and photons. In this way, using GCALOR, the hadronic interaction calculations in the GEANT frame are made by the CALOR code system while the tracking and storing of the particles is done by GEANT. The interface between CALOR and GEANT determines which code to call for the current particle. The material description is automatically extracted from GEANT. GCALOR makes use of the MICAP [JOH-88] code for the simulation of the interaction of neutrons with with nuclide energies below 20 MeV, and uses the FLUKA [BAT-07] simulation code for energies above 20 MeV, since that in GEANT frame FLUKA does not provide information about low energy neutrons.

4.4.1 The low energy neutron code MICAP

The MICAP code has been developed to determine the response of a gas-filled cavity ionization chamber in a mixed neutron and photon radiation environment. The calculation scheme used in MICAP follows individual radiation particles incident on the detector wall material. The incident neutrons produce photons and heavy charged particles and the photons produce electrons and positrons. If these charged particles enter in the detector they will lose energy until they energy is completely deposited or escapes the detector volume. MICAP not only yields the energy deposition by particle type and total energy deposited, but also the particular type reaction.

This program utilizes all currently data in the Evaluated Nuclear Data File (ENDF/B), i.e., partial cross-sections, angular distributions and secondary energy distributions. For very low neutron is used a thermal scattering model based on the free gas model.

4.4.2 The single hadronic interaction code for high energy neutrons FLUKA

The FLUKA hadron-nucleon interaction models are based on resonance production and decay below a few GeV, and on the Dual Parton model [CAP-94] above. For hadron-nucleus interactions two additional models are used. For momenta below 3 GeV/c, the PEANUT includes a very *Generalized Intra-Nuclear Cascade* (GINC) and a pre-equilibrium stage. For high energies, a less sophisticated GINC model is completed by the Gribov-Glauber multiple collision mechanism. Both modules are followed by equilibrium processes: evaporation, fission, Fermi break-up, gamma deexcitation.

4.5 Simulations of the NeuLAND based on RPC

The starting point of all the work performed in simulations was the development of a new class (*R3BNeuLandv1*) by the Dr. Denis Bertini. In this class the geometry of one RPC module (similar as the one shown in Fig. 3.6) was implemented. The RPC implemented in the *R3BNeuLandv1* class had a 40 cm length, 22.1 cm width and 2.54 cm thick. It consisted in a sandwich of RPC and steel plates inside an aluminum case. The steal in the RPC should work as converter material and at the same time as electrode. The central 4 mm of steel were subdivided in 8 anode strips of 2.5 cm width with the same length of the detector separated each oder by a 3 mm gap. In Figure 4.5 is shown the initial geometry of this RPC module.

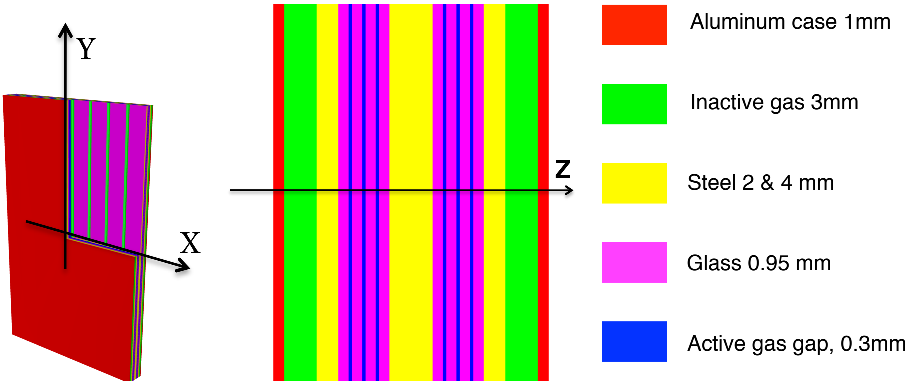

Figure 4.5: Initial geometry of the R3BNeuLandv1 class.

The gas was composed by 84% of Freon, 10% of SF_6 and of 6% Isobutane, the glass (soda-lime glass) was composed by 73% of SiO_2, 14% of Na_2O, 9% of CaO and 4% of MgO and the steel was composed by 71% of Fe, 18% of Cr and 11% of Ni. The composition of the inactive gas was the same as the active gas, it just was defined as active volume the gas between the glass plates.

4.5.1 Geometry definition

The RPC module defined in the *R3BNeuLandv1* was defined according to the initial RPCs requirements and prototypes for the NeuLAND detector, however the size of the module was not the required for a module of the full version of NeuLAND. The full size detector, according to the initial design, would consist of 60 planes of 4 modules with an active area of 50×200 cm^2 (see section 3.3) which does not corresponds to the size of the module implemented. Based on the code already implemented, it was created a RPC module, a single plane with an active area of 200×200 cm^2 (made with 4 modules), and a full size NeuLAND with 60 planes of depth each one rotated 90$^{\mathrm{o}}$ compared to the previous one. With the modifications in the geometry, additional options were implemented for which one of the tree different geometries choose (module, plane or full size) could be chosen, as well as the selection of the converter materials and thickness and the number of planes of the full size detector.

5

Systematic studies of different converter materials

Initially the efficiency of the detector using different materials as converter was evaluated. The motivation for this study were the simulations performed by the NeuLAND collaboration of the LAND detector. The results obtained by this simulations were in very good agreement with experimental data from the LAND detector for booth Monte Carlo engines GEANT3 and GEANT4. It was concluded, through the simulation results, that the main principle of detection by the LAND detector is the elastic scattering of neutrons with the hydrogen in the scintillator material, different from what was believed previously. It also was simulated LAND without iron plates which presented similar results which meant that the iron converters were not necessary. Also, that was concluded that several particles created from the interactions of the neutrons with iron were trapped in the iron plates.

Given these results, it was defined the study of different converter materials with the goal of optimizing the NeuLAND detector constructed with RPCs. Some hydrogen rich materials like paraffin were selected to performed this study.

5.1 Simulations parameters

The results presented in this chapter steam from simulations performed using the following parameters:

- 3000 events
- GEANT3
- 1 neutron per event
- $E_n = 800$ MeV
- Detector placed at 1 m from source
- Open angle: 0 - 2 degrees
- Steel, paraffin and glass as converter materials
- No energy threshold for the efficiency

5.2 Converter material thickness and efficiency

One of the goal design parameters for NeuLAND is the detection efficiency for one neutron $\epsilon > 90\%$. Considering the initial design of the RPC based full-size NeuLAND, with 60 planes and steel as converter material, the dependence of the efficiency on the thickness of the steel plates was studied. The thickness of the steel plates was systematically changed. The converter material thickness in the center of the detector was twice the thickness on both sides of the module, as shown in Figure 5.1.

The variation of the efficiency as a function of the thickness of the steel plates for several configurations of the detector with different number of planes is shown in Figure 5.2.

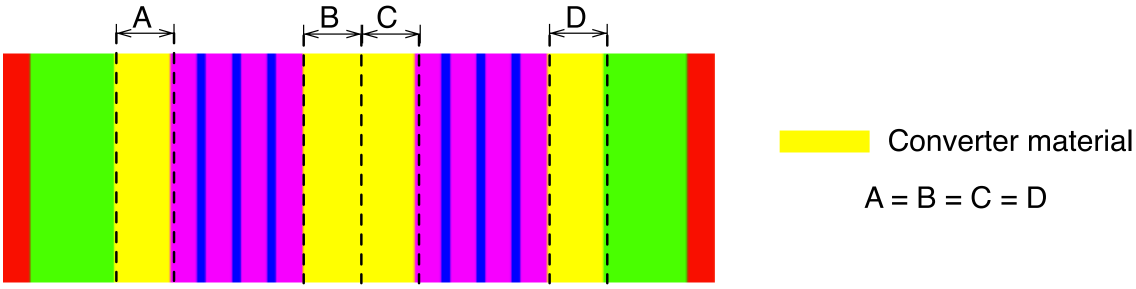

Figure 5.1: Schematic drawing of the RPC. THe thickness of converter material varied in the efficiency study is labeled on the figure.

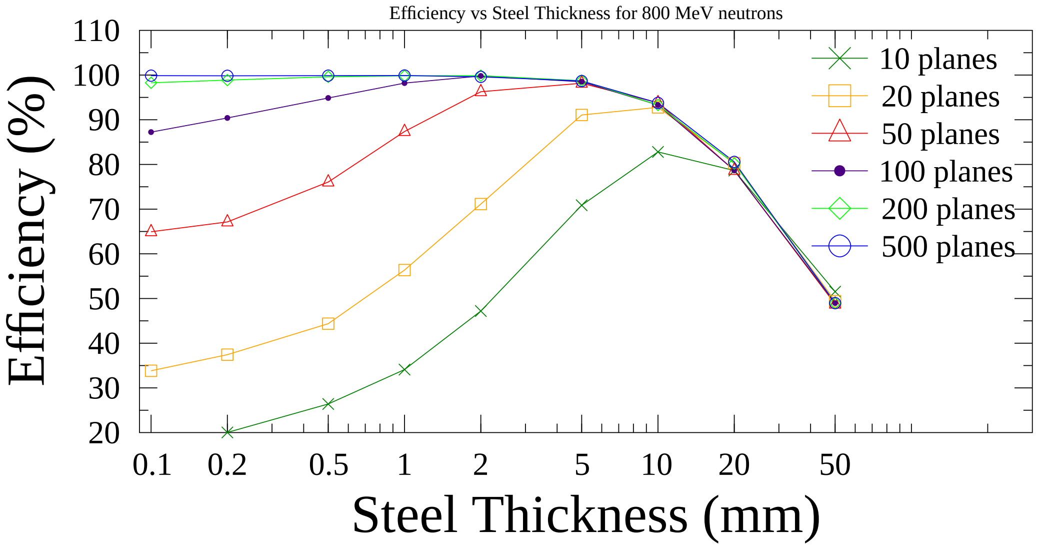

Figure 5.2: Variation of the one neutron detection efficiency as a function of the steel plates thickness for several detector configurations.

As it can be seen in Figure 5.2, all the different configurations reach a maximum of efficiency for a certain steel thickness. Considering a small converter thickness, the efficiency increases with the number of planes. Depending on the detector configuration, there is a certain thickness value for which the efficiency starts dropping, as the particles created in the steel do not have enough energy to scape and reach the RPC gas. Another aspect that we can observe, is that the efficiency does not only depend on the amount of steel. There are several configurations contain the same amount of steel but present different efficiencies for instance for 10 planes and 10 mm steel thickness reaches an efficiency below 85% while the configuration with 50 planes and 2 mm of steel thickness remains above 95%.

A similar study was done using paraffin as converter material, replacing the 3 steel plates by 3 paraffin planes. In Figure 5.3 the variation of the one neutron detection efficiency for several paraffin thicknesses and for different detector configurations is shown.

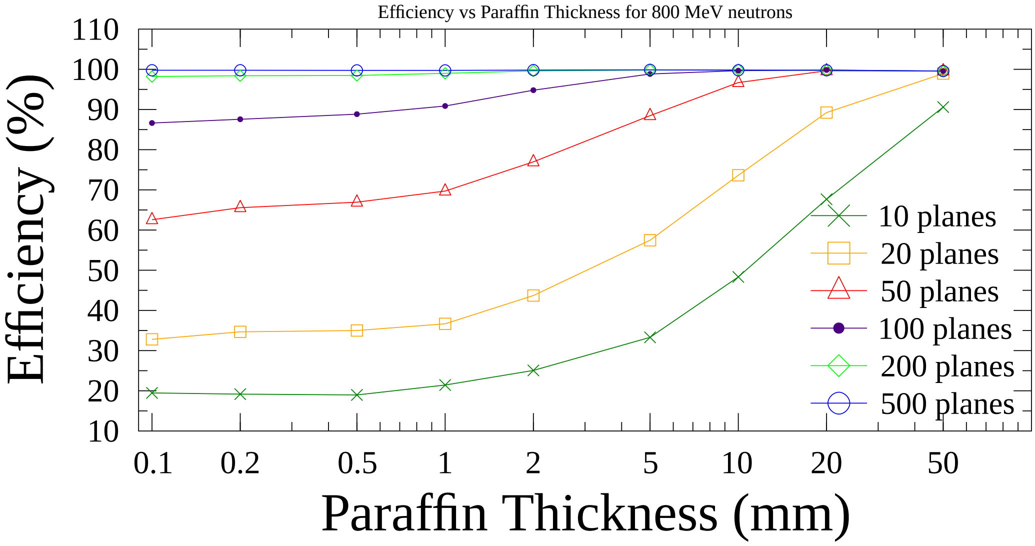

Figure 5.3: Variation of the one neutron detection efficiency as a function of the paraffin plates thickness for several detector configurations.

The detector response using paraffin as converter material is different compared to the steel's one. The increase in efficiency with the paraffin thickness is slower than the steel case, but never decreases for the same range of thicknesses. For small thicknesses, except from the 10 planes configuration, the efficiency for the two different materials is similar and higher than 20%. This fact leads to the idea that the rest of the components of the detector also work as converters.

Apart from the converter plates, the material present in more quantity in the RPC is the glass that contains the gas gaps. Some of the secondary particles that reach the gas gaps could be created in the glass plates. Therefore, we also studied the dependence of the one neutron detection efficiency on the converter material thickness for the detector with just glass as converter material.

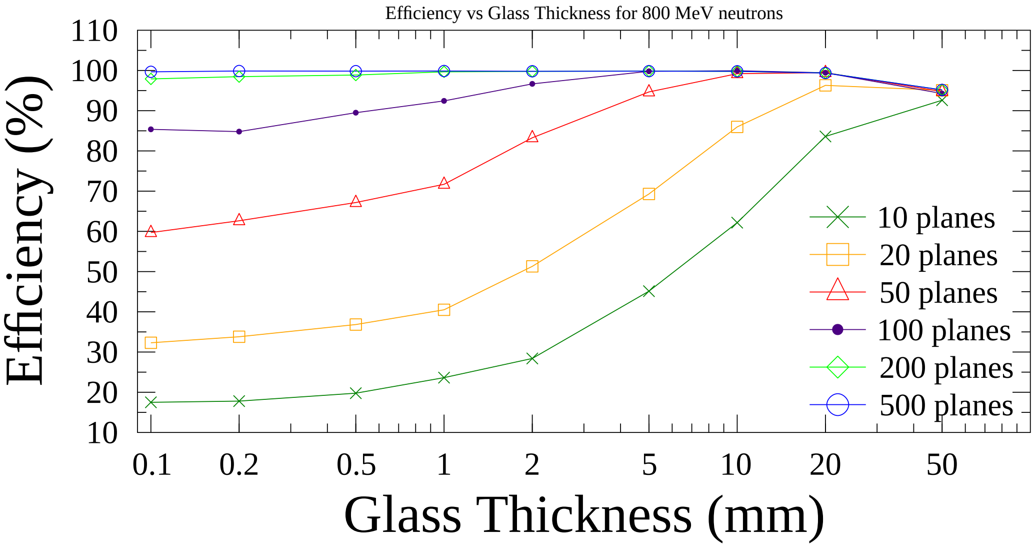

Figure 5.4: Variation of the one neutron detection efficiency as a function of the glass plates thickness for several detector configurations.

As it can be noted, the detector constructed with only glass plates still satisfies the design goals regarding the efficiency for one neutron detection.

5.3 Configurations using different converter materials

For comparison of the characteristics of the detector composed of one of the three converters materials considered, 3 configurations with similar efficiencies, one for each converter, were chosen. The selected detector configurations were:

- 50 planes, 2 mm of steel thickness
- 100 planes, 1 mm of paraffin thickness

- 200 planes, 0.1 mm of glass thickness

The detection principle of using the steel as a converter is the nuclear interaction of the neutron with iron, which produces a shower of charged particles that will lose energy in the gas gaps, being the secondary protons the major responsible for that. In the case of paraffin, a different detection principle will be expected due to its composition. The paraffin contains 15% of hydrogen and 85% of carbon. Because of the presence of hydrogen in the paraffin composition, it is expected that the neutron predominantly interacts with the hydrogen by elastic scattering.

Table 5.1 compares the total number of created protons for the three configurations and the kind of particle that induced its creation.

Table 5.1: Number of created protons and the kind of particle that induced its creation for the three configurations.

	Steel (2 mm - 50 planes)	**Paraffin (1 mm - 100 planes)**	**Glass (0.1 mm - 200 planes)**
Primaries detected	96.3%	90.9%	99.8%
Created protons	308776	82046	31736
Mother of proton: neutron	93.7%	96.4%	91.1%
Mother of proton: proton	3.0%	1.2%	3.3%
Mother of proton: other	3.4%	2.3%	5.6%

The detector constructed with paraffin produces more protons than the steel and the glass ones. As mentioned earlier, this fact results from the interaction principle with the converter. Glass and steel present similar results regarding the number of created protons and their origin. Thus, the interaction principle for both materials seems to be similar.

Figures 5.5, 5.6, and 5.7 present the number of detected protons per event considering respectively steel, paraffin and glass as converters for the selected configurations.

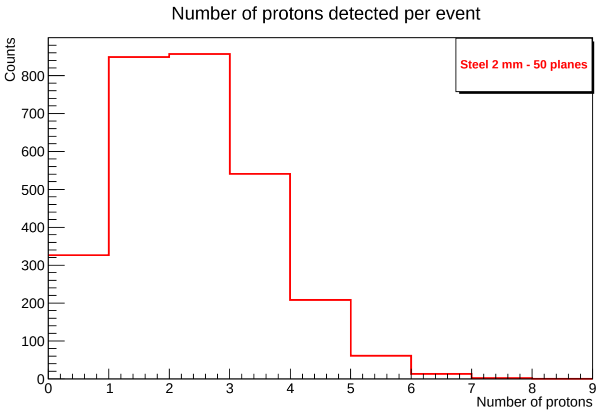

Figure 5.5: Number of detected protons per event for 2 mm steel - 50 planes.

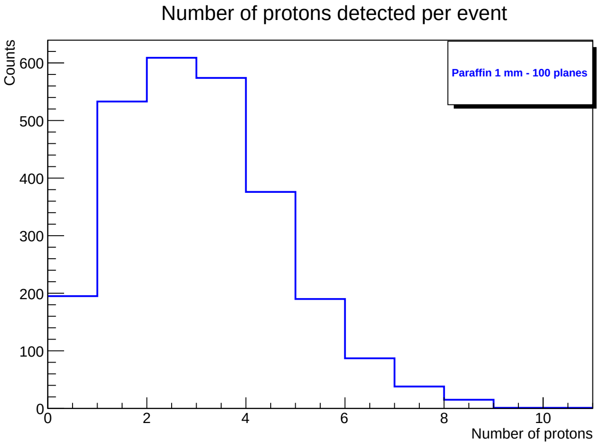

Figure 5.6: Number of detected protons per event for 1 mm paraffin - 100 planes.

In Figure 5.8 is also presented a comparison of the initial energy of the detected protons for the detector composed with different materials.

The number of detected protons does not significantly change with the converter material, although the mean number of detected protons considering glass is higher than in the other two cases. It can also be noticed that the energy of the detected protons ranges up to the energy of the generated neutrons of 800 MeV for all configu-

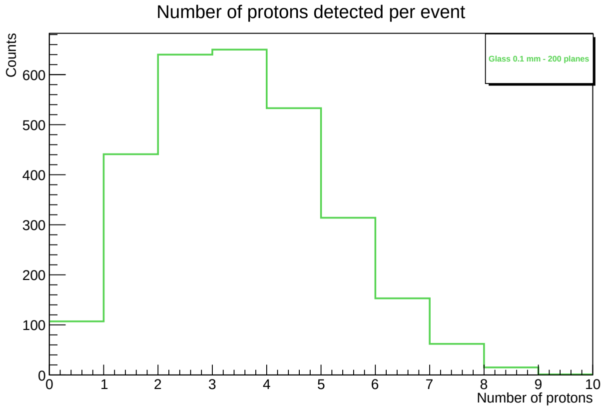

Figure 5.7: Number of detected protons per event for 0.1 mm glass - 200 planes.

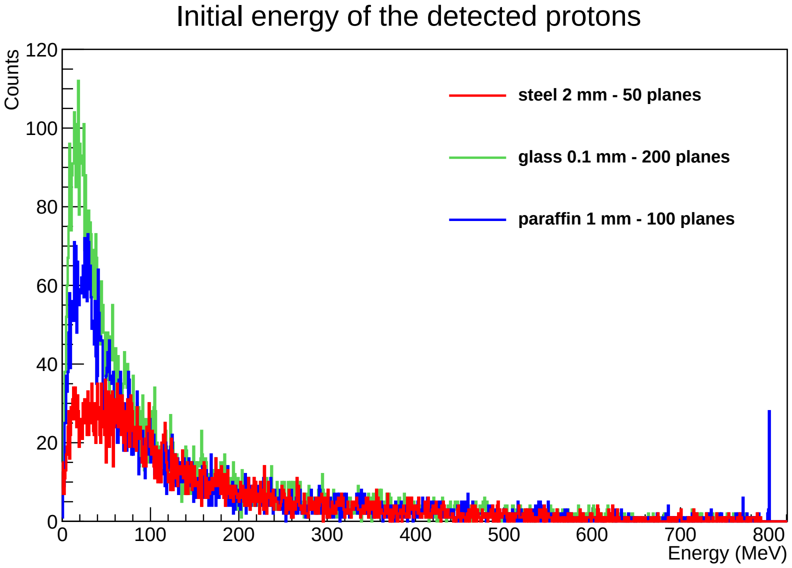

Figure 5.8: Initial energy of the detected protons for the detector developed with the considered geometries and converter materials.

rations. It can be noted however that in the low energy region the number of detected protons differs for the different materials. As steel is a material with high density and the configuration studied contains the larger thickness, the probability for low energy protons to not leave the material and reach the gas gaps increases. We can also see that the geometry with glass as converter material is the one who detects more low energy protons.

With these results, and considering just one of the design demands (the one neutron detection efficiency), we conclude that the detector could be built with any of the three studied materials. However, the development of a detector built with just glass plates is simpler [FON-11], as on the one hand the detector needs to have glass in its composition and on the other hand it is simpler to build from the standpoint of mechanics and electronics. Therefore, from now on, our investigations will concentrate on the characteristics of an iron-less RPC for the detection of high-energy neutrons.

6

The iron-less concept

After concluding that a detector built just with glass plates may do the work, it was considered a new concept design: the iron-less concept.

6.1 Geometry of the iron-less concept

Together with the LIP-Coimbra's group specialized in RPCs [LIP-web] a different concept for the detector with a new module geometry was considered. Since the glass could work as converter, it was defined a RPC module constituted by 5 gaps (maximum number of gaps for a RPC without compromising the high voltage [FON-11]), 6 plates of glass and a gas tight case made of plastic and with feedthroughs for the gas and HV. In Figure 6.1 the new concept for the iron-less RPC is shown.

The readout would be done with external electrodes with no additional feedthroughs an everything inside to a metallic shielding. A schematic view of the RPC design is shown in Figure 6.1).

Each RPC module would be a 2×2 m^2 device active area and the full size detector will have a modular structure constituted by a set of RPC modules (planes). In Figure 6.2 is shown the modular structure of the detector.

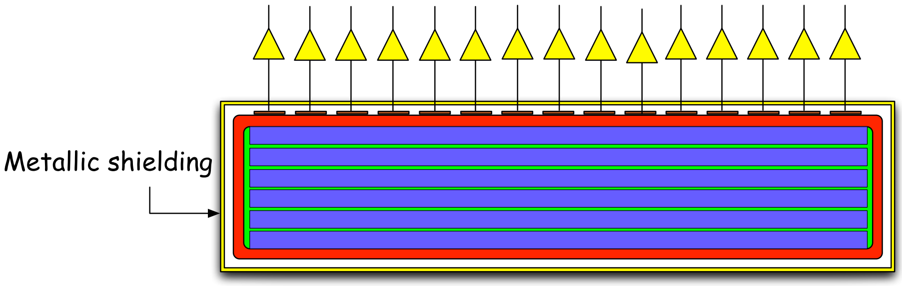

Figure 6.1: Schematic drawing of the iron-less RPC module with the readout electrodes.

This iron-less modular concept allows to adopt many possibilities. Converter material like steel or paraffin could be added in between the RPC modules as shown in Figure 6.3. This option seemed in the end not to be necessary.

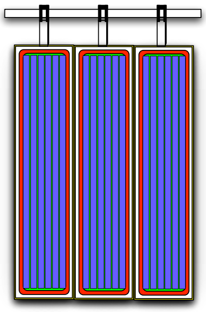

Figure 6.2: Schematic drawing of the modular structure of the full size detector.

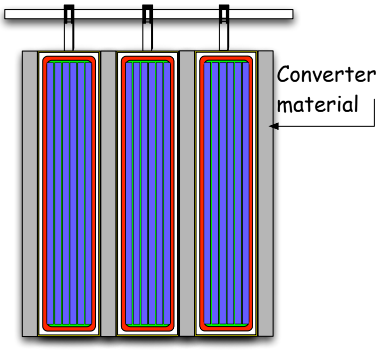

Figure 6.3: Schematic drawing of the modular structure of the full size detector with converter in between the RPC planes.

Thus, it was necessary to realize how many planes would be needed and what the best thickness for the glass plates.

6.2 Simulated geometry

For the simulation of the concept a new class was been developed, the *R3BNeuLandLIP* class which describes the geometry presented in Figure 6.4. A RPC plane with 5 gaps with the gas standard mixture (84% of Freon, 10% of SF_6 and of 6% Isobutane), 6 soda-lime glass plates and a plastic case. The RPC plane was constructed with the NeuLAND requirements of the dimensions for the active area, 2×2 m^2.

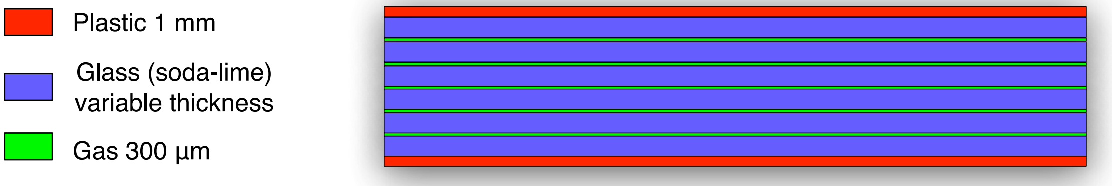

Figure 6.4: Schematic drawing of the iron-less RPC module.

In the simulation code there were implemented also options to control the thickness of the glass plates and to select the number of planes for the full detector. For simplicity the electrodes were not implemented at this stage, due to their small thickness, their contribution in the tracking of the particles relatively to the other materials present in the RPC is very small.

6.3 The one gap efficiency

Before studin the new RPC concept, it was necessary to verify the efficiency for one gap. The one gap efficiency is 75% [FON-11] for MIPs. Even if a particle loses energy in the gap, it does not means that it can be detected. In other words, the deposited energy needs to to be larger than a certain threshold. In order to determine the efficiency for one single gap in our simulations it was performed a simulation of a geometry of one gap for muons with a momentum of 300 MeV/c directed into a single gap geometry. The gap simulated geometry was the same dimensions as the ones from the RPC planes, 2×2 m^2 of active area and a thickness of 300 μm. The gap was placed at 35 m from the source with vacuum as the medium in between. There were generated 10000 events with one muon per event and this time the monte carlo engine used was the GEANT4.

In Figure 6.5 can be seen the variation of the one gap efficiency with the energy threshold.

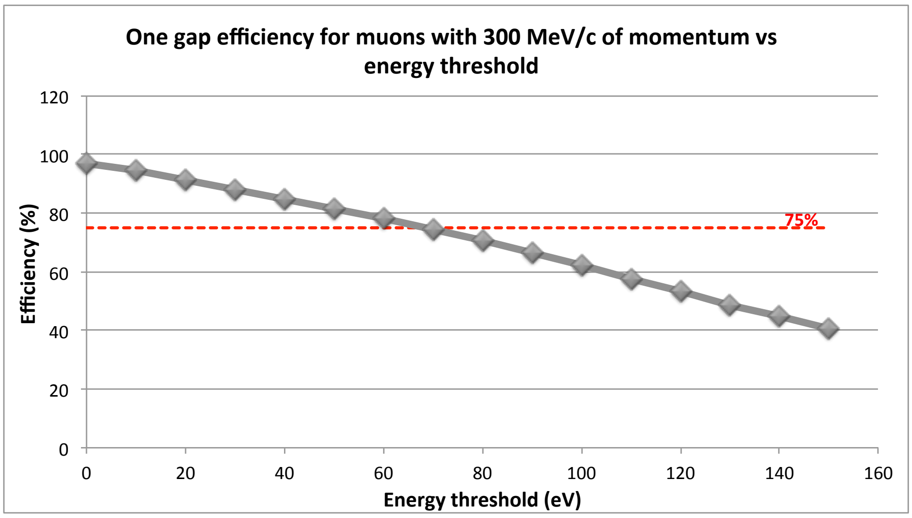

Figure 6.5: The one gap efficiency for different energy thresholds for the gap.

The efficiency without energy threshold was about 97%. By increasing the threshold, the efficiency starts to drop. As shown, an efficiency of 75% is obtained wen considering an energy threshold of 70 eV. Therefore, from now on it will be applied an energy threshold of 70 eV in order to limit the one gap efficiency to 75%.

6.4 Efficiency for one neutron detection

A similar analysis to the one shown in Chapter 5 it was done for the iron-less RPC. As already mentioned, it is necessary to know how many planes and which is the best thickness for the glass plates that provides the best performance for the detector. The glass plates are 2 m width and 2 m length which limits the thickness to 1 mm [FON-11]. Therefore, the selected thicknesses for the glass plates in this study were 1 mm, 2 mm, 3 mm, 4 mm and 5 mm.

For the simulations performed in the one neutron detection studies the following parameters were used:

- 10000 events
- GEANT4
- 1 neutron per event
- An energy of 429 MeV per neutron, $p = 995$ MeV/c
- Detector placed at 35 m from source (center of the detector)
- Vacuum as medium in the cave
- Open angle: 0 degrees
- 1, 2, 3, 4 and 5 mm of glass thickness
- An energy threshold of 70 eV

The medium in the cave was implemented as vacuum, although in the real setup will be air. The reason why we implemented vacuum was based in the fact that for large distances some neutrons never reach the detector since they will interact with air. Thus, for a reliable comparison we implemented vacuum as the medium in the cave to be sure that all the neutrons reach the detector.

For the glass plates thicknesses considered, several simulations were performed with different number of planes with the described parameters. In Figure 6.6 the efficiency for one neutron detection of the detector simulated with several configurations is shown.

Independent of the thickness of the glass plates, it is possible to reach efficiencies larger than 90% by increasing the number of planes.

For the evaluation of the performance of the detector in the reconstruction of the momentum of one neutron, 5 configurations considering different glass thicknesses and number of consecutive planes were chosen. The detection efficiency as function of the total glass thickness for the different detector configurations is shown at Figure 6.7. As

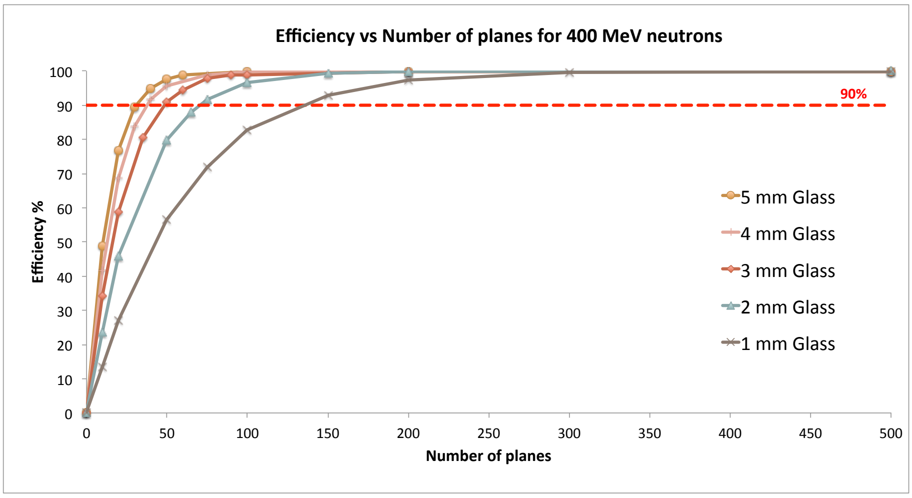

Figure 6.6: The one neutron detection efficiency for different detector configurations with different glass thicknesses.

it can be seen, the different curves follow on top of each other, reaching all of them a 100% efficiency for a total glass thickness of 180 cm.

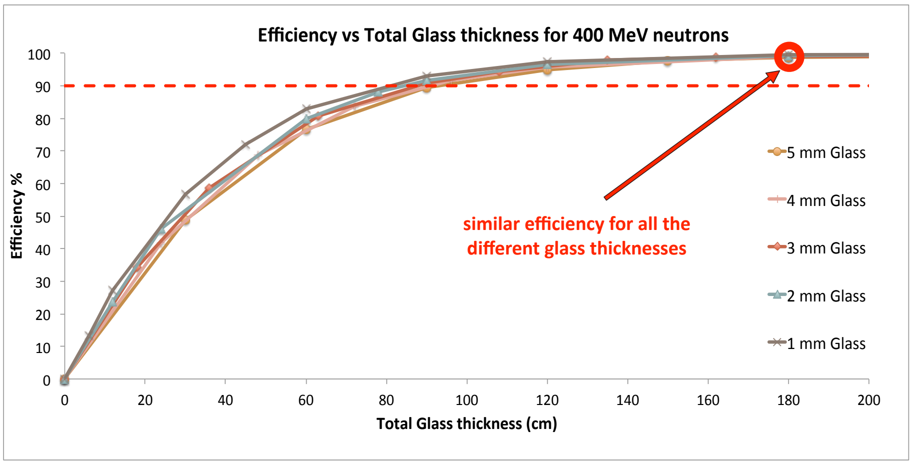

Figure 6.7: The one neutron detection efficiency for different total glass thicknesses.

The efficiencies values and the corresponding detector configurations chosen for the studies to follow are listed in the Table 6.1.

As already mentioned, the detector measures neutrons with energies in the range of

Table 6.1: Different detector configuration selected for characterization and the respective one neutron detection efficiency.

Detector Configuration (glass plates thickness / number of planes)	**One neutron efficiency**
1 mm / 300 planes	99.6%
2 mm / 150 planes	99.31%
3 mm / 100 planes	98.96%
4 mm / 75 planes	98.87%
5 mm / 60 planes	98.76%

200 MeV to 1000 MeV. In Figure 6.8 the detector efficiency for the selected geometries for the energy range between 200 MeV and 1000 MeV is shown.

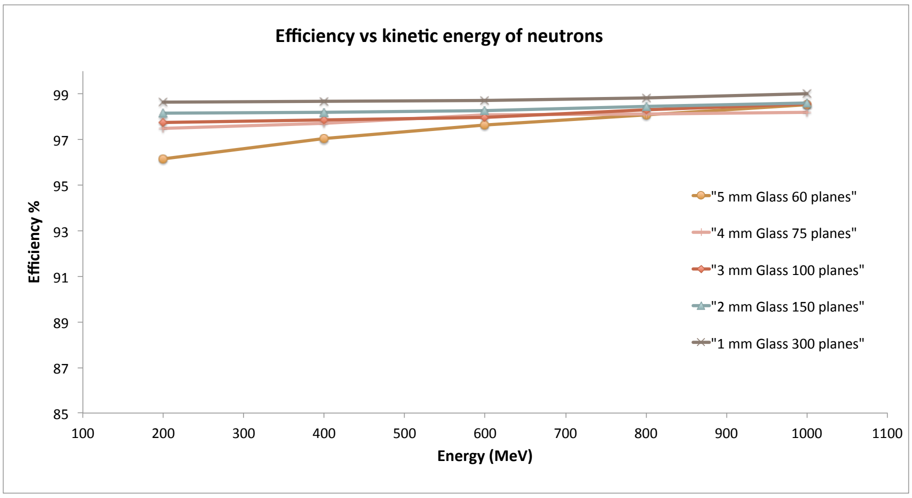

Figure 6.8: One neutron detection efficiency for different detector configurations.

As it can be seen, all configurations present an efficiency above the 90% for the energy range expected for the neutrons in R^{3}B experiments.

6.5 Multiplicity and energy of generated secondary particles

As first step in the comparison of the different configurations a comparison of the different detected particles per event was performed. Exemplary Figure 6.9 shows the detected particles per event for the 3 mm glass thickness configuration[1]. As it can be seen, the electrons/positrons and protons are the main responsible for the deposition of energy in the gas gaps. Also almost all events present protons and electrons that will be detected.

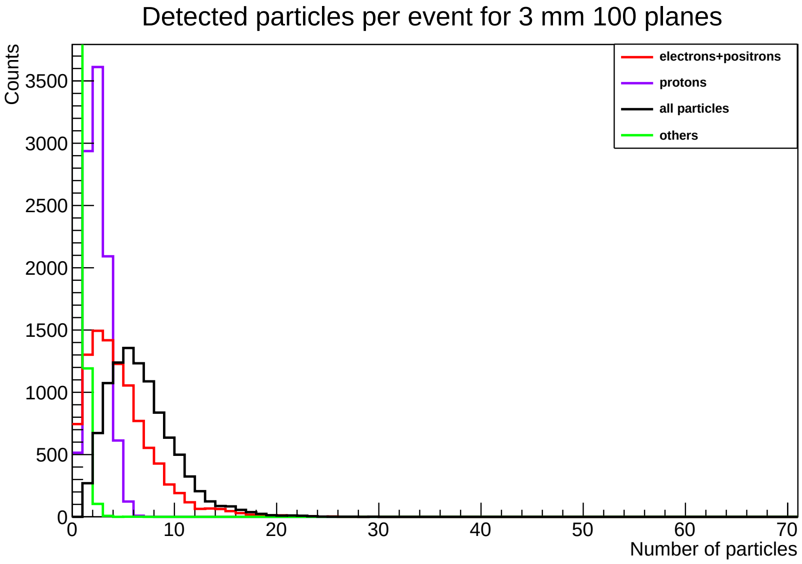

Figure 6.9: Comparison of the detected particles multiplicity for 3 mm glass thickness with 100 planes.

Table 6.2 lists the number of detected protons, electrons plus positrons and other particles for every simulated detector configuration considering 10000 primary neutrons. As can be seen by the table the electrons/positrons are the particles that interact more often with the gas. In addition, the total number of detected particles decreases with increasing glass thickness, which does not imply that there are fewer particles created.

---

[1] For the others configurations see Appendix A.1

The thicker the glass, the shorter the penetration of the particles in the detector. Thus, only the particles with enough energy will cross the glass and deposit energy in the gas. To reinforce this assumption, 3 histograms were created to compare the number of detected particles for each detector configuration. Figure 6.10 shows the detected proton multiplicity, Figure 6.11 the detected e^-/e^+ multiplicity and Figure 6.12 the multiplicity of all detected particles per event.

Table 6.2: Total detected particles for all the geometries.

	1 mm 300 planes	**2 mm 150 planes**	**3 mm 100 planes**	**4 mm 75 planes**	**5 mm 60 planes**
Protons	25482	21842	19565	18009	16664
Elect. + Posit.	58974	48963	41244	35054	30571
Others	2376	1809	1435	1275	1111
Total	86832	72614	62244	54338	48346

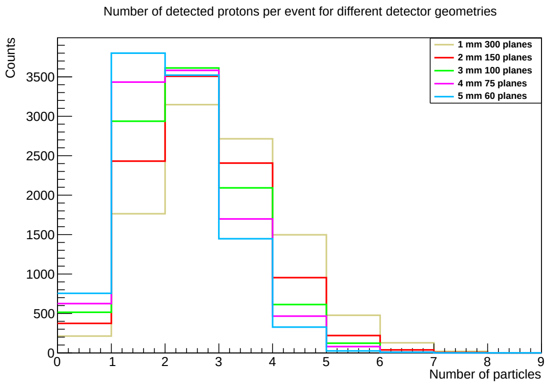

Figure 6.10: Protons multiplicity for all detector configurations.

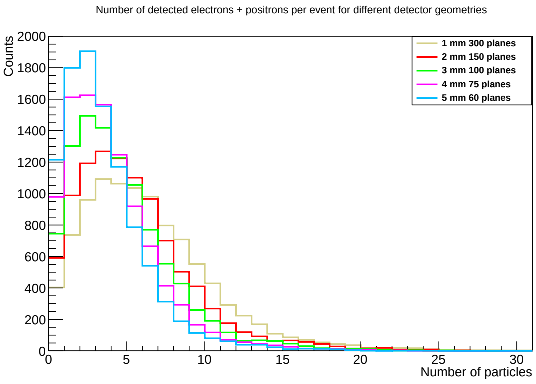

Figure 6.11: Electrons/positrons multiplicity for all detector configurations.

From this comparison we can observe that by increasing the glass thickness, the mean number of particles multiplicity shifts to the left, which means that we have less detected particles of all kind.

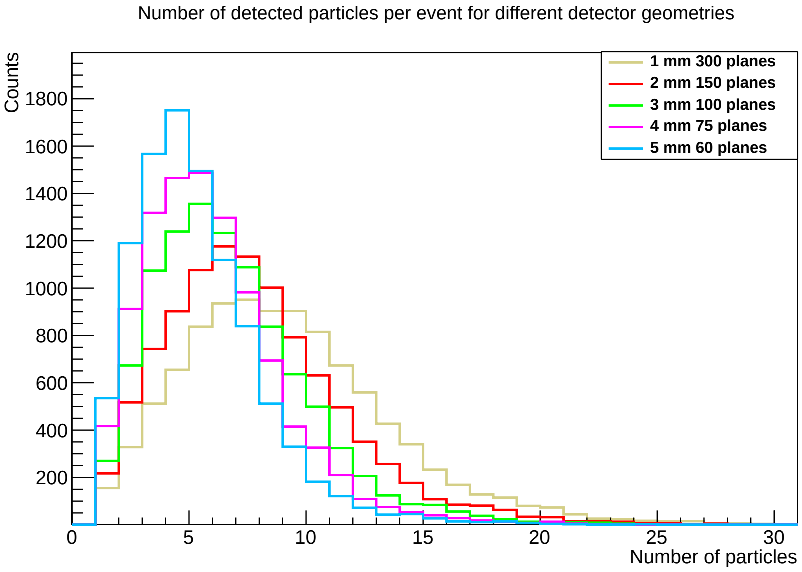

Figure 6.12: Detected particles per event for all detector configurations.

The particles that mainly lose energy in the gas gaps are protons and electrons or positrons. It is important therefore to characterize and compare the initial energy of those particles since they are the ones that are going to give the information of the neutron. The initial energy of the detected particles is shown on Figure 6.13 for the 3 mm glass thickness with 100 planes geometry[1]. All configurations of the detector follow the same initial energy distributions of the detected particles. The electrons energy range between zero and about 250 MeV while the detected protons have an initial energy in the range between zero and the initial energy of the primary neutrons generated.

A comparison of the initial energy of the detected particles was also performed for all the detector configurations. This is shown for the case of protons and electrons/positrons in Figures 6.14 and 6.15 respectively and for all particles Figure 6.16).

Similar to the study of the particle's multiplicity, the thicker glass the lower the number of particles that pass and deposit energy in the gaps. As it can seen in Figures

---

[1] For the others configurations see Appendix A.2

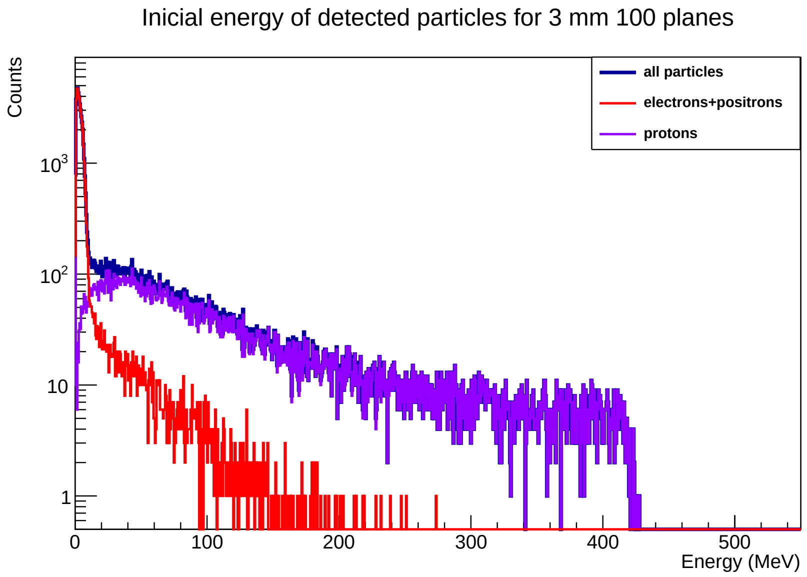

Figure 6.13: Initial energy of the detected particles for 3 mm 100 planes geometry.

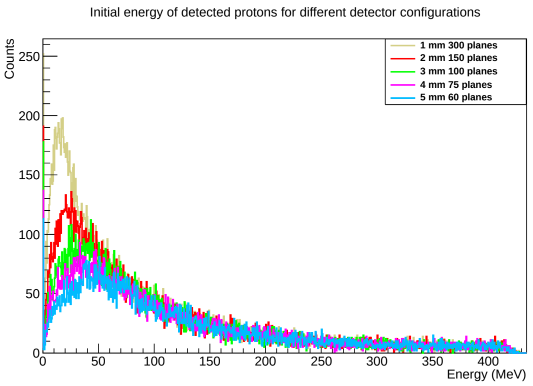

Figure 6.14: Initial energy of the detected protons for all detector configurations.

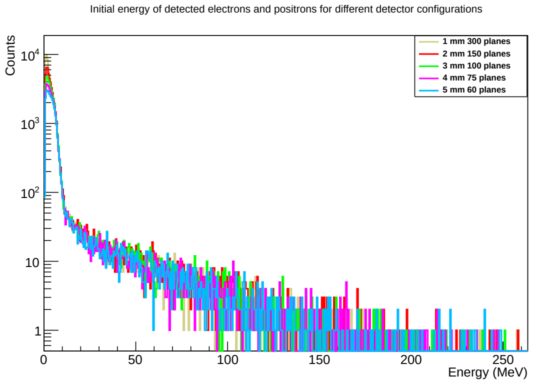

Figure 6.15: Initial energy of the detected electrons and positrons for all detector configurations.

6.14, 6.15 and 6.16, for higher energies the initial energy of the detected particles is similar contrary to what is observed in the lower energy region of the spectra. For the geometries composed of thicker glass, there are less counts in the spectra in the lower energy area. We can thus conclude, that the difference in the number of detected particles shown in Table 6.2 is due to the thickness of the glass plates, as the range of the slow energy particles is shorter than the thickness.

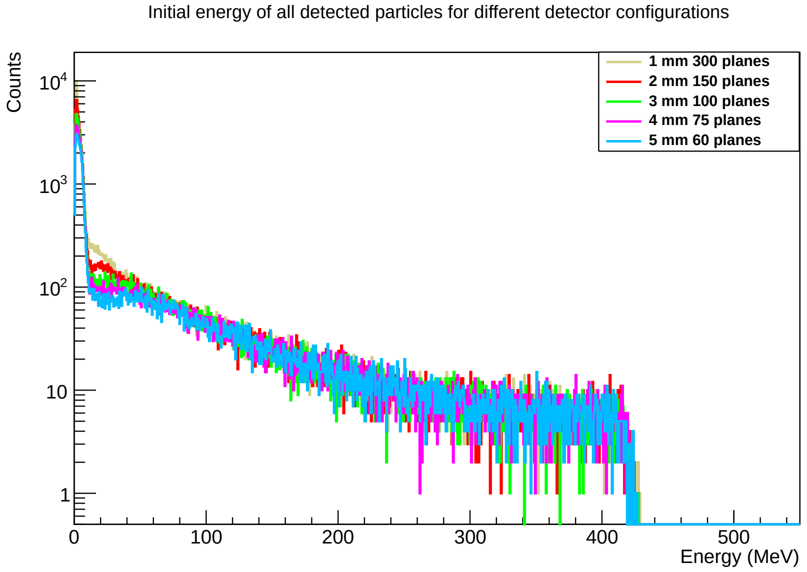

Figure 6.16: Initial energy of the all detected particles for all detector configurations.

Another important magnitude investigate the energy lost by the particles in the active medium of the detector, the gas gaps. For an avalanche to be generated, the charged particles as to lose a few tens of eV [FON-11]. In Figure 6.17 the energy loss distribution in the gaps for the detector configuration with 3 mm glass thickness and 100 planes[1] is shown.

The mean value of the energy distribution is higher than the necessary energy to generate an avalanche and well above of the energy threshold implemented to limit the one gap efficiency, which means that the energy deposit by the charged particles is enough to be detected.

The energy loss distribution of the gaps is similar for all geometries as expected from the initial energy distribution of the detected particles. Since the energy of the created secondary particles is similar for all detector geometries and the gap geometry and gas composition is equal for all configurations, one would expect the energy loss to be similar. However, the counts are not the same for all the geometries since the

---

[1] For the others configurations see Appendix A.3

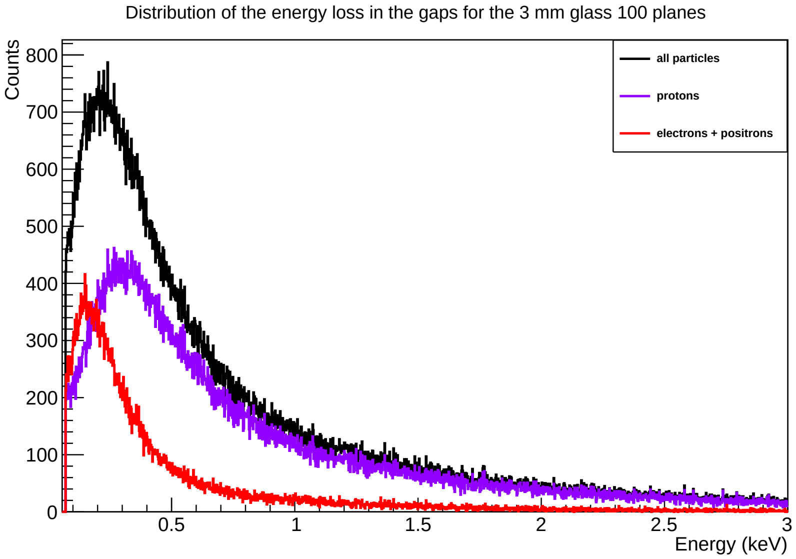

Figure 6.17: Energy loss distribution of the 3 mm 100 planes geometry discriminating the protons and the electrons + positrons.

number of particles detected for all the geometries is different. The mean value of a gaussian fit made to all the energy loss distributions is listed in Table 6.3 for comparison of the different detector geometries.

Table 6.3: Peak value for all the energy loss distribution for all the detector geometries considered.

	1 mm 300 planes	**2 mm 150 planes**	**3 mm 100 planes**	**4 mm 75 planes**	**5 mm 60 planes**
Protons	0.16 keV	0.17 keV	0.17 keV	0.17 keV	0.16 keV
Elect. + Posit.	0.32 keV	0.34 keV	0.33 keV	0.33 keV	0.33 keV
All particles	0.24 keV	0.24 keV	0.23 keV	0.24 keV	0.24 keV

As it can be seen, similar results for the energy lost by the protons as well as by the electrons are obtained.

6.6 Spatial distribution of the detected events

The spatial distribution of the detected events is extremely important for the reconstruction of the momentum of the neutrons that reach the detector. As seen in the previous section, the main particles for the neutron detection are the protons and the electrons/positrons. Thus, our analysis will concentrate on the characteristics of these two kind of secondary particles. For an accurate measurement of the neutron momentum, the distance from the point where energy was deposited by a secondary particle should be close to the initial trajectory of the neutron. A large distance will induce a large error for the neutron trajectory and consecutively a wrong result for the momentum of the neutron.

Figures 6.18 and 6.19 show the spacial distribution of all hits in the detector induced by a proton or by an electron/positron.

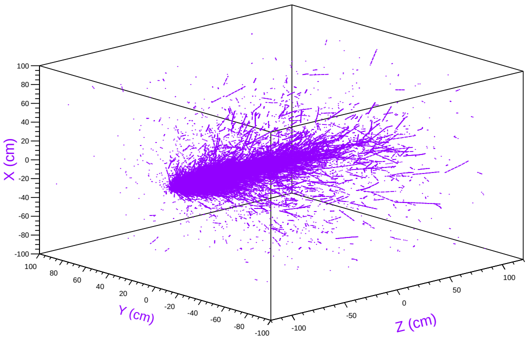

Figure 6.18: Spacial representation of all proton hits in the detector.

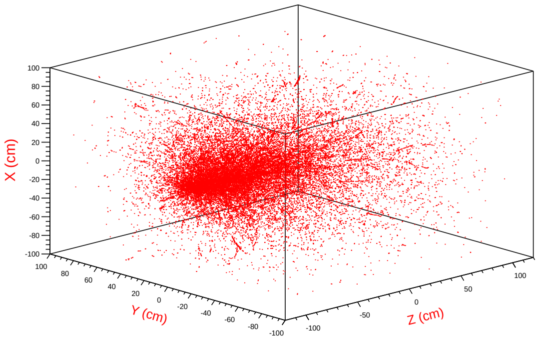

Figure 6.19: Spacial representation of all electron and positron hits in the detector.

The particles show a different behavior in the detector regarding the location of the energy depositions in the detector. Whereas protons interact several times leaving a trace of interactions, electrons usually deposit energy a few times before being completely stopped. The total number of crossed gaps per particle per plane is shown in Figure 6.20 for the case of 3 mm glass plates and 100 planes configuration[1]. Protons are the particles which penetrate the most crossing in average 10 gaps for this geometry. This is expected since they are the particles with higher initial energy. The electrons/positrons cross in average 2.3 gaps for this geometry. In Table 6.4 the average number of crossed gaps for each particle for each configuration is listed.

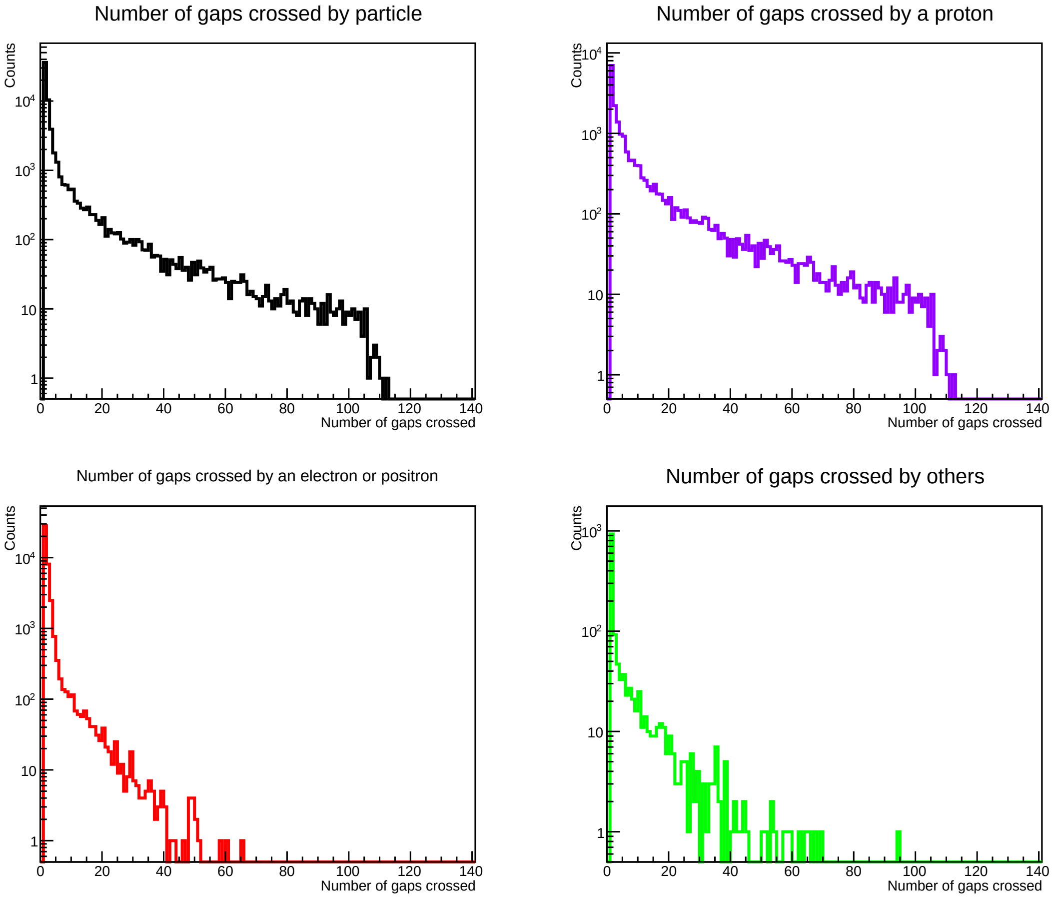

Figure 6.20: Number of gaps crossed by each particle for the geometry of 3 mm glass plates and 100 planes depth.

As it can be observed, the number of crossed gaps also depends on the glass thick-

---

[1] For the others geometries see Appendix A.4

Table 6.4: Average number of crossed gaps by each kind of particle for all detector geometries.

	1 mm 300 planes	**2 mm 150 planes**	**3 mm 100 planes**	**4 mm 75 planes**	**5 mm 60 planes**
Protons	23.0	13.4	10.1	8.7	7.4
Elect. + Posit.	3.0	2.1	1.8	1.6	1.5
All particles	9.0	5.6	4.5	4.5	3.6

ness. The thinner the glass plates the larger the number of crossed gaps for both protons and electrons/positrons. The fact that protons pass through multiple gaps may help for the tracking of the neutron at a later stage.

Although electrons are the particles which are more often created in the detector, they are not the particles that deposit energy more frequently. In Table 6.5 is shown the number of hits in the detector for each particle. As it can be observed protons interact more often with the gas in the detector.

Table 6.5: Number of hits in the detector for each kind of particles for each configuration.

	1 mm 300 planes	**2 mm 150 planes**	**3 mm 100 planes**	**4 mm 75 planes**	**5 mm 60 planes**
Protons	571327	285660	192620	152657	120694
Elect. + Posit.	162044	94368	67500	51490	42424
All particles	751220	389742	266508	209216	167158

Another aspect that the simulations allows us to investigate is the number of gaps activated per plane and per particle type. This information may help in improving the analysis of multi-hit events (section 6.7). As already shown, two kind of particles are the main responsible for the detection of the neutron: protons and electron/positrons, which has already shown behave completely different inside the detector.

In Figure 6.21 the activated gaps per plane per event for the 3 mm glass thickness and 100 planes geometry is shown[1].

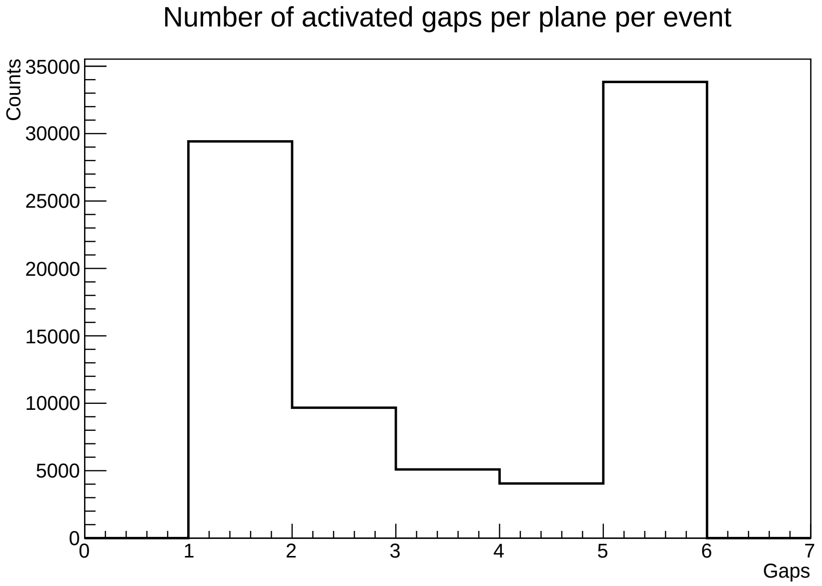

Figure 6.21: Number of gas gaps activated per plane per event for the 3 mm glass 100 planes geometry.

As it can be seen, most of the times either one or five gaps are activated per plane. This suggests there might be two different processes responsible for it. We have already observed that protons cross in average more gaps than electrons/positrons which may be correlated the effect shown in Figure 6.21. The number of activated gaps per plane discriminated by electrons/positrons and protons is shown in Figures 6.22 and 6.23, respectively.

As it can be seen, the previously made assumption is correct: electrons/positrons deposit energy more often in just one gap per plane while protons deposit energy more often in five gaps per plane.

We can also study the sensitive of the detector regarding the number of gaps activated per plane. For this, the efficiency considering different numbers of activated gaps

---

[1] For the others geometries see Appendix A.10

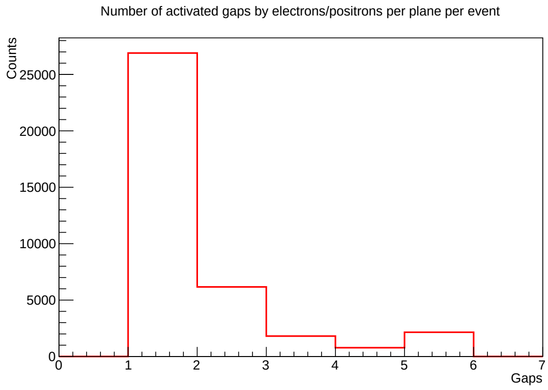

Figure 6.22: Number of gas gaps activated by electrons/positrons per plane per event for the 3 mm 100 planes geometry.

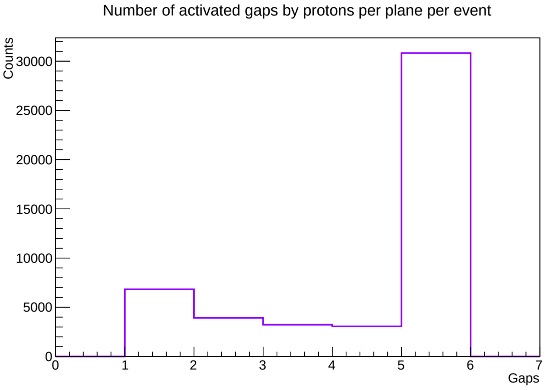

Figure 6.23: Number of gas gaps activated by protons per plane per event for the 3 mm 100 planes geometry.

per plane for the one neutron case was calculated. This information is important since the hardware requirements for the detector are not the same if the majority of events deposit energy in almost all the gaps per plane or otherwise deposit energy just in a few or in a single gap [FON-11].

The results of this analysis are listed in Table 6.6.

Table 6.6: One neutron detection efficiency considering different numbers of activated gaps per planes for all the detector geometries.

	Detector geometries				
Number of Gaps	**1 mm 300 planes**	**2 mm 150 planes**	**3 mm 100 planes**	**4 mm 75 planes**	**5 mm 60 planes**
5	90.28%	76.19%	66.82%	63.37%	56.12%
4 or 5	94.69%	83.64%	74.3%	69.94%	63.98%
3 or 4 or 5	98.00%	92.1%	84.69%	79.44%	73.87%
1	89.16%	88.94%	87.93%	86.37%	84.93%
1 or 2	94.63%	94.16%	93.53%	92.75%	91.91%
1 or 2 or 3	97.10%	96.70%	96.13%	95.78%	95.27%
all	99.60%	99.31%	98.96%	98.87%	98.76%

As it can be seen, the detection of events that deposit energy in few gaps becomes relevant for the geometries with thicker glass plates, as it is less probable that almost all gaps from a plane are fired. We can conclude that the detection in a few or in a single gap is important for the total detection efficiency, mainly for the geometries with thicker glass plates.

Another important aspect is the characterization of the particle that provides the first signal in the detector. As the detector is a Time-of-Flight system we are interested in the measurement of the time when the neutron reaches the detector. This time is given by the first energy deposition in the detector. The probability that each kind of particle provides the first energy deposition is listed in Table 6.7 for each detector geometry.

Table 6.7: Probability that a particle gives the fastest energy deposition for all detector configurations.

	1 mm 300 planes	**2 mm 150 planes**	**3 mm 100 planes**	**4 mm 75 planes**	**5 mm 60 planes**
Protons	75.61%	74.34%	74.13%	74.66%	74.35%
Elect. + Posit.	20.23%	21.73%	22.30%	21.80%	21.86%
Other particles	4.16%	3.93%	3.57%	3.54%	3.79%

The first energy deposition is mainly done by the protons, independent of the configuration and for about 75% of all events. Electrons and all other particles behave similarly for the different detector geometries. Which particle interacts first is intrinsically related to the initial energy distribution of the created particle by the nuclear interaction of the neutron on the detector which, as already showed, is quite similar for all the configurations of the detector.

Another important aspect for the detection is the spatial dispersion of the hits compared to the initial trajectory of the neutron. The secondary particles are created in all directions as can be seen in the tridimensional spacial distribution of all the hits shown Figures 6.18 and 6.19, however it is important that the first interaction of the charged particles in the detector is near to the path of the neutron. Figure 6.24 shows the spacial distribution in x, y and z for the first hit in each event, as well as a two-dimensional (x vs y) distribution for the 3 mm glass thickness geometry[1].

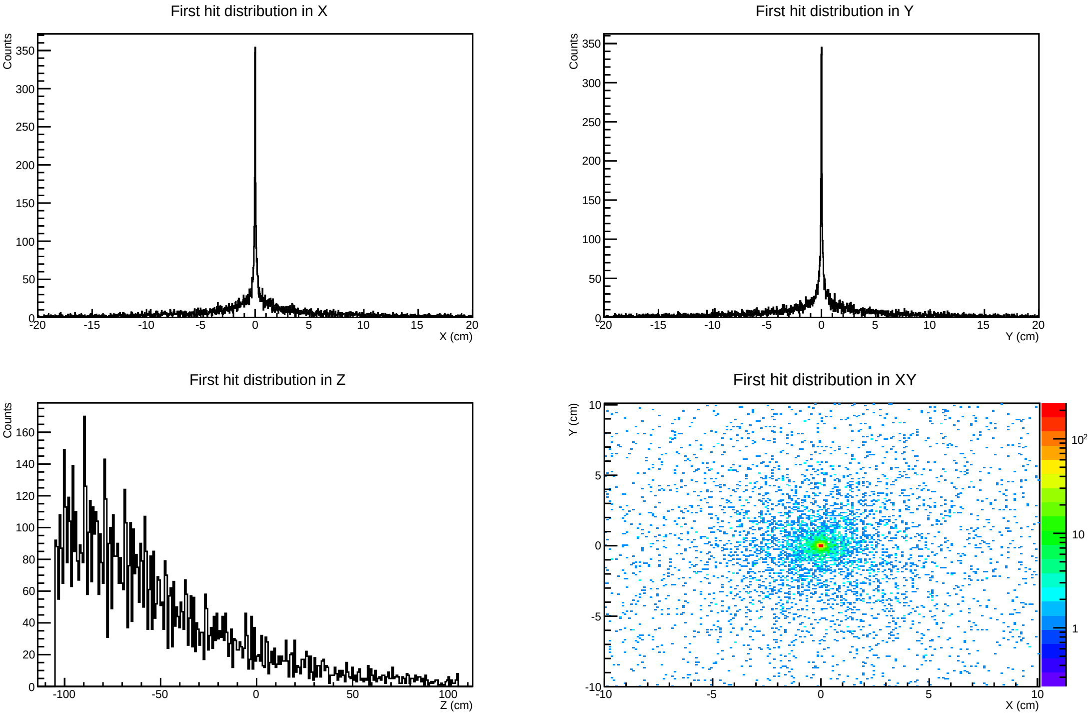

Figure 6.24: Spacial distribution of the first hit on the detector for the 3 mm 100 planes configuration.

The center of the detector is at the position $(x, y, z) = (0, 0, 0)$ and the source is at position $(x, y, z) = (0, 0, -3500)$. All units are in cm. The neutrons are generated along the $(0, 0, 1)$ direction. As it can be observed, most interactions are near the initial neutron trajectory, with peaks located at $(x, y) = (0, 0)$. Regarding the position distribution along the direction of the neutrons (z-axis), usually the first event happens

---

[1] For the others geometries see Appendix A.5

at the detected surface (at about $z = -100$ cm). We also see that for almost all events, the first interaction happens in the first half of the detector.

6.7 Multi-hit recognition

As mentioned in the design goals of the NeuLAND detector, one of the requirements for the detector is the multi-hit recognition up to 5 neutrons. The RPC does not provide a sufficiently valid energy resolution [FON-11] which means that we can not use the energy loss of the particles in the gas gaps to determine the number of neutrons that reached the detector. Therefore we need to use a different quantity to achieve this purpose. In this work, the initial steps in this analysis were performed by characterizing the dependence of the different event multiplicities obtained from the simulation on the simulated number of neutrons.

In the analysis of the multiplicity, several approaches were applied and various simulations were performed. For all considered detector geometries, several neutrons (up to 4) with the same energy and trajectory emitted at the same time were simulated.

6.7.1 Multiplicity analysis

The first approach considered was the analysis of the gas gaps multiplicity, i.e., this multiplicity is given by the number of gas gaps in which energy has been deposited by the secondary particles. The number of created particles will increase with the number of neutrons which leads to a larger number of activated gaps per event. In Figure 6.25 a comparison of the gaps multiplicity for 1, 2, 3 and 4 neutrons is shown for the 3 mm glass thickness with 100 planes configuration.[1].

In all cases the multiplicity distribution presents long tails that make the multi-hit recognition very inefficient.

---

[1] For the others geometries see Appendix A.6

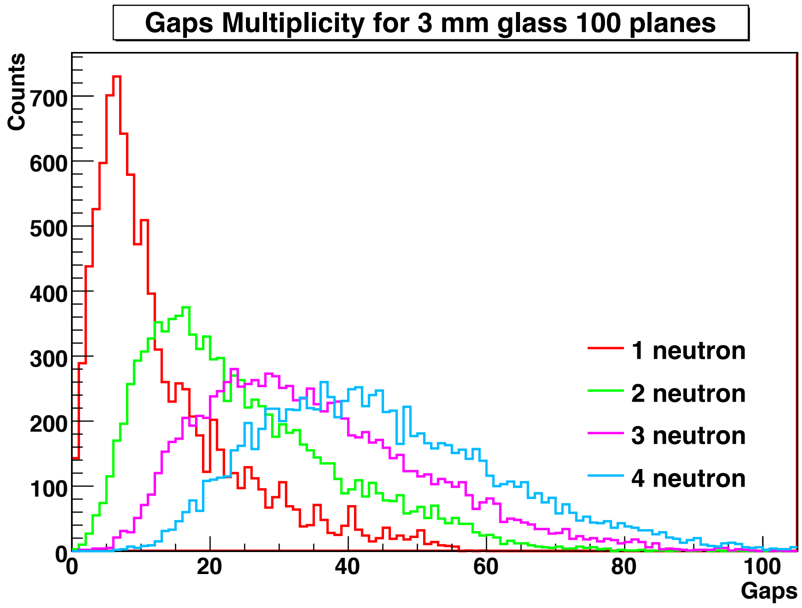

Figure 6.25: Gaps multiplicity for the 3 mm 100 planes geometry for different number of incoming neutrons.

Perhaps this result could be improved by considering the multiplicity of the planes where almost all gaps were activated (mainly originated by protons. See section 6.6) or when just a few gaps were activated per plane (mainly caused by electrons/positrons. See section 6.6). The plane multiplicity of a different number of incoming neutrons considering 1 or 2 activated gaps per plane and considering 3, 4 or 5 gaps activated per plane is shown respectively in Figures 6.26 and 6.27.

The multiplicity considering just a certain number of gaps makes even worst the multi-hit recognition as can be seen in the Figures 6.26 and 6.27. Therefore, a new approach is needed for the multi-hit recognition analysis.

This new approach was to count the number of activated planes per event, i.e, for all detector configurations we determined how many detector planes have experienced at least one energy deposition in at least one of the five gas gaps. The result of this analysis is shown in Figure 6.28 using the same simulated data at the previous analysis.[1].

---

[1] For the others geometries see Appendix A.7

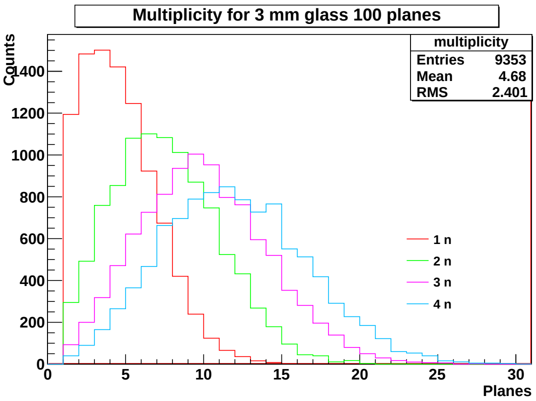

Figure 6.26: Plane multiplicity of different incoming neutrons considering just the planes were 1 or 2 gaps were activated.

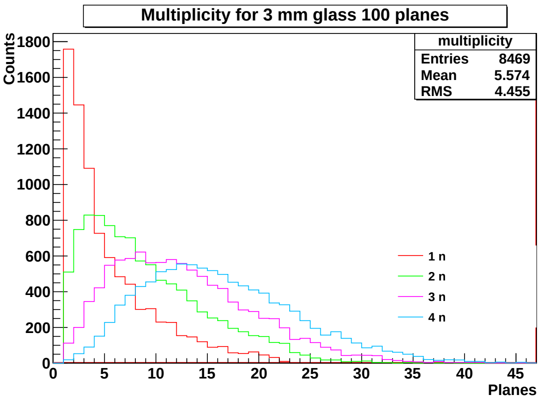

Figure 6.27: Plane multiplicity of different incoming neutrons considering just the planes were 3, 4 or 5 gaps were activated.

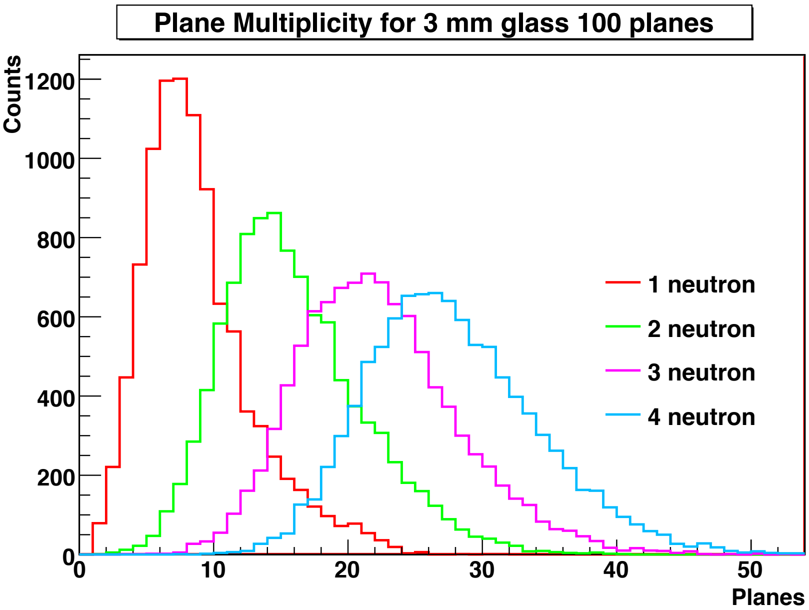

Figure 6.28: Plane multiplicity for the 3 mm 100 planes geometry for different number of incoming neutrons.

In this case, the multiplicity distributions became thiner with shorter tails. However they are not yet completely separated which may reduce the efficiency in the correct determination of the number of detected neutrons.

Finally, an additional approach was considered in the analysis of the multiplicity, taking into account the number of pair of planes activated per event, i.e., every time there was a deposition of energy in a pair of planes, the multiplicity was increased. In Figure 6.29 is shown a comparison for the three multiplicities for the 3 mm glass thickness geometry for the 1 neutron case. As it can be seen, the tails of the peaks were reduced with the applied analysis for the plane multiplicity and even more reduced for the 2 planes multiplicity.

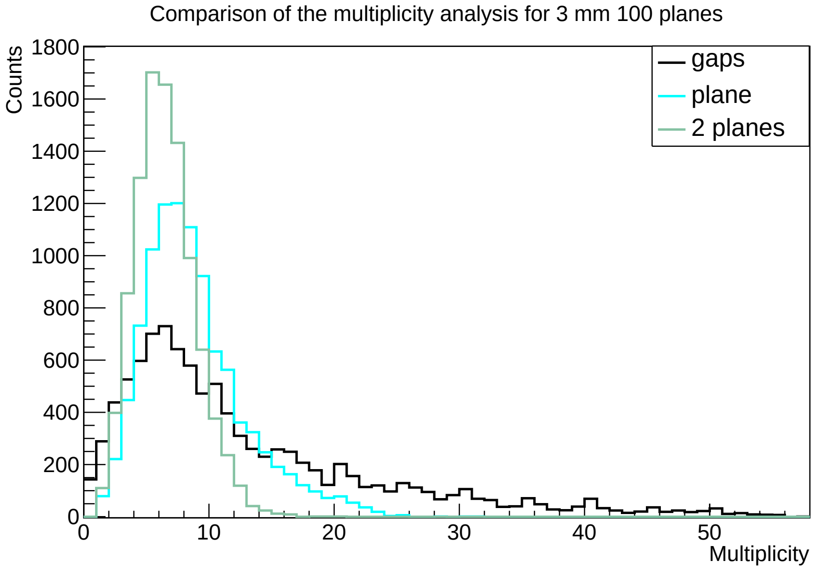

Figure 6.29: Comparison of the multiplicity analysis for the 3 mm 100 planes geometry for one incoming neutron case.

One example of the 2-planes multiplicity comparison for different number of incoming neutrons is presented in Figure 6.30 again for the 3 mm configuration[1].

As it can be seen, the resolution in determining the number of neutrons improve considerably with the two planes multiplicity and the tails are reduced, however they still are overlapped and not completely separable which means that the efficiency for the detection of multi neutrons will not be maximized using solely this method for the identification of the neutrons. In the areas overlapped, there will be a percentage of events for which we will not correctly identify wrongly the number of neutrons.

---

[1] For the others geometries see Appendix A.7

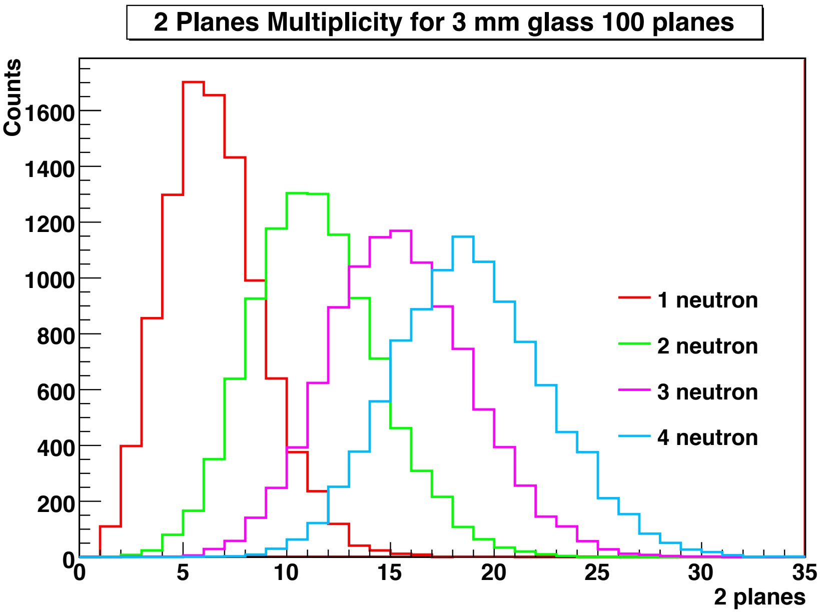

Figure 6.30: Two plane multiplicity for the 3 mm 100 planes geometry for different number of incoming neutrons.

6.7.2 Identification matrices

Using the information of the different multiplicities for the identification of the number of incoming neutrons, a gaussian fit to all histograms of the plane multiplicity and of the two planes multiplicity analysis was done. Table 6.8 lists the mean values and the FWHM of the gaussian fits made to the peaks of the plane multiplicity for all the detector configurations. As it can be seen, the mean values of the distribution increase with the number of neutrons per event, however the width of the peaks also increases. The mean values decrease with the increase of the glass thickness of the detector configuration as expected from previous analysis.

Table 6.9 is equivalent to the previous table but lists the values for the two planes multiplicity.

Table 6.8: Mean values and FWHM of the gaussian fits made to the histograms of the plane multiplicity for all the detector geometries.

Plane Multiplicity								
	1 neutron		**2 neutrons**		**3 neutrons**		**4 neutrons**	
	Mean	**FWHM**	**Mean**	**FWHM**	**Mean**	**FWHM**	**Mean**	**FWHM**
1 mm 300 p.	14.4	13.7	29.3	26.0	45.8	28.0	60.3	39.6
2 mm 150 p.	9.9	9.2	20.6	14.9	29.3	18.8	37.6	19.6
3 mm 100 p.	8.0	7.6	15.6	10.8	22.0	12.6	27.7	14
4 mm 75 p.	6.6	6.0	12.5	8.6	17.3	9.7	22	10.5
5 mm 60 p.	5.8	5.4	10.9	7.5	15.2	8.5	18.8	9.3

Table 6.9: Mean values and FWHM of the gaussian fits made to the histograms of the two planes multiplicity for all the detector geometries.

Two Plane Multiplicity								
	1 neutron		**2 neutrons**		**3 neutrons**		**4 neutrons**	
	Mean	**FWHM**	**Mean**	**FWHM**	**Mean**	**FWHM**	**Mean**	**FWHM**
1 mm 300 p.	11.1	9.3	22.3	14.5	31.4	16.9	39.4	19.9
2 mm 150 p.	8.0	6.8	14.7	9.2	20.3	10.6	25.0	11.6
3 mm 100 p.	6.4	5.5	11.4	7.0	15.5	7.9	18.9	8.6
4 mm 75 p.	5.4	4.7	9.5	5.9	12.7	6.6	15.4	7.1
5 mm 60 p.	4.7	4	8.1	5.1	10.8	5.7	13.0	6.1

From the comparison of the tables, it can be seen that the mean values decrease for the two planes multiplicity analysis as also the FWHM does.

With the values from the Tables 6.8 and 6.9 several linear regressions were performed for the number of neutrons as a function of the mean value of the gaussian fits. The FWHM was considered as the error of the points.

Figures 6.31 and 6.32 show the linear relation between the number of neutrons and the mean value of the multiplicity for booth cases, plane multiplicity and two planes multiplicity for the 3 mm thickness geometry[1].

Five linear equations for each multiplicity analysis were obtained, two for each

---

[1] For the others geometries see Appendix A.9

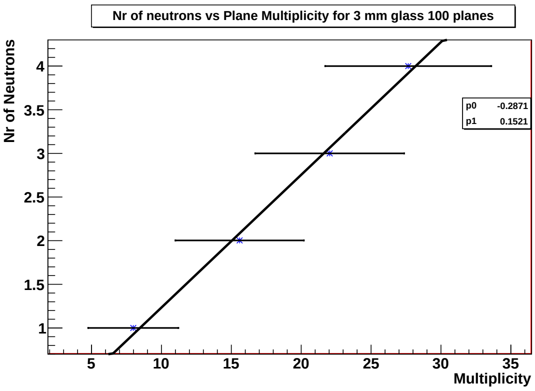

Figure 6.31: Linear regression to the number of neutrons in function of the mean value of the plane multiplicity.

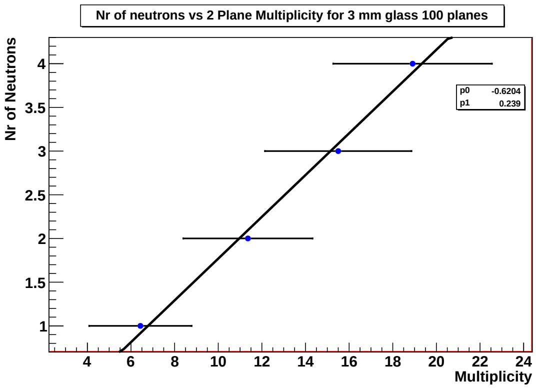

Figure 6.32: Linear regression to the number of neutrons in function of the mean value of the two planes multiplicity.

detector geometry. These equations are listed in Table 6.10.

Considering these equations, the simulated data were analyzed for all the different incoming neutrons cases and for all geometries. For each event, the multiplicity was extracted and the respective number of incoming neutrons was calculated rounding the result to the closest integer value.

Table 6.10: Equations for the number of neutrons (N_n) as a function of the mean value of the peaks multiplicity (m_n) for the two multiplicity methods for all the different detector geometries.

	Plane Multiplicity	**Two Plane Multiplicity**
1 mm 300 p.	$N_n = 0.06489m_n + 0.06916$	$N_n = 0.1057m_n - 0.2503$
2 mm 150 p.	$N_n = 0.1086m_n - 0.1439$	$N_n = 0.1755m_n - 0.4814$
3 mm 100 p.	$N_n = 0.1521m_n - 0.2871$	$N_n = 0.239m_n - 0.6204$
4 mm 75 p.	$N_n = 0.1961m_n - 0.3621$	$N_n = 0.2998m_n - 0.7201$
5 mm 60 p.	$N_n = 0.2299m_n - 0.4095$	$N_n = 0.3567m_n - 0.7699$

Thus, without knowing how many neutrons reached the detector, several tables considering the identification of the detected neutrons were made to determine the detection efficiency for different number of neutrons per event.

These identification matrices are presented in Tables 6.11-6.15.

Table 6.11: Identification matrices for the plane and two plane multiplicities for 1 mm glass thickness and 300 planes geometry.

	Primary							
	Plane Multiplicity				**Two Plane Multiplicity**			
Detected	**1 n**	**2 n**	**3 n**	**4 n**	**1 n**	**2 n**	**3 n**	**4 n**
1 n	**74%**	20%	1%		**82%**	20%	1%	
2 n	16%	**44%**	24%	4%	14%	**54%**	28%	4%
3 n	6%	22%	**37%**	25%	2%	19%	**43%**	29%
4 n	2%	9%	23%	**35%**		4%	21%	**43%**
5 n		2%	9%	20%			4%	17%
6 n			2%	9%				3%
7 n				3%				

Table 6.12: Identification matrices for the plane and two plane multiplicities for 2 mm glass thickness and 150 planes geometry.

	Primary							
	Plane Multiplicity				**Two Plane Multiplicity**			
Detected	**1 n**	**2 n**	**3 n**	**4 n**	**1 n**	**2 n**	**3 n**	**4 n**
1 n	**79%**	19%	1%		**87%**	25%	2%	
2 n	16%	**53%**	28%	6%	11%	**47%**	21%	4%
3 n	4%	20%	**40%**	30%		24%	**49%**	30%
4 n		6%	22%	**39%**		2%	22%	**43%**
5 n			5%	17%			3%	17%
6 n			1%	5%				2%
7 n				1%				

Table 6.13: Identification matrices for the plane and two plane multiplicities for 3 mm glass thickness and 100 planes geometry.

	Primary							
	Plane Multiplicity				**Two Plane Multiplicity**			
Detected	**1 n**	**2 n**	**3 n**	**4 n**	**1 n**	**2 n**	**3 n**	**4 n**
1 n	**82%**	23%	2%		**85%**	21%	3%	
2 n	15%	**51%**	28%	6%	14%	**58%**	32%	8%
3 n	2%	20%	**45%**	35%		16%	**42%**	32%
4 n		3%	17%	**33%**		4%	19%	**38%**
5 n			5%	18%			3%	16%
6 n				4%				3%
7 n				3%				

Table 6.14: Identification matrices for the plane and two plane multiplicities for 4 mm glass thickness and 75 planes geometry.

	Primary							
	Plane Multiplicity				**Two Plane Multiplicity**			
Detected	**1 n**	**2 n**	**3 n**	**4 n**	**1 n**	**2 n**	**3 n**	**4 n**
1 n	**82%**	24%	2%		**89%**	29%	4%	
2 n	14%	**47%**	24%	4%	9%	**43%**	24%	6%
3 n	3%	21%	**42%**	28%		24%	**50%**	39%
4 n		5%	22%	**38%**		2%	16%	**33%**
5 n			6%	23%			3%	15%
6 n				4%				3%
7 n								

Table 6.15: Identification matrices for the plane and two plane multiplicities for 5 mm glass thickness and 60 planes geometry.

	Primary							
	Plane Multiplicity				**Two Plane Multiplicity**			
Detected	**1 n**	**2 n**	**3 n**	**4 n**	**1 n**	**2 n**	**3 n**	**4 n**
1 n	**86%**	29%	3%		**90%**	31%	5%	
2 n	11%	**44%**	25%	6%	8%	**49%**	32%	11%
3 n	1%	22%	**48%**	37%		14%	**30%**	23%
4 n		2%	16%	**34%**		4%	25%	**42%**
5 n			4%	16%			4%	18%
6 n				4%				3%
7 n				3%				

As it can be seen, the results improved by using the 2-planes multiplicity compared to the one plane multiplicity. However, the identification of multi-hit becomes better for ticker glass plates. Overall, the detector geometry with 100 planes and 3 mm glass plates thickness is the one that presents better and more homogeneous results for the multi-hit recognition.

6.8 Reconstruction of the neutron momentum

The momentum of relativistic neutrons is defined as:

$$p = \gamma m v \tag{6.1}$$

where m is the neutron mass, v the velocity of the neutron with respect to a given frame of reference and γ the Lorentz factor given by:

$$\gamma = \frac{1}{\sqrt{1-\beta^2}} \tag{6.2}$$

where $\beta = v/c$ being c the speed of light in a vacuum.

The momentum will be indirectly determined. The detector provides information in the Time-of-Flight of the projectile as well as the distance from the target were the projectile is produced to indirectly determine its velocity and respective momentum.

6.8.1 Two possible analysis choices

In order to reconstruct the momentum, two possible choices of analysis were considered: one using the first interaction with the smallest time; and another using the interaction which gives us the biggest neutron velocity, and consequently the biggest β. Figure 6.33 represents two energy depositions, A and B from the same neutron event, at a distance from the target d_A and d_B, by two secondary charged particles.

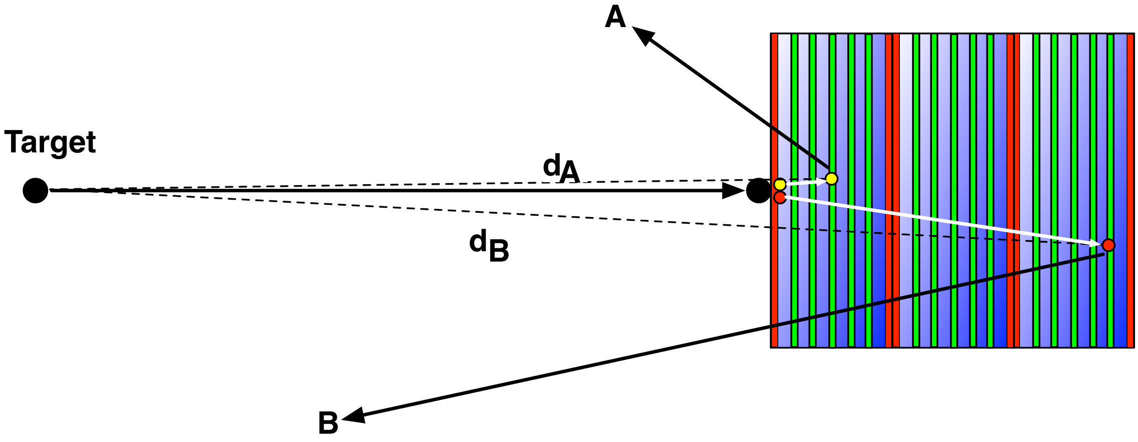

Figure 6.33: Schematic drawing of the two analysis methods for the momentum reconstruction.

Assuming that the time of the energy deposition t_A is smaller than t_B and $t_A \approx t_B$, and the distance d_B is larger than the distance d_A, the momentum of the respective neutron is going to be better described by the deposition B which will give a velocity d_B/t_B closer to the neutron velocity. This situation happens, as the energy of the secondary particles ranges from 0 MeV to the energy of the initial energy of the neutron (see section 6.5). For instance, two particles A and B can be created with completely different energies being the energy of the particle A much smaller than that of particle

B. The particle A, even with a smaller energy than particle B, can provide a faster time signal. However, if their times are similar, the particle B travelled a larger distance in the detector before being detected, providing a better reconstruction of the neutron velocity and consecutively a bigger β than the particle A.

However, with larger depth penetration by the particles, one should expect a larger dispersion in x and y on the detector for the particles that provide a bigger β which will be important later in this discussion.

6.8.2 Spacial distribution of the events which provides the biggest β

Using the hit on the detector that provides the bigger β, it is important to characterize the spacial distribution in the detector, since this quantity may have influence in the reconstruction of the excitation energy in break-up reactions for seen at R^{3}B.

In Figure 6.34 a comparison of the spacial distribution between the hits that provides the biggest β and the hits that provides the smallest time for the 3 mm glass thickness geometry is shown.

As it can be seen in the comparison of the spacial distribution, the hits that provide the biggest β are more dispersed in the detector and occur at a bigger depth, as shown in the lower left of the Figure 6.34. However, the coordinate with the largest influence in the calculation of the momentum is the z coordinate, since the velocity of the neutron is calculated using:

$$V_n = \frac{d_n}{t_d} = \frac{\sqrt{(x_d - x_t)^2 + (y_d - y_t)^2 + (z_d - z_t)^2}}{t_d} \tag{6.3}$$

where x_d, y_d and z_d are the coordinates of the detected particle and the x_t, y_t and z_t are the origin of the incoming neutron detected at time t_d. Since the detector is placed at 35 m from the neutron source in z, the z coordinate will have the largest influence in the momentum reconstruction.

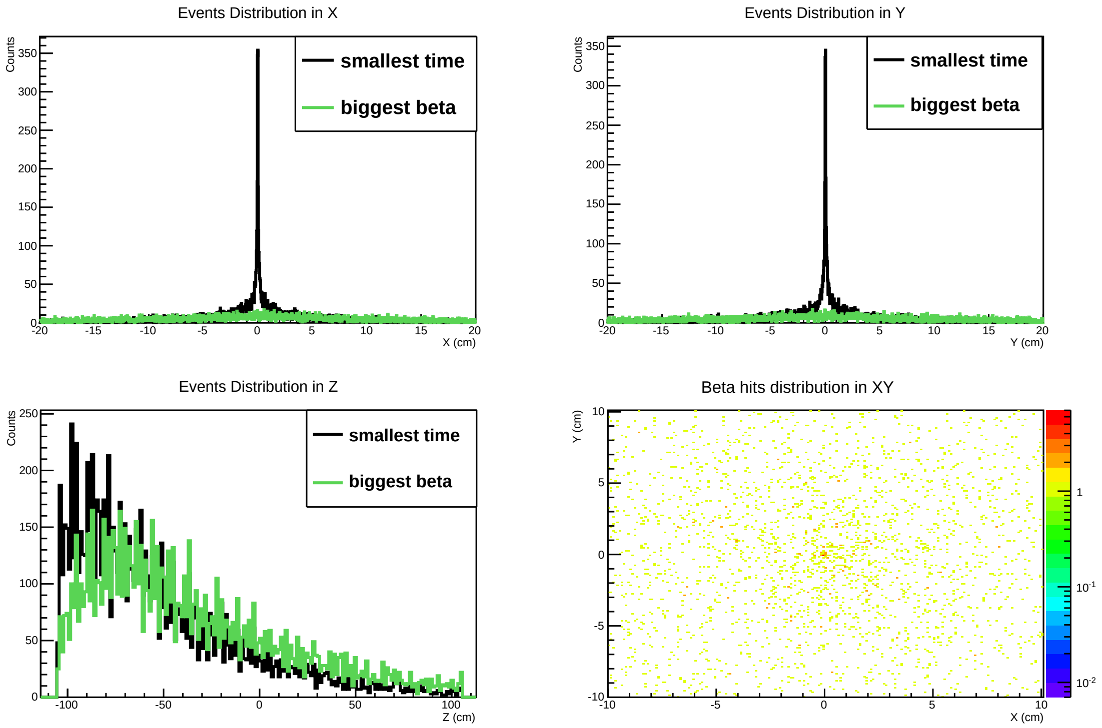

Figure 6.34: Comparison of the spacial distributions in x (top left), y (top right) and z (bottom left) of the hits in the detector for the hits that provide the biggest β and the hits that provide the smallest time. At the bottom right a two-dimensional histogram for the xy spacial distribution of the hits that provide the biggest β is presented. All the spectra corresponds to the 3 mm glass geometry.

To better characterize the events that provide the biggest neutron velocity is important to realize which particles are responsible for the hits that provide the biggest β .The probability of each kind of particle to provide the biggest β per event is listed in Table 6.16.

Comparing these results with those presented in Table 6.7, there is not a significant difference between in the probability that a particular kind of particles provides the first hit or the biggest β.

Table 6.16: Probability for each kind of particle to provide the biggest β per event for the all detector configurations.

	1 mm 300 planes	**2 mm 150 planes**	**3 mm 100 planes**	**4 mm 75 planes**	**5 mm 60 planes**
Protons	70.34%	72.30%	72.81%	73.66%	74.50%
Elect. + Posit.	24.89%	22.85%	22.38%	21.33%	20.54%
Other particles	4,37%	4.2%	3.57%	3.94%	3.79%

6.8.3 Two possible analysis choices: a comparison

With the two discussed analysis choices, a comparison for all geometries was performed for the $\Delta p = p_{init} - p_{reconst}$. The initial neutron momentum of the simulated neutrons was 995 MeV/c. In Figure 6.35 a comparison of the momentum reconstruction by the first hit per neutron in the detector for all the detector geometries is shown.

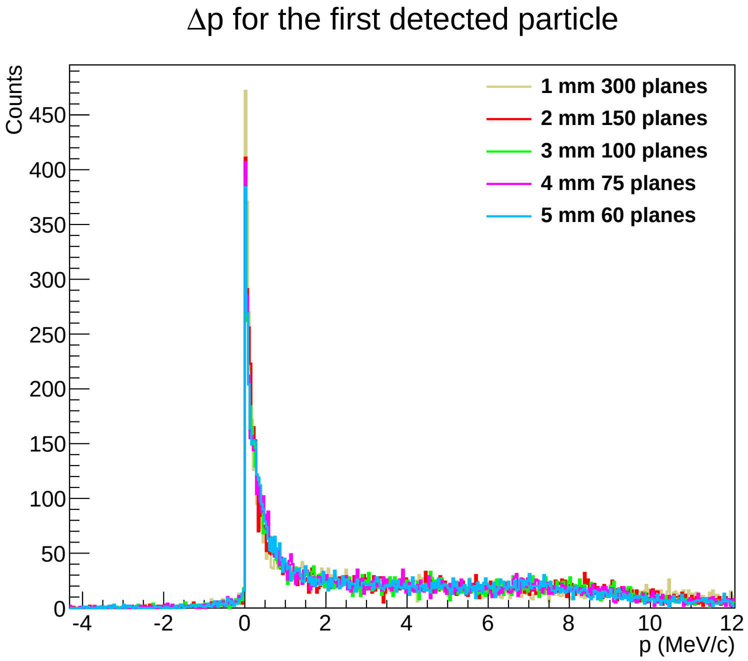

Figure 6.35: Comparison of the difference between the initial and the reconstructed momentum derived using the first hit per neutron in the detector for all detector geometries.

As it can be seen, the geometry of the detector does not have a large influence in the momentum reconstruction for this analysis choice, although it can be noted that the maximum at $\Delta p = 0$ MeV/c is larger for the geometries with thinner glass plates.

An equivalent result considering the other choice of analysis for the momentum reconstruction,i.e., choosing the hit that provides the biggest β, is presented in Figure 6.36.

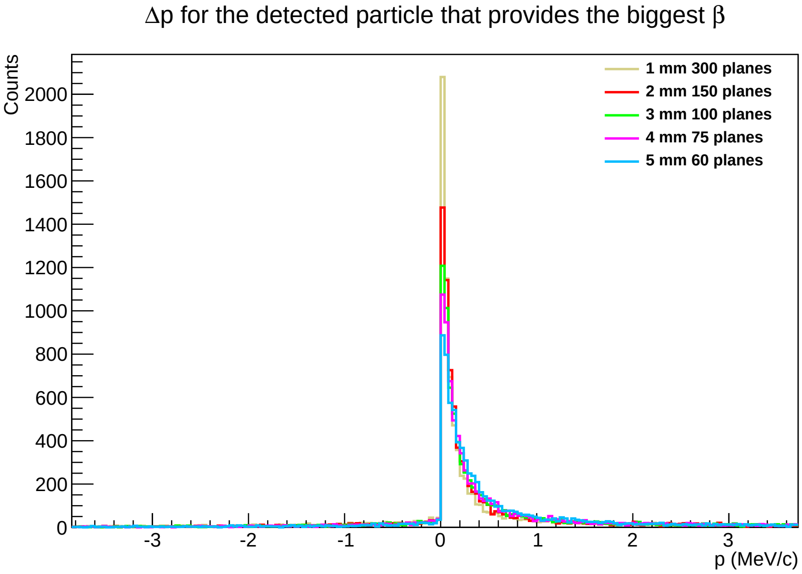

Figure 6.36: Comparison of the difference between the initial and the reconstructed momentum derived using the biggest β hit for all the detector geometries.

Using this choice of analysis to reconstruct the neutron momentum, it can be noted a larger sensitivity on the detector configuration in efficiently reconstructing the momentum. As for $\Delta p = 0$ the geometries with thinner glass provide a higher number of neutrons with correctly reconstructed momentum.

For a better comparison of the two analysis choices Figure 6.37 shows Δp for the 3 mm glass thickness geometry[1].

As it can observed in the comparison, the momentum is more effectively reconstructed using the biggest β. It certainly can be concluded that the first hit is not

---

[1] For the others geometries see Appendix A.11

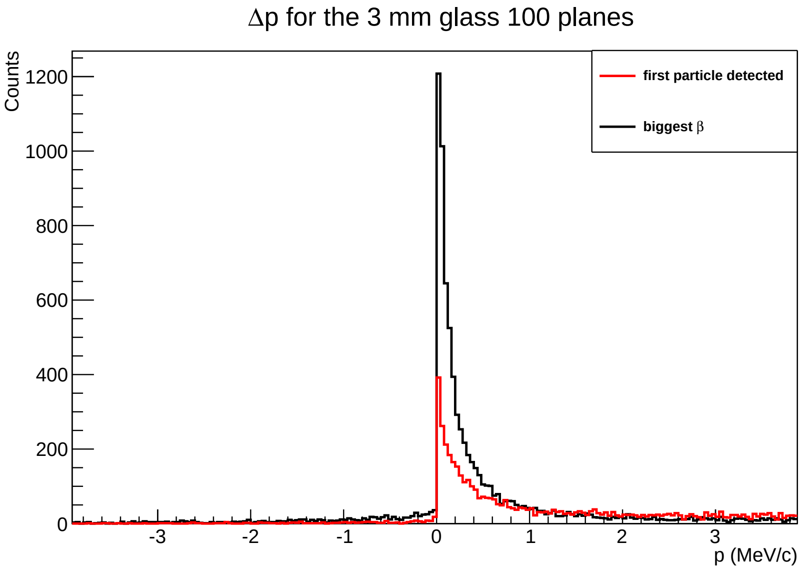

Figure 6.37: Comparison of the analysis methods of the momentum reconstruction for the 3 mm glass 100 planes geometry.

always the hit that provides the best information to reconstruct the momentum. There are in most cases hits that provide value for the velocity calculation closer to the neutron velocity, resulting in a better reconstruction of the momentum of the neutron.

7

Physics case

As mentioned in the design goals of NeuLAND (see section 1.5.1), one of the requirements of the detector is to provide an energy resolution of about 20 keV at an excitation energy of 100 keV, being the detector placed at 35 m and a neutron energy of about 500 AMeV. In order to evaluate the performance of the detector regarding the excitation energy resolution, simulations of a real case experiment of a Coulomb dissociation reaction has been performed.

7.1 Coulomb dissociation method

The Coulomb Dissociation (CD) method is based on the fact that a projectile passing by a target nucleus sees the Coulomb field of the nucleus. Coulomb excitation reactions serve as one of the most powerful spectroscopic tools for investigating excited states of exotic nuclei. In a CD reaction, the projectile is excited by the Coulomb field of a high-Z target. A representative picture of the Coulomb excitation is shown in Figure 7.1. As illustrated in the Figure, a Lorentz-contracted electric field acts on a projectile nucleus when the projectile passes fast by a high-Z target at an impact parameter b. In this electric field, the incident nucleus absorbs a virtual photon. Hence, Coulomb excitation can be expressed as a photo-absorption process induced by a virtual photon.

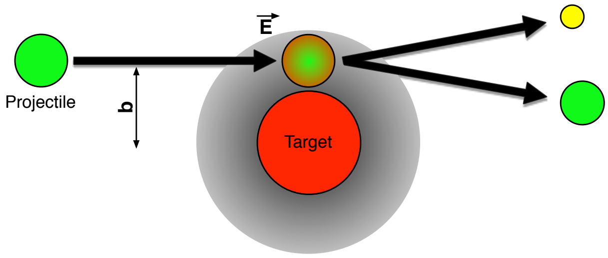

Figure 7.1: Schematic drawing for Coulomb excitation process. The electric field $\vec{E}$, is provided in the projectile rest frame and is Lorentz-contracted in the beam direction. The final state is described as a dissociated state (Coulomb Dissociation).

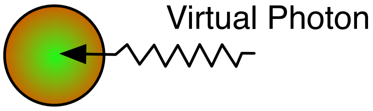

Figure 7.2: The electric field from the target is interpreted as a virtual photon flux.

In a CD experiment one aims at reconstructing the properties of the excited incoming beam by detecting the emitted fragments and reconstructing their relative energy. Considering the $^{132}Sn(\gamma,n)\ ^{131}Sn$ CD reaction, the objective is to detect both of the outgoing fragments and measure their respective momenta allowing the indirect measurement of the relative energy between their centre-of-mass using invariant mass relations. This is schematic presented in Figure 7.3.

Using relativistic relations between the momentum and the energy of a particle, the energy of the system $^{131}Sn + n$ is defined in the laboratory frame as:

$$E_{Lab} = \sqrt{P^2_{131Sn} + m^2_{131Sn}} + \sqrt{P^2_n + m^2_n} \tag{7.1}$$

being the $m_{^{131}Sn}$ and m_n the masses of the outgoing fragments.

The invariant mass of the system is therefore given by:

$$m_{inv} = \sqrt{(E_{^{131}Sn} + E_n)^2 - (\vec{P}_{^{131}Sn} + \vec{P}_n)^2} \tag{7.2}$$

being the $E_{^{131}Sn}$ and E_n the total energy of the system $^{131}Sn + n$.

The relative kinetic energy will be given by the mass difference of the whole system:

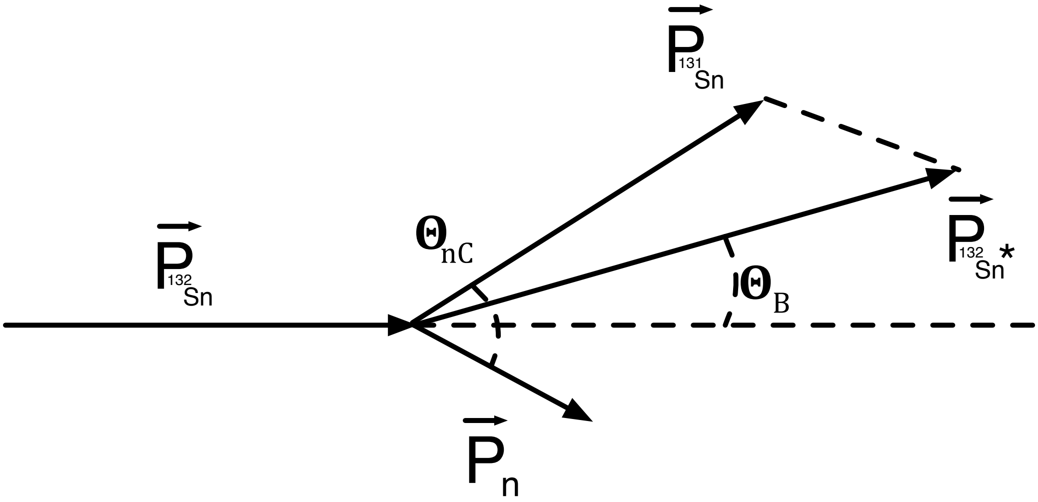

Figure 7.3: Representation of the momenta of the outgoing fragments in a $^{132}Sn(\gamma,n)\ ^{131}Sn$ CD reaction. The $\vec{P}_{^{132}Sn^*}$ is the vectorial sum of $\vec{P}_{^{131}Sn} + \vec{P}_n$. The scattering angle Θ_B is the angle between the $\vec{P}_{^{132}Sn}$ and $\vec{P}_{^{132}Sn^*}$. The Θ_{nC} is the angle between the $\vec{P}_{^{131}Sn}$ and $\vec{P}_n$.

$$E_{rel} = m_{inv} - m_{^{131}Sn} - m_n \tag{7.3}$$

The relative kinetic energy is the excitation energy of the incoming nucleus. If the nucleus is in the ground state, the invariant mass is zero. If on the contrary the incoming nucleus is in an excited state, the invariant mass is bigger than zero and the difference of masses will give us a measure of the excitation energy.

7.2 The $^{132}Sn(\gamma,n)\ ^{131}Sn$ simulated reaction

In order to evaluate the performance of the detector regarding the resolution of the excitation energy, simulations of a Coulomb Dissociation reaction of the ^{132}Sn nucleus were performed. For the simulation of this reaction only the 3 mm glass thickness with 100 planes geometry has been considered since it was the geometry with better multi-hit capability (although this property is not used at this stage). The simulations performed were based on several event files produced within the NeuLAND collaboration. These event files consisted in the momentum components of the final state of the $^{132}Sn(\gamma, n)$ ^{131}Sn reaction. For each event, two particles resulted from the reaction: a ^{131}Sn nucleus and a neutron. In the simulations other already developed geometries were used: the ALADIN magnet, to deflect the heavy-fragments and the TOF-Wall for its detection. A schematic view is shown in Figure 7.4.

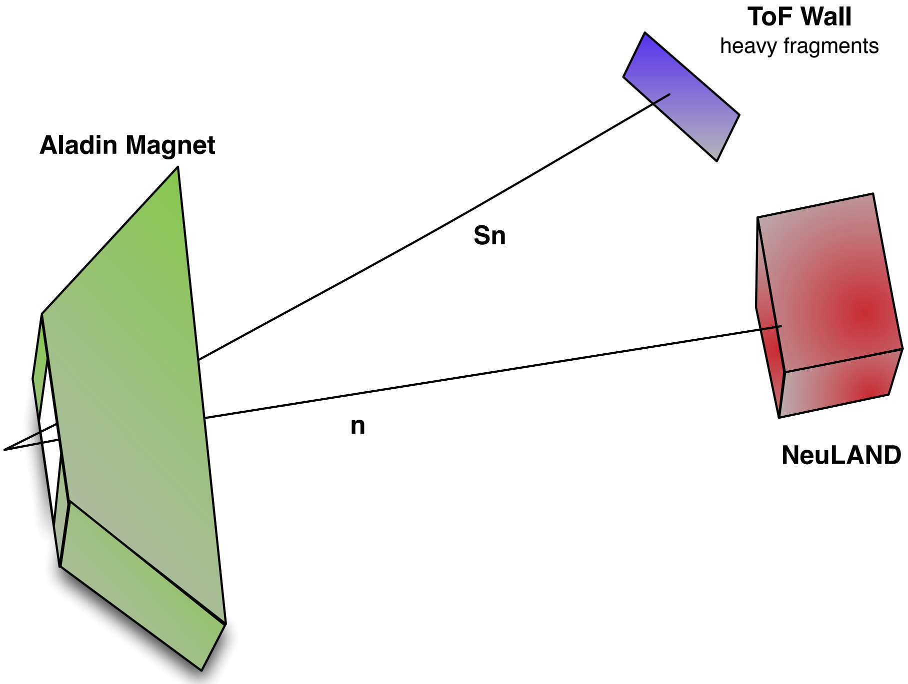

Figure 7.4: Schematic drawing of the simulation setup for the $^{132}Sn(\gamma, n)$ ^{131}Sn reaction.

The simulations were performed using 10000 events with the GEANT4 engine at 200, 600, and 1000 MeV at two different distances, 12.5 m and 30 m and with air as the medium in the cave. In neither case was considered the multi-hit capability, were always considered the arrival of just one neutron. The simulations were performed for an excitation energy of the fragment of 100 keV.

7.3 Excitation energy results

The excitation energy was calculated using the initial moment of the heavy-fragment and the neutron momentum reconstructed by our detector. In Figures (7.5, 7.6 and 7.7) the results of the reconstructed excitation energy, considering the two choices of the momentum reconstruction analysis for all the considered energies and distances from target, are presented.

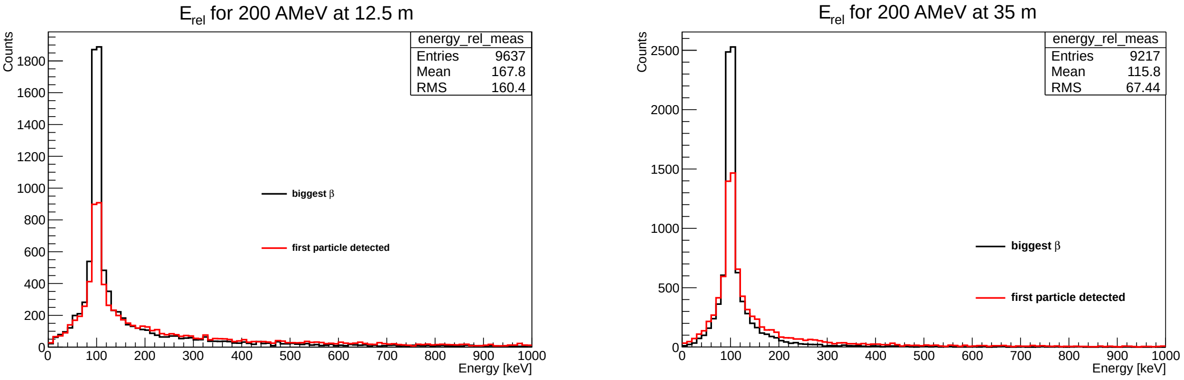

Figure 7.5: Excitation energy of ^{132}Sn at 200 AMeV using the two different methods for the momentum reconstruction of the neutron with the detector placed at 12.5 m (left) and 35 m (right) from the target. The simulated excitation energy of the nucleus corresponds to 100 keV.

As a result, we can see that the excitation energy is better reconstructed by using the information from the hit that provides the biggest β. We can also see that the efficiency decreases for higher beam energies and with the proximity to the target. In addition, we can see that for the same energy, the number of entries is not the lower for the larger distance. This fact is explained by the air in the cave, since the larger the distance to the detector, the bigger the probability for the neutrons to interact with the air and thus not reaching the detector.

For a better comparison and to realize the performance in terms of energy resolution, gaussian fits to the excitation energy distributions were performed. The results are listed in Table 7.1.

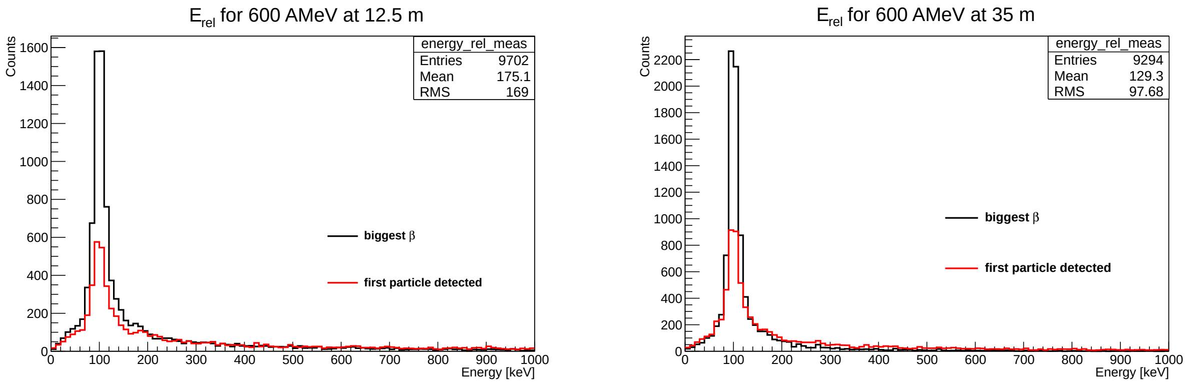

Figure 7.6: Excitation energy of ^{132}Sn at 600 AMeV using the two different methods for the momentum reconstruction of the neutron with the detector placed at 12.5 m (left) and 35 m (right) from the target. The simulated excitation energy of the nucleus corresponds to 100 keV.

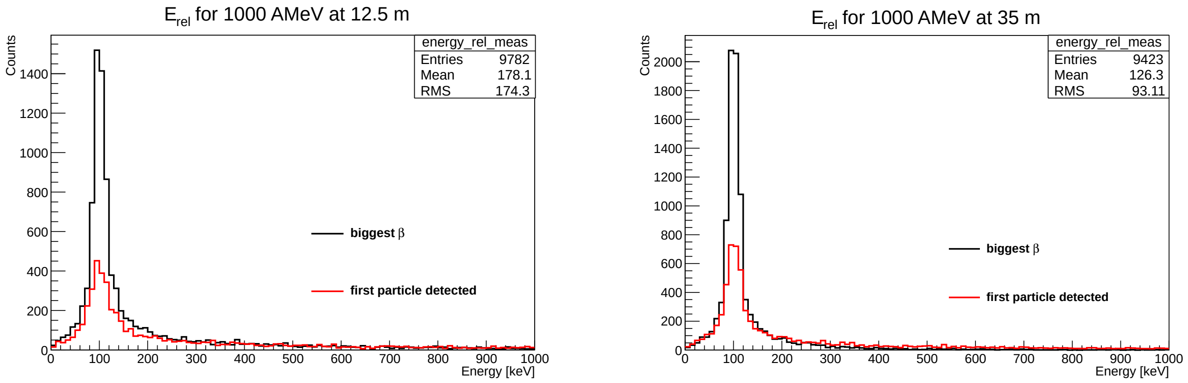

Figure 7.7: Excitation energy of ^{132}Sn at 1000 AMeV using the two different methods for the momentum reconstruction of the neutron with the detector placed at 12.5 m (left) and 35 m (right) from the target. The simulated excitation energy of the nucleus corresponds to 100 keV.

The widths of the distributions are larger for higher energies. However, there is not a significant difference considering the sigma values for the two distances at the same beam energy. This fact is explained by the ideal detection conditions considered at this stage, i.e., in the simulations neither time nor space resolutions have been implemented at this stage.

Table 7.1: Sigma and mean values of the gaussian fits made to the excitation energy histograms.

	12.5 m		35 m	
Energy	**sigma (keV)**	**mean value (keV)**	**sigma (keV)**	**mean value (keV)**
200 MeV	9	100	9	100
600 MeV	11	100	11	100
1000 MeV	16	100	13	100

7.4 Real conditions

In order to reproduce the spacial and time resolutions of the detector, random distributions were applied to the position coordinates (x, y and z) and to the time provided by the hits in the detector. As for the x and z coordinates, a square random distribution of 3 cm (size of the readout strip) and 1.075 cm for the z (half size of the plane thickness) was applied to x and z coordinates respectively. For the y and for the time, gaussian distributions of $\sigma_y = 1$ cm and $\sigma_t = 80$ ps were applied, respectively [FON-11].

Figure 7.8 shows a comparison between the momentum reconstructed with the hit that provides the biggest β in the ideal case to the momentum reconstructed with real conditions applied for two different distances from the target for a beam energy of 600 AMeV.

The diagrams show the effect of the real conditions applied to the momentum reconstruction. As it can be seen, the reconstructed momentum becomes wider and smaller due to the uncertainties applied to the coordinates and time. However, the mean value of the distribution remains well defined. Figures 7.9, 7.10 and 7.11 show the excitation energy spectrum of 200, 600 and 1000 AMeV at 12.5 and 35 m from the target calculated with the momentum reconstructed with the already mentioned uncertainties.

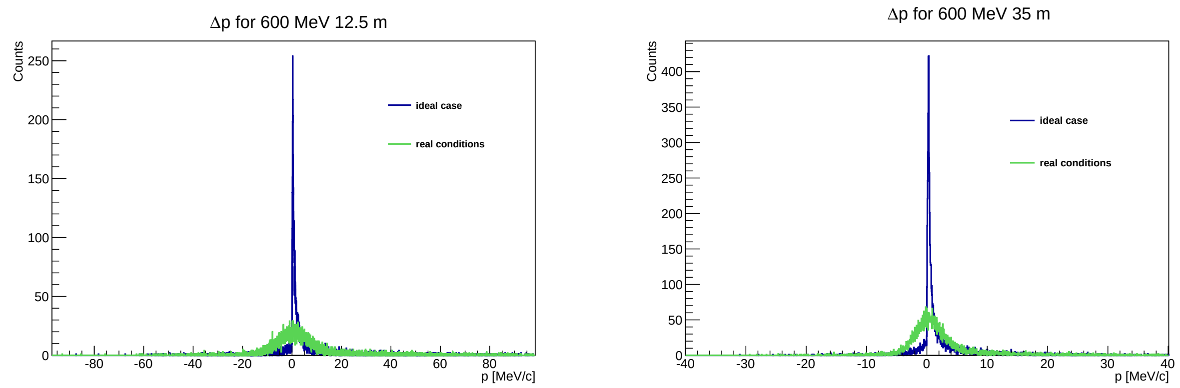

Figure 7.8: Reconstructed momentum considering the hit that provides the biggest β for the ideal case and under real conditions. The energy of the beam was 600 AMeV. On the left panel the detector is placed at 12.5 m from the target and in the right panel the detector is placed at 35 m from the target.

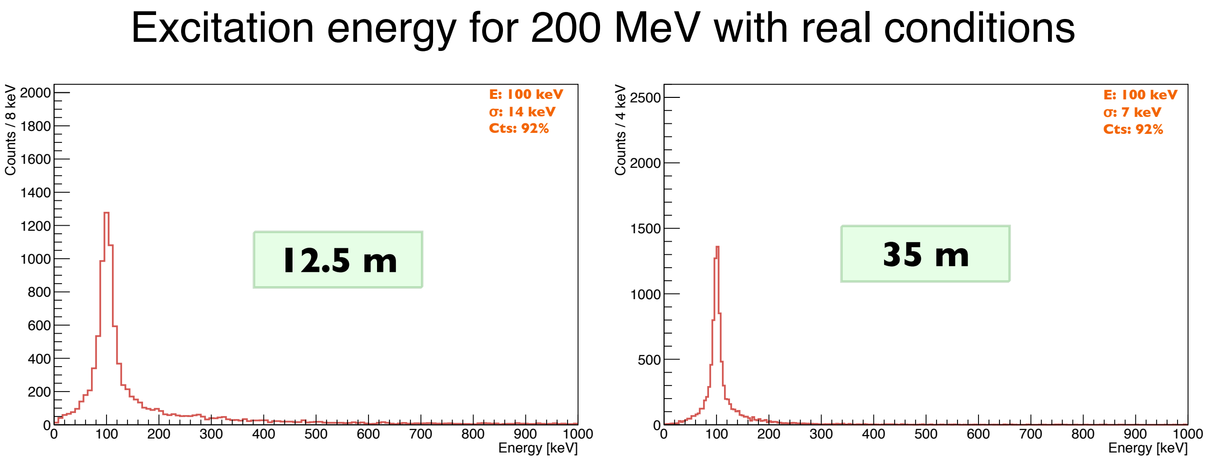

Figure 7.9: Excitation energy spectra of E_{rel} = 100 keV and 200 AMeV beam energy, reconstructed using the hit that provides the biggest β, with the detector placed at 12.5 m (left) and 35 m (right) from the target.

The Figures also contain the mean value of E_{rel} and the standard deviation σ of gaussian fits made to the spectra. The total number of events in the spectra normalized to the total number of simulated events (Cts) is also given.

As it can be seen, the definition of the centroid of the excitation energy distribution worsens with increasing beam energy and with the proximity to the target, as compared to the case where no real conditions were applied. The uncertainties induced by the

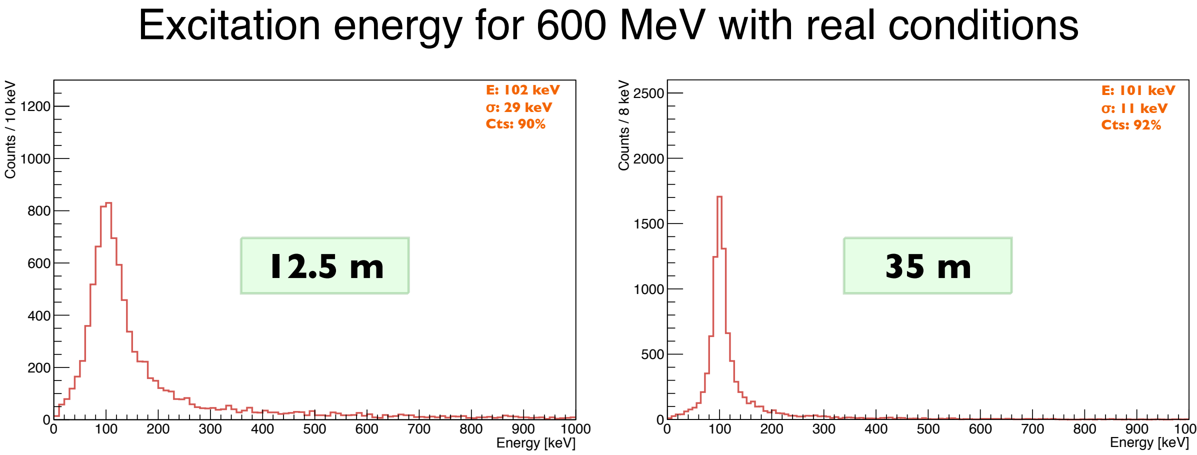

Figure 7.10: Spectrum of the excitation energy of 100 keV for 600 MeV neutrons reconstructed by the hit that provides the biggest β with the detector placed at 12.5 m (left) and 35 m (right) from the target.

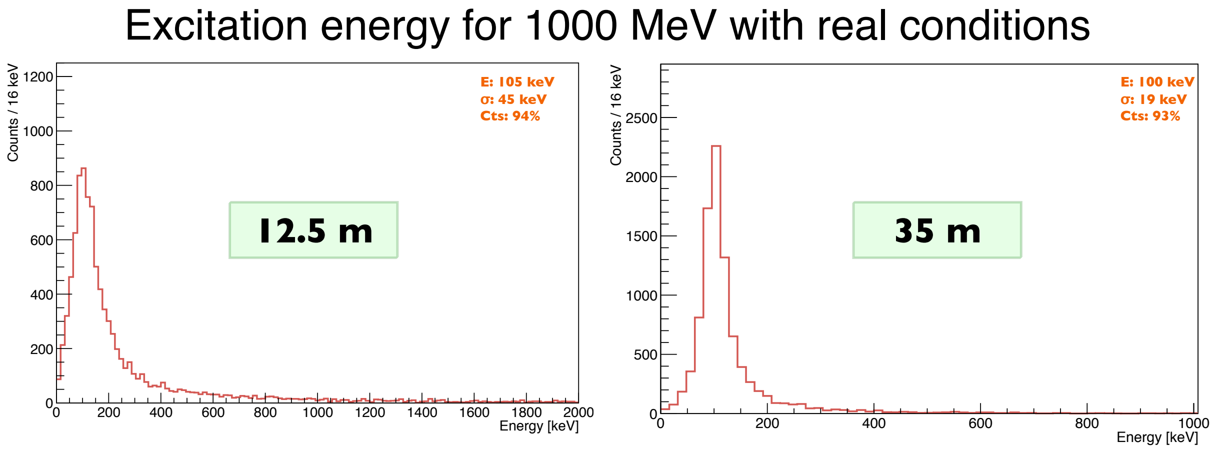

Figure 7.11: Spectrum of the excitation energy of 100 keV for 1000 MeV neutrons reconstructed by the hit that provides the biggest β with the detector placed at 12.5 m (left) and 35 m (right) from the target.

intrinsic characteristics of the RPCs are more relevant for small distances to the target. The worst obtain result corresponds to the highest simulated energy and to the shortest distance with a resolution of $\sigma = 45$ keV.

Overall the detector based on RPC provides a very good energy resolution and efficiency in the reconstruction of the excitation energy for the case where only one neutron is emitted.

8

Prototype simulations

This work has been performed aiming at the development of a prototype by the LIP-Coimbra group, that will be tested in an deuteron-breakup reaction experiment at GSI using “monoenergetic” neutrons with an energy range of 200-800 MeV.

The experiment *S406* aims at detecting neutrons resulting from a quasi-free scatering reaction of a deuteron beam delivered by the SiS18 on protons using a CH_2 target [BOR-10]. The experiment will allow to test the time response of the detector as well the efficiency as a function of the beam energy. Four different energies (200, 300, 500 and 800 MeV) will be studied. The experience is scheduled for the first half of 2012.

8.1 Detection efficiency

The prototype will have a total active area of 200×50 cm^2. As already shown, the detector efficiency will depend on the total number of consecutive RPC planes it will be made of. In order to determine the number of planes needed to achieve a reasonable detection efficiency, several simulations were preformed considering the geometry presented in Figure 8.1 and considering different number of planes.

The simulations were performed with the GEANT4 engine considering neutrons of

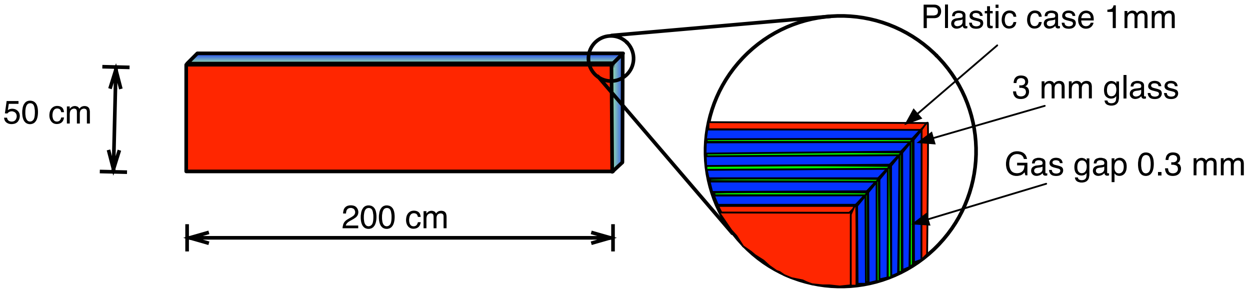

Figure 8.1: Schematic drawing of the geometry of one module of the prototype.

400 MeV ($p = 955$ MeV/c) generated at 35 m from the prototype.

In Figure 8.2 the one neutron detection efficiency for the prototype as a function of the number of planes is shown.

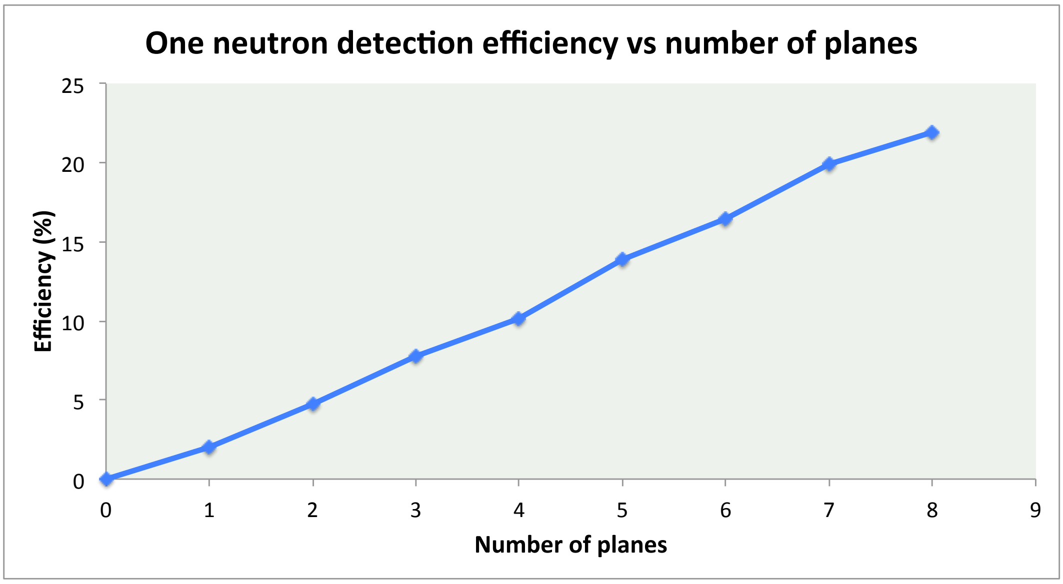

Figure 8.2: Efficiency of one neutron detection of the prototype in function of the number of planes for 400 MeV neutrons.

As it can be seen, an efficiency of about 22% is reached using 8 planes. This will allow a reasonable efficiency for the test.

Considering the geometry of the prototype with 8 planes, different energies of the incoming neutrons were simulated. The energies considered were the ones proposed by

[BOR-10],i.e., 200, 300, 500 and 800 MeV. Figure 8.3 shows the one neutron efficiency as a function of the kinetic energy of the incoming neutrons.

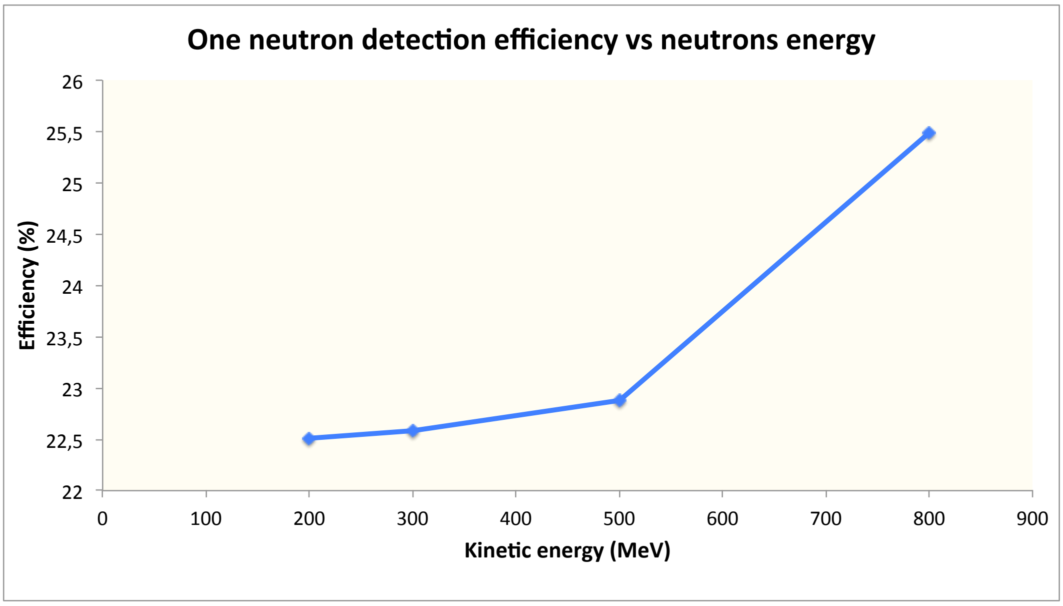

Figure 8.3: Efficiency of one neutron detection of the prototype as a function of the neutron kinetic energy.

As it can be seen, the efficiency increases with increasing kinetic energy. It can also be noticed that for the lowest energy the efficiency of the detector is still above 22%.

8.2 Momentum reconstruction

Once the geometry of the prototype has been defined it is important to realize how the momentum of the neutron is expected to be reconstructed during the test.

Considering the two choices for the momentum reconstruction previously studied (see section 6.8.1), the momentum of the neutron was reconstructed under ideal conditions. The result is shown in Figure 8.4.

As it can be seen, the analysis considering the biggest β still provides a better reconstruction of the neutron momentum.

Considering this type of analysis, and taking into account a time resolution of

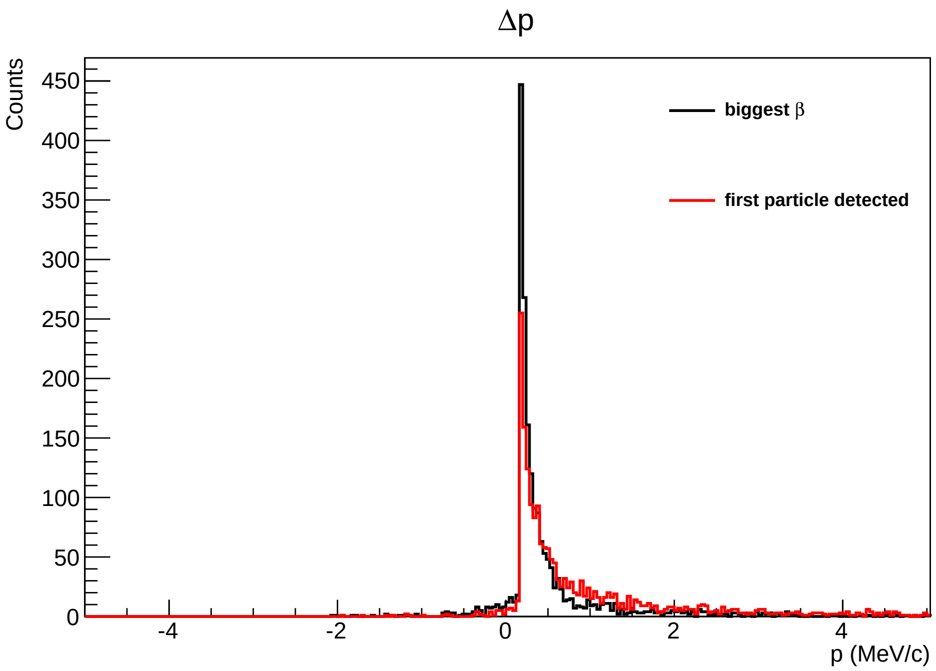

Figure 8.4: Difference between the initial and the reconstructed momentum for the two choices of momentum reconstruction for the prototype in the case of 400 MeV neutrons generated at a distance of 35 m. The analysis was performed without time and space resolutions implemented.

$\sigma_t = 80$ ps, a x coordinate resolution of 3 cm, $\sigma_y = 1$ cm for the y resolution and half size of a plane thickness of 1.075 cm for the z coordinate, the momentum of the neutron was reconstructed and is presented in Figure 8.5.

As it can be seen, the momentum is correctly reconstructed with a width of $\sigma_p =$ 1.13 MeV/c. Based on the simulation results, it will be possible to detected about 20% of the neutrons that will reach the prototype, and it will be possible to correctly reconstruct its momentum with enough statistics.

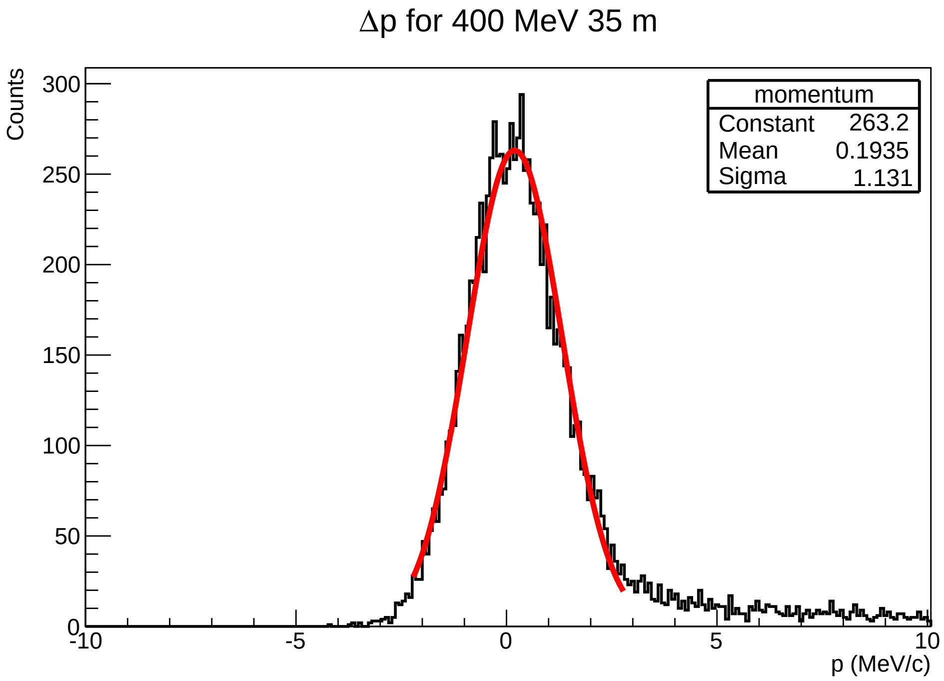

Figure 8.5: Reconstructed momentum of the neutron by the prototype for 400 MeV neutrons at 35 m using the biggest β approach.

9

Final considerations and future work

The present work concentrated of the evaluation of the simulated performance of a Time-of-Flight neutron detector based on Resistive Plate Chambers. The results obtained for an iron-less concept for a RPC showed a high efficiency and very good momentum resolution in the detection of one neutron events for a wide energy range (between 200 MeV and 1 GeV).

It was shown that the main particles responsible of depositing energy in the detector are protons and electrons/positrons. The behavior of the particles in the detector is different as well as their initial energy. Protons activate more gaps, and thus more planes, than the electrons, which deposit energy in just a few gaps. The multiplicity of detected electrons/positrons is larger than that of protons; however, protons are the responsible for the majority of the detector hits. It was also shown the importance of single gap multiplicity for the total efficiency.

One important aspect of this work that needs to be improved is the multi-hit recognition analysis. As it was shown in our multi-hit recognition analysis, the detection efficiency of multi neutrons reaching the detector suffers a considerable decrease with the increase the neutron number. It is mandatory to develop an intelligent and effective clusterization analysis to evaluate the response of the iron-less RPC in the reconstruction multi neutron hits. At this stage the configuration with 3 mm of glass plates configuration turned to be the best geometry for possible future multi neutron hit reconstruction. Another advantage of using the 3 mm glass thickness is the easily handling of the plates, which makes the construction process easy and cost effective.

As for the reconstruction of the momentum of the neutron, two different approaches were adopted: using the first particle that deposits energy in the detector, and choosing the particle that provides the biggest velocity of the neutron (biggest β). It was concluded that for neutron multiplicity of one, the biggest β approach is considerably better and reconstructs the neutron momentum more efficiently and correctly than the first hit approach. However, as the hit that provides the biggest β is most of times given to a further depth in the detector, the particle that provides the hit sufferers a larger dispersion compared to the particle that provides the first hit, which happens more probably closer to the original trajectory of the neutron. Thus, although the biggest β analysis provides a better reconstruction of the momentum, a wrong reconstruction of the neutron trajectory results in a incorrect determination of the excitation energy. A better analysis approach trying to combine all available information is required. Overall, the neutron reconstruction by the different detector geometries does not depend much on the detector geometry.

The simulated data was folded with the expected uncertainties in the determination of position and time. Under those conditions the reconstruction of the momentum and the excitation energy, presented an excellent efficiency and resolution for one neutron detection.

One of the goals of this work was to provide valid results to the LIP-Coimbra's group so they were able to start to build a prototype that would be tested in spring of 2012 at GSI. The simulations showed that the prototype needs to consist of 8 planes to reach an efficiency higher than 20% for the range of energies considered.

The simulations work needs to continue to trying to improves some analysis aspects and the creation of tools to analyze the data from the prototype.

Appendix A

Complementary histograms of the different iron-less concepts

A.1 Detected particles multiplicity

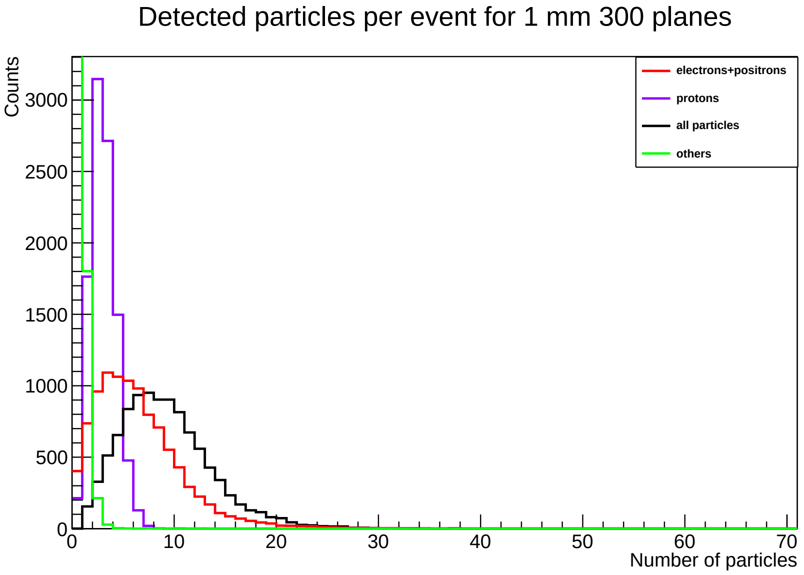

Figure A.1: Comparison of the detected particles multiplicity for 1 mm glass thickness with 300 planes.

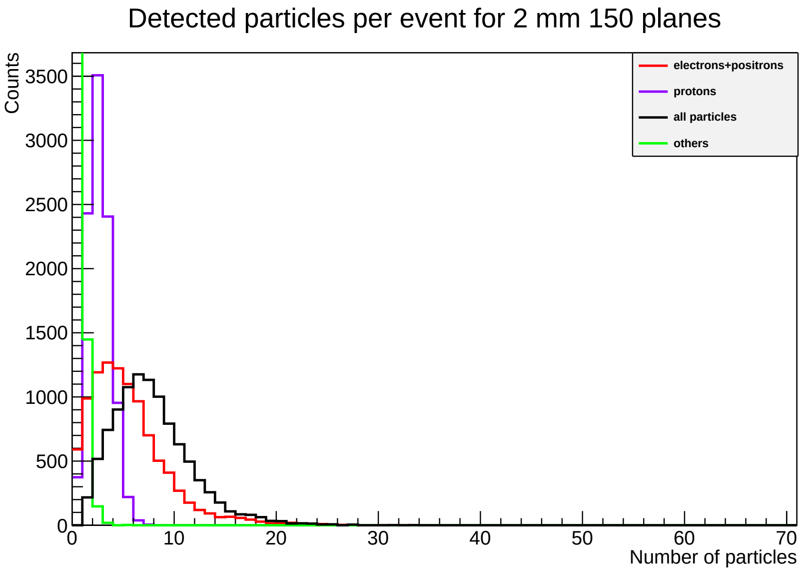

Figure A.2: Comparison of the detected particles multiplicity for 2 mm glass thickness with 150 planes.

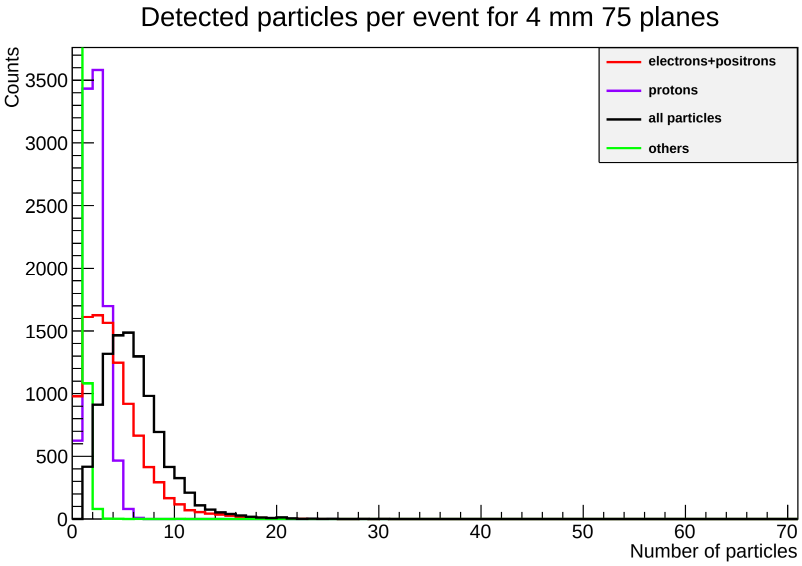

Figure A.3: Comparison of the detected particles multiplicity for 4 mm glass thickness with 75 planes.

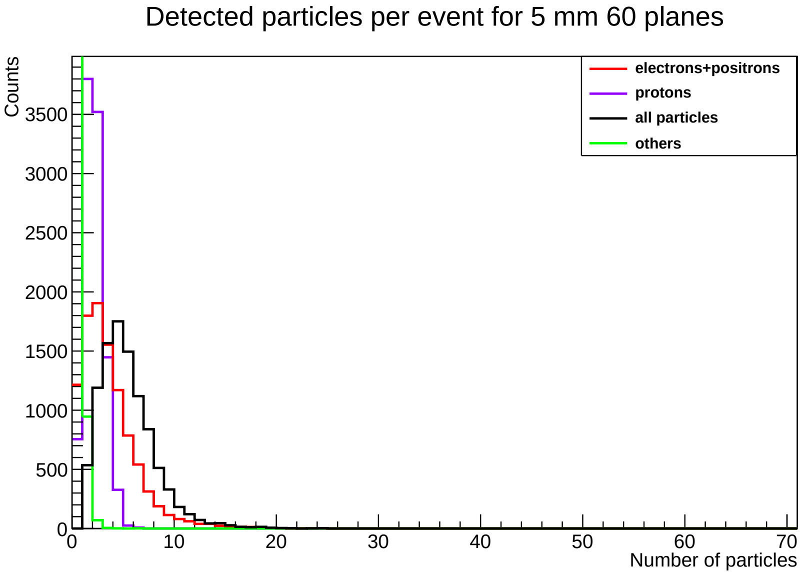

Figure A.4: Comparison of the detected particles multiplicity for 5 mm glass thickness with 60 planes.

A.2 Detected particles initial energy

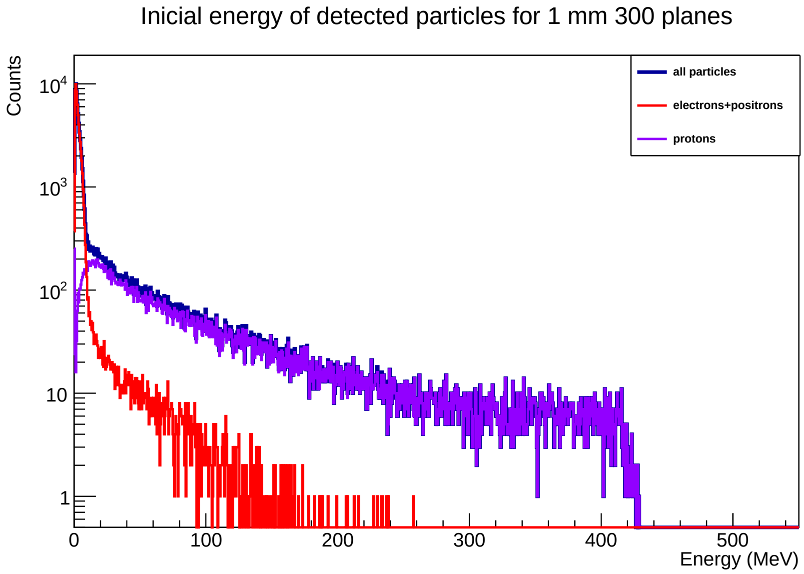

Figure A.5: Initial energy of the detected particles for 1 mm 300 planes geometry.

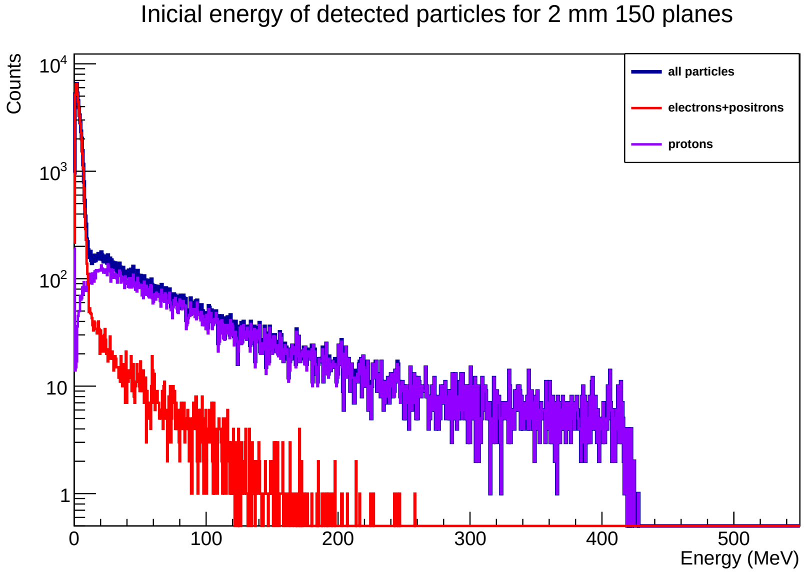

Figure A.6: Initial energy of the detected particles for 2 mm 150 planes geometry.

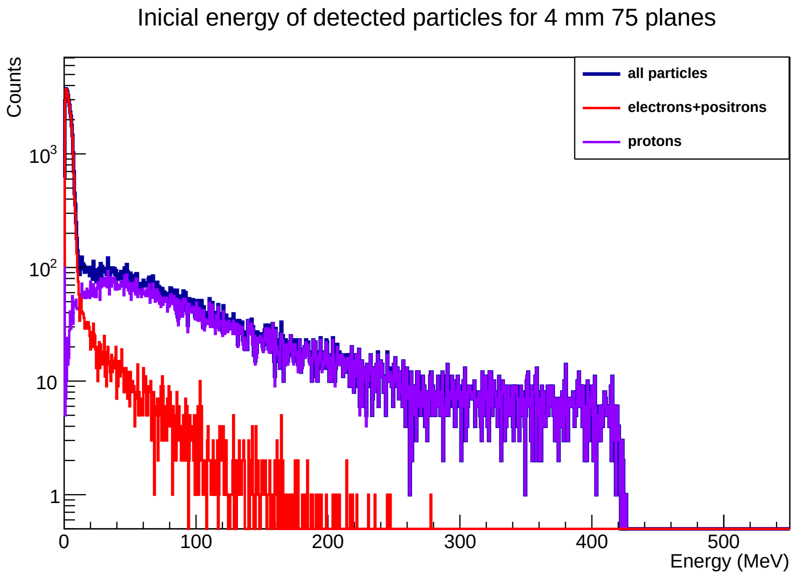

Figure A.7: Initial energy of the detected particles for 4 mm 75 planes geometry.

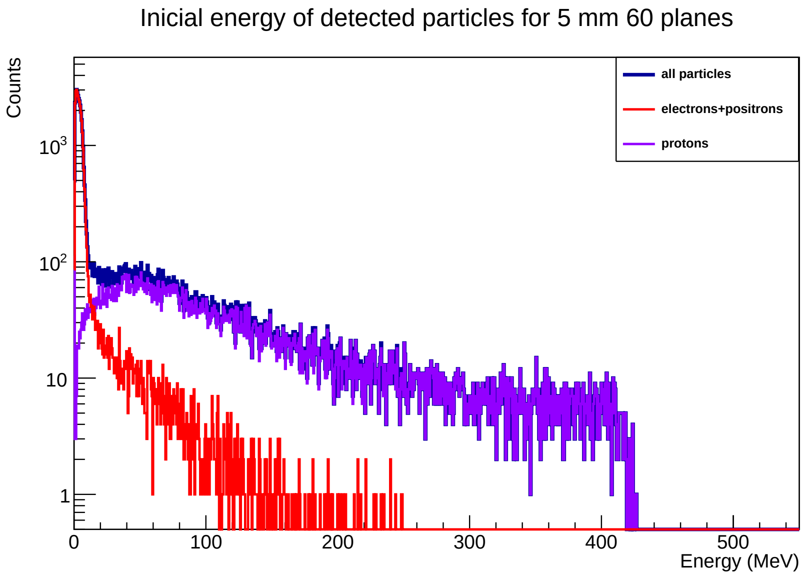

Figure A.8: Initial energy of the detected particles for 5 mm 60 planes geometry.

A.3 Energy loss distribution in the gaps

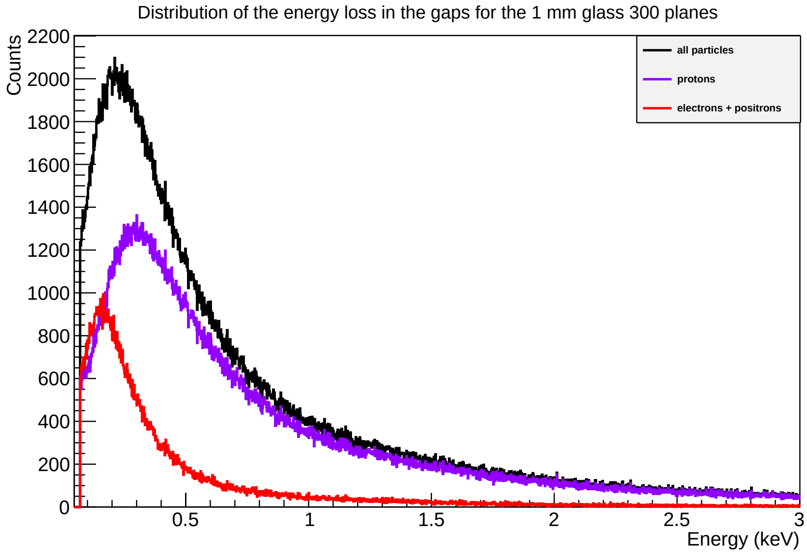

Figure A.9: Energy loss distribution for the 1 mm 300 planes geometry.

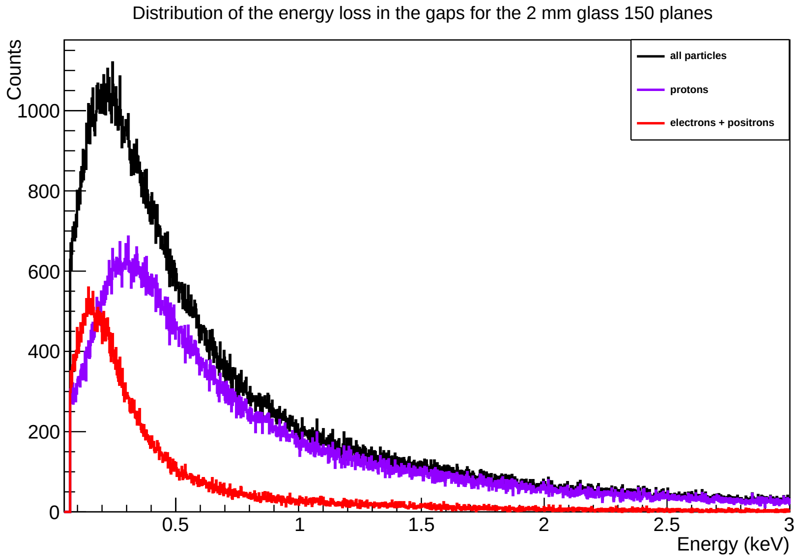

Figure A.10: Energy loss distribution for the 2 mm 150 planes geometry.

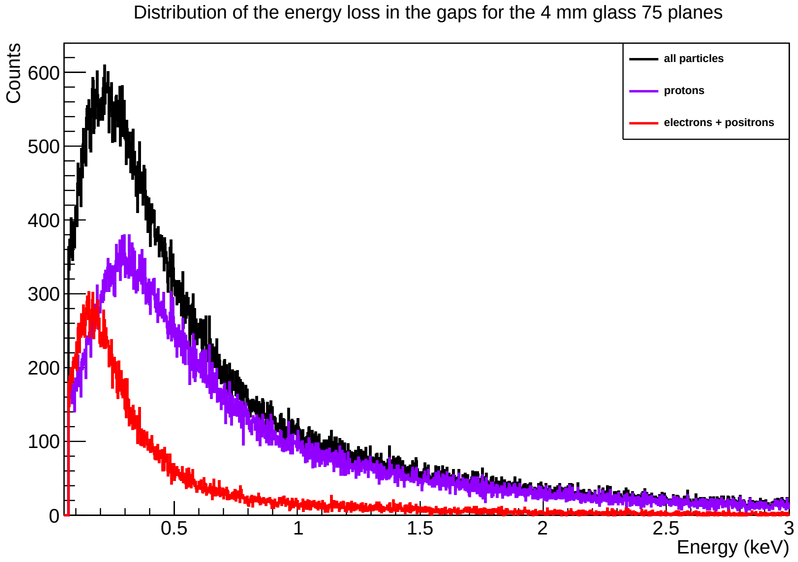

Figure A.11: Energy loss distribution for the 4 mm 75 planes geometry.

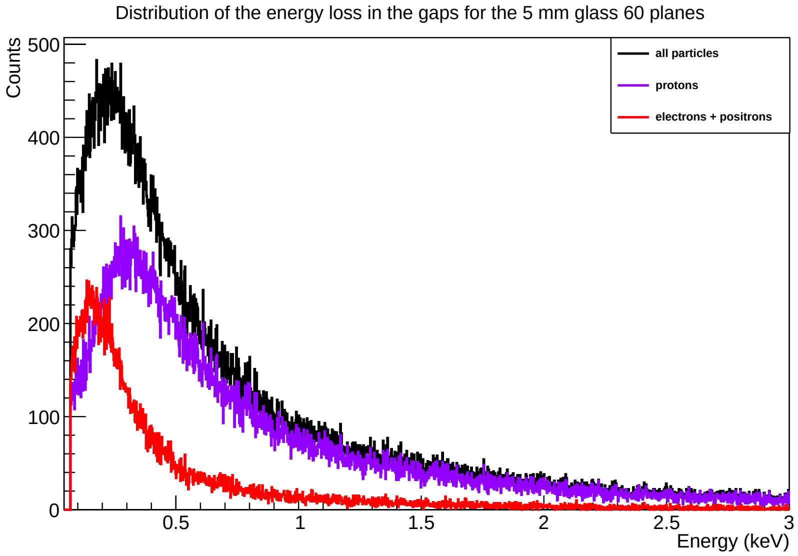

Figure A.12: Energy loss distribution for the 5 mm 60 planes geometry.

A.4 Crossed gaps by particle per event

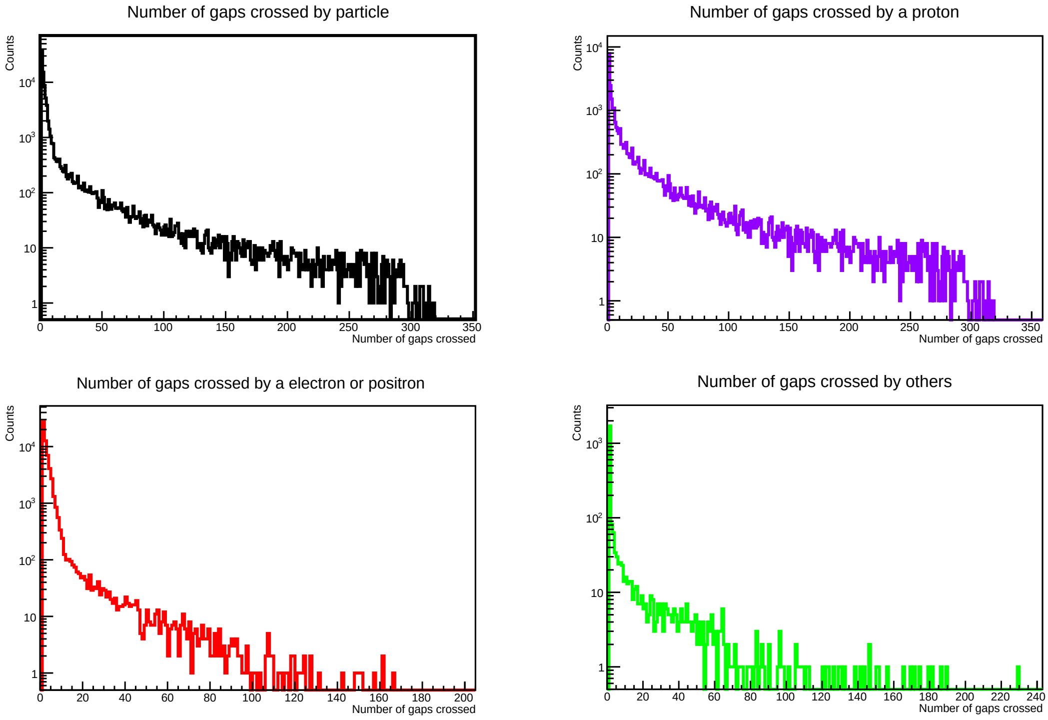

Figure A.13: Crossed gaps for each particle for the 1 mm glass thickness 300 planes geometry.

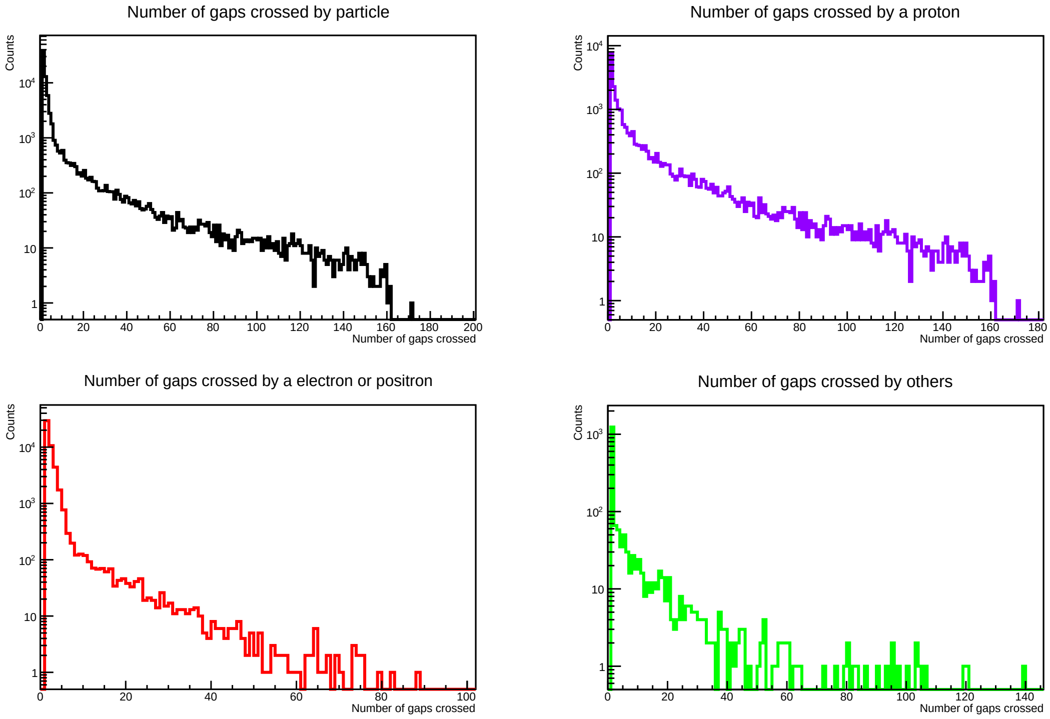

Figure A.14: Crossed gaps for each particle for the 2 mm glass thickness 150 planes geometry.

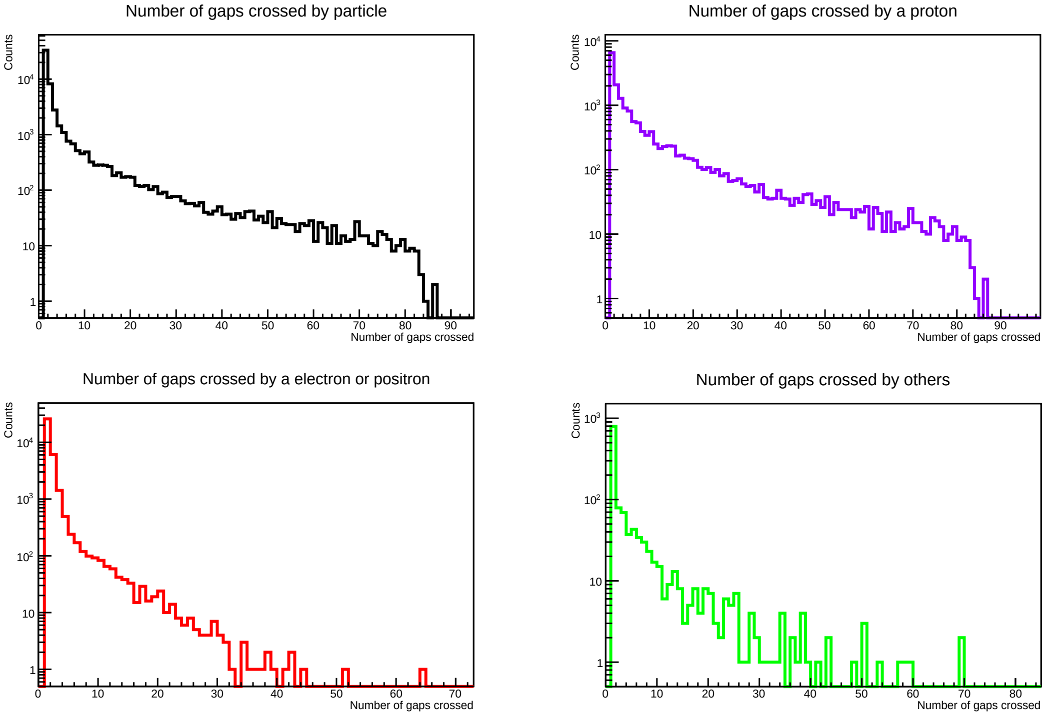

Figure A.15: Crossed gaps for each particle for the 4 mm glass thickness 75 planes geometry.

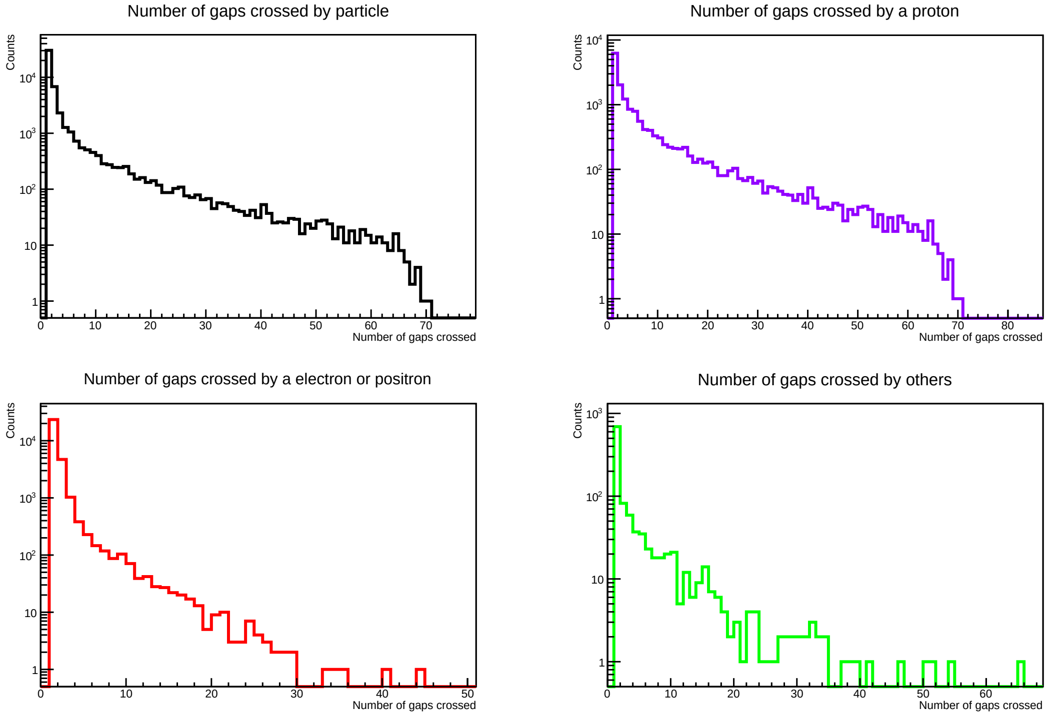

Figure A.16: Crossed gaps for each particle for the 5 mm glass thickness 60 planes geometry.

A.5 Spacial distributions of the first hit

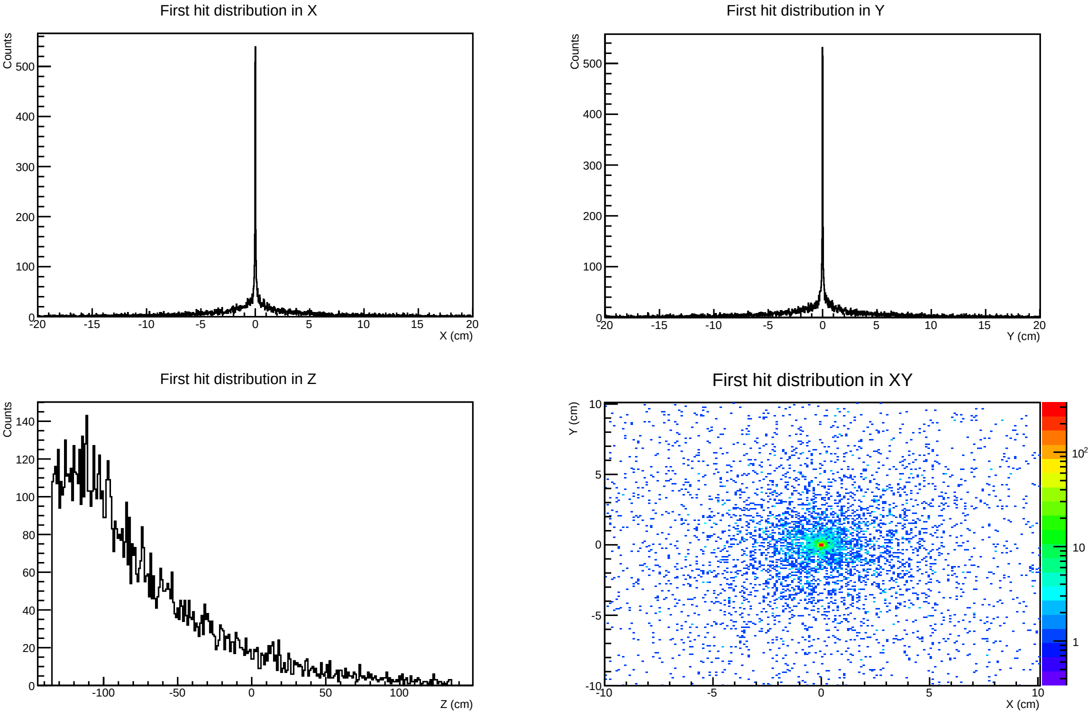

Figure A.17: Spacial distribution of the first hit on the detector for the 1 mm 300 planes configuration.

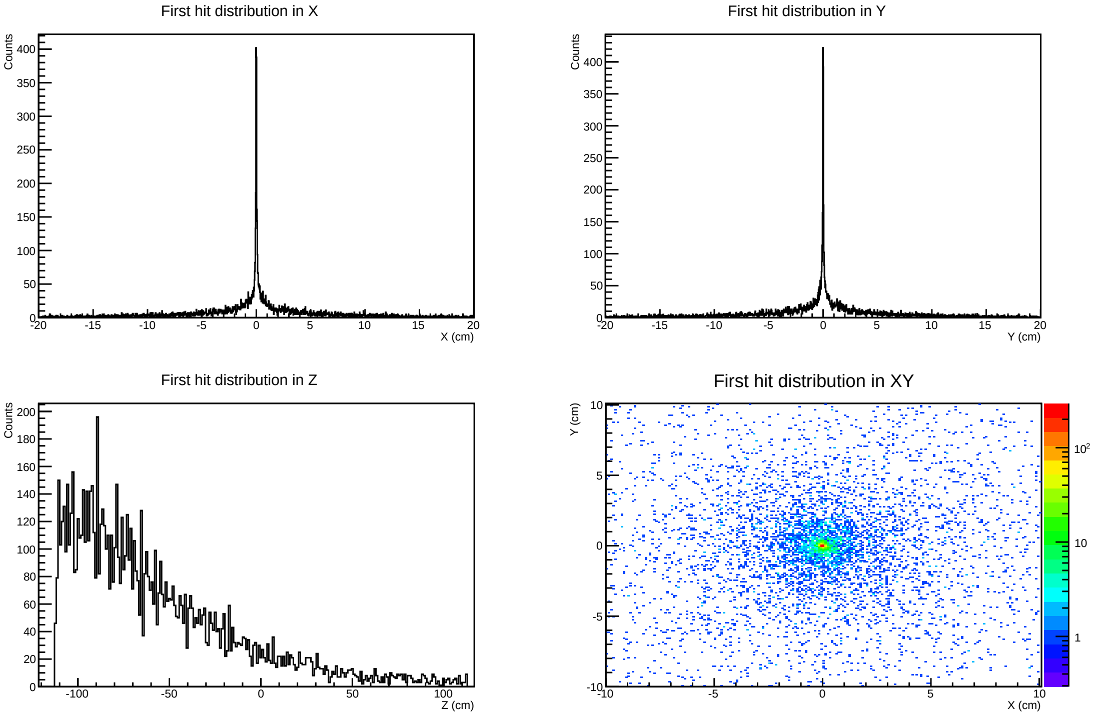

Figure A.18: Spacial distribution of the first hit on the detector for the 2 mm 150 planes configuration.

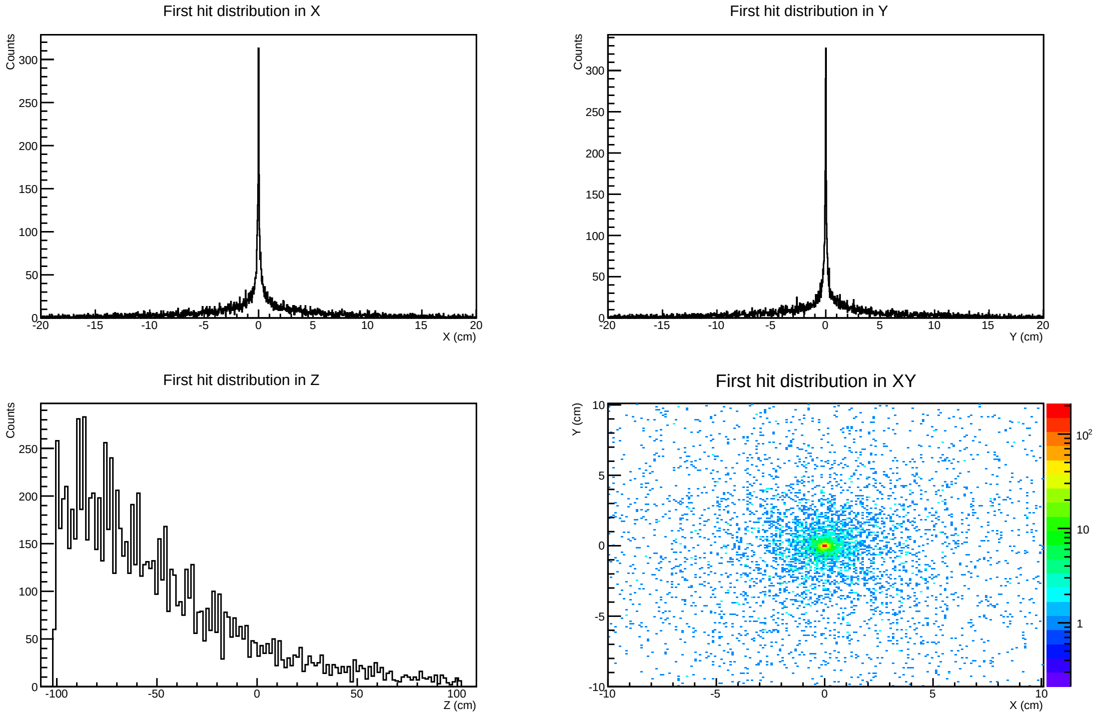

Figure A.19: Spacial distribution of the first hit on the detector for the 4 mm 75 planes configuration.

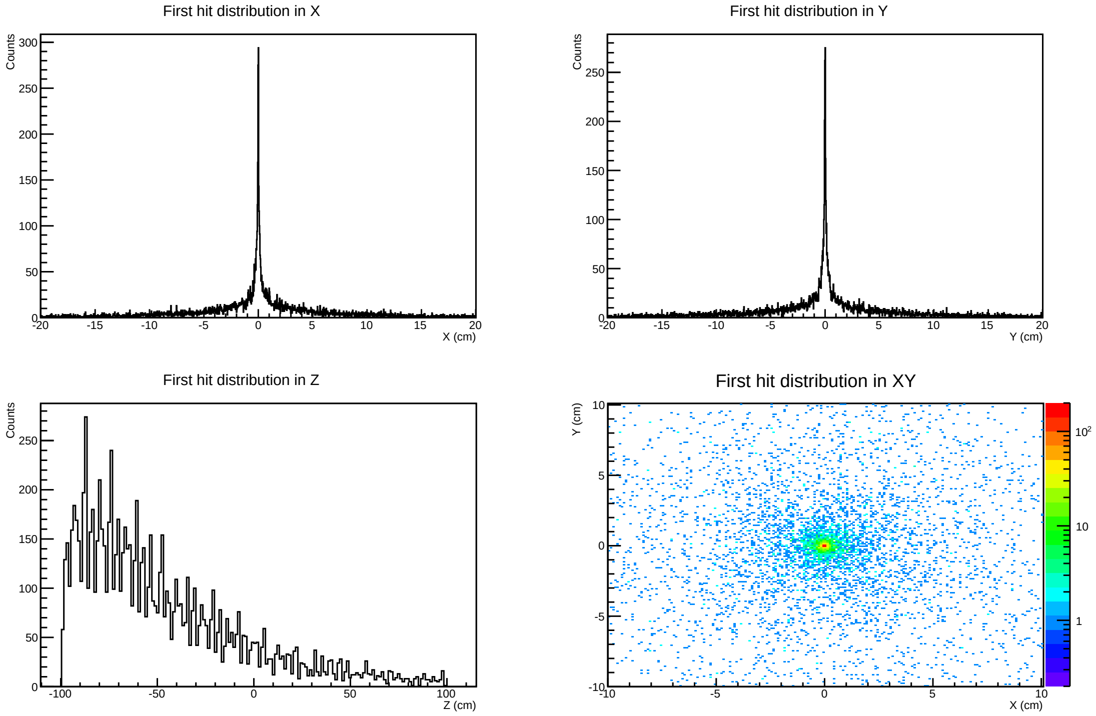

Figure A.20: Spacial distribution of the first hit on the detector for the 5 mm 60 planes configuration.

A.6 Gaps multiplicity for different number of incoming neutrons

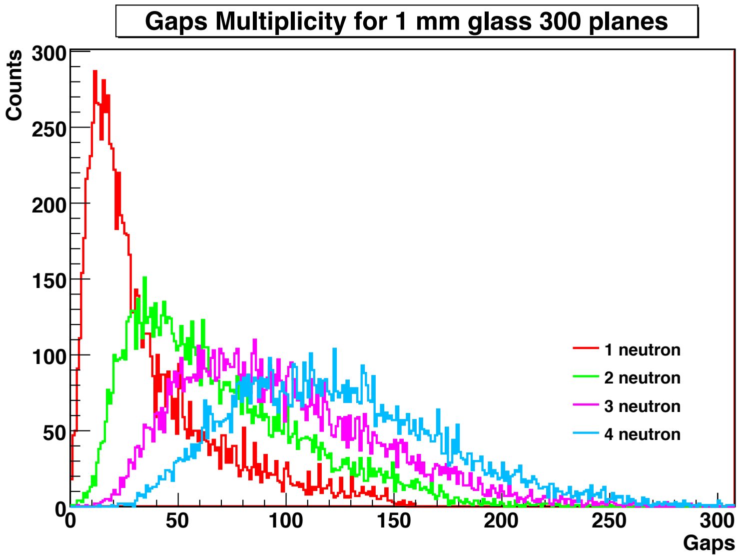

Figure A.21: Gaps multiplicity for the 1 mm 300 planes geometry for different number of incoming neutrons.

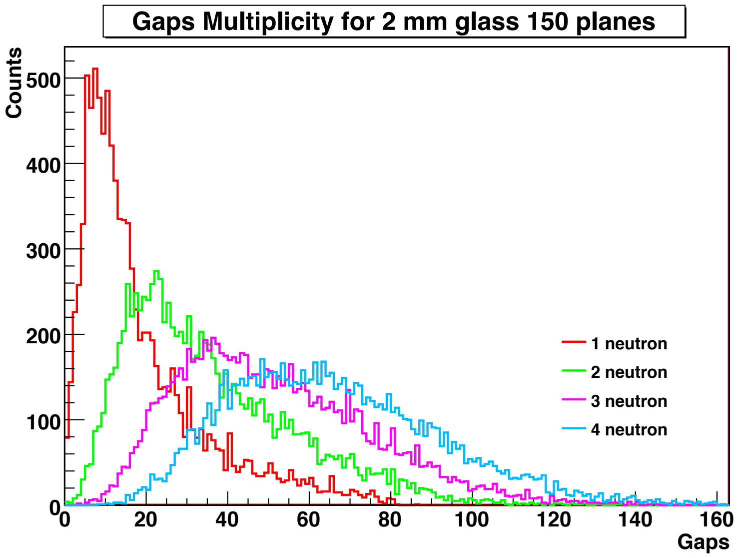

Figure A.22: Gaps multiplicity for the 2 mm 150 planes geometry for different number of incoming neutrons.

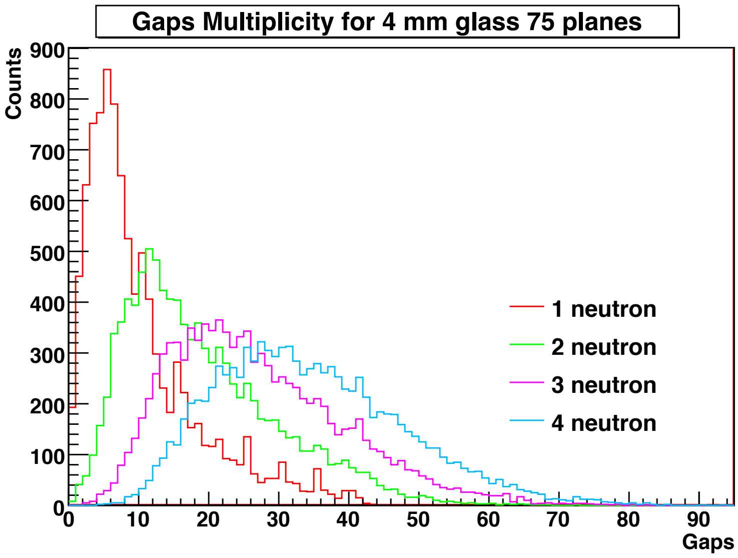

Figure A.23: Gaps multiplicity for the 4 mm 75 planes geometry for different number of incoming neutrons.

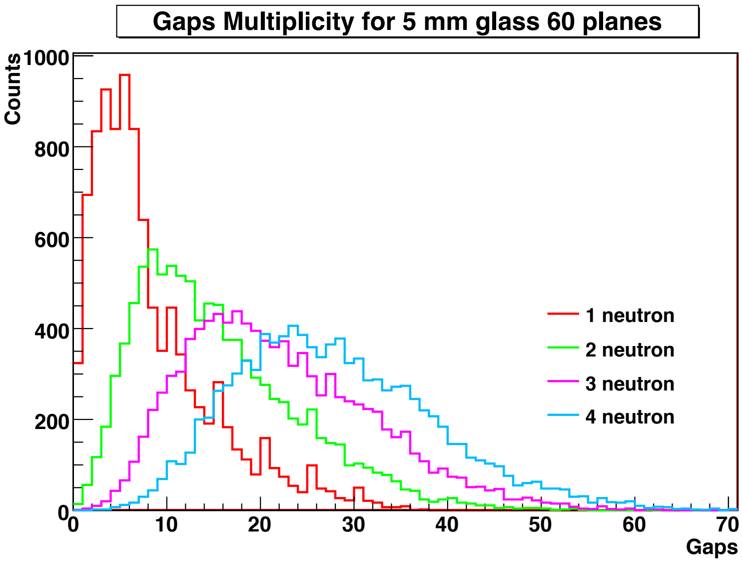

Figure A.24: Gaps multiplicity for the 3 mm 100 planes geometry for different number of incoming neutrons.

A.7 Plane multiplicity for different number of incoming neutrons

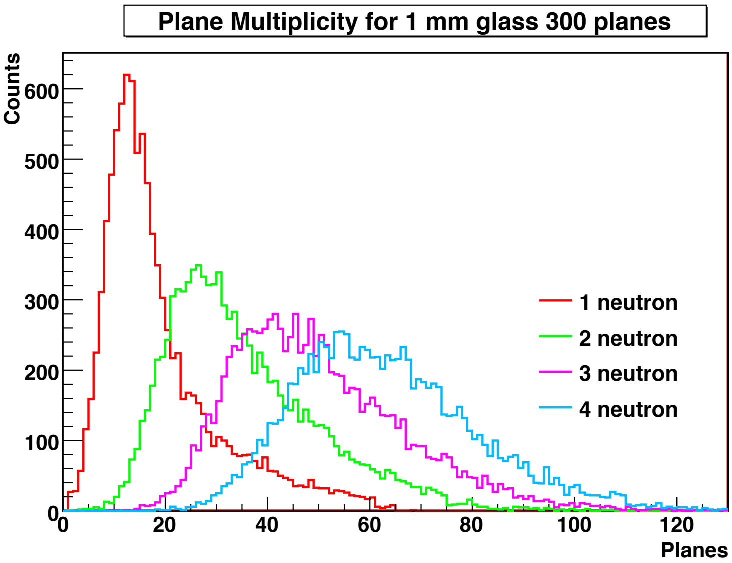

Figure A.25: Plane multiplicity for the 1 mm 300 planes geometry for different number of incoming neutrons.

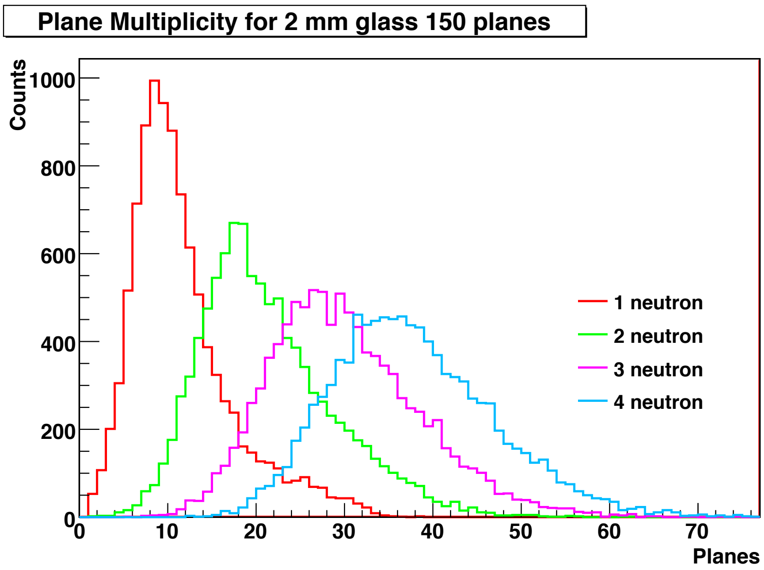

Figure A.26: Plane multiplicity for the 2 mm 150 planes geometry for different number of incoming neutrons.

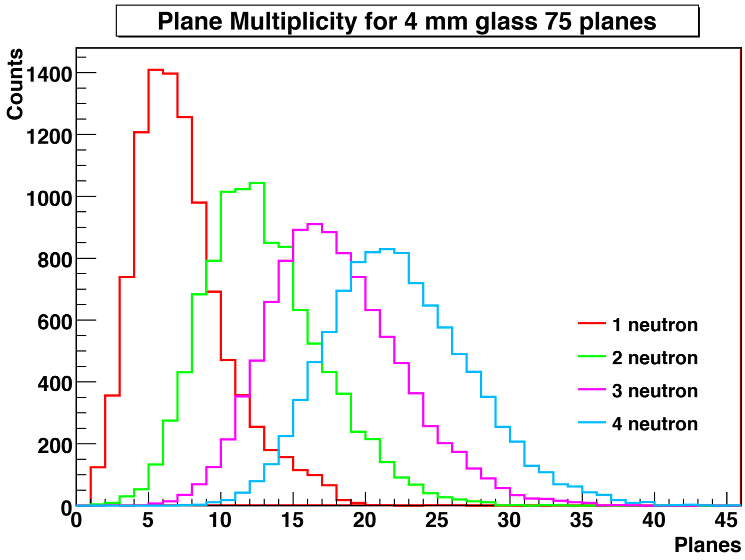

Figure A.27: Plane multiplicity for the 4 mm 75 planes geometry for different number of incoming neutrons.

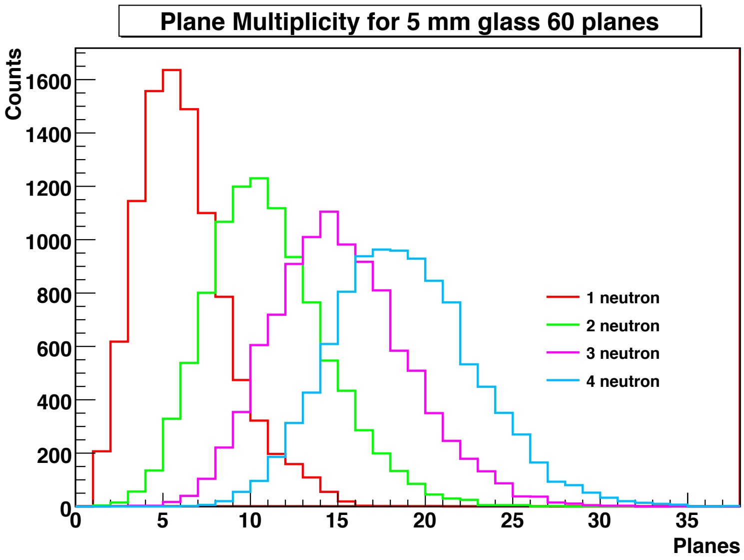

Figure A.28: Plane multiplicity for the 5 mm 60 planes geometry for different number of incoming neutrons.

A.8 Two planes multiplicity for different number of incoming neutrons

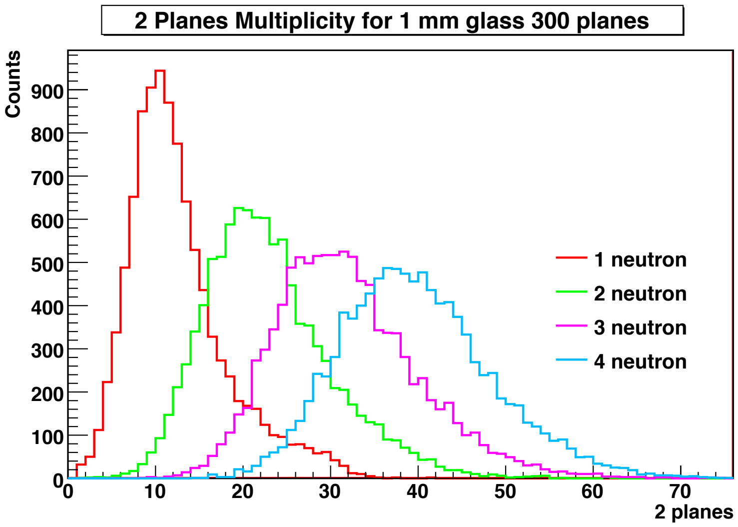

Figure A.29: Two plane multiplicity for the 1 mm 300 planes geometry for different number of incoming neutrons.

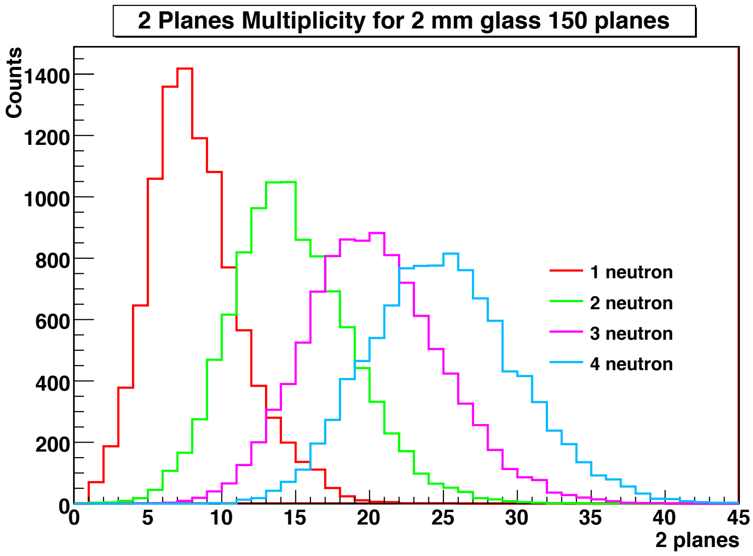

Figure A.30: Two plane multiplicity for the 2 mm 150 planes geometry for different number of incoming neutrons.

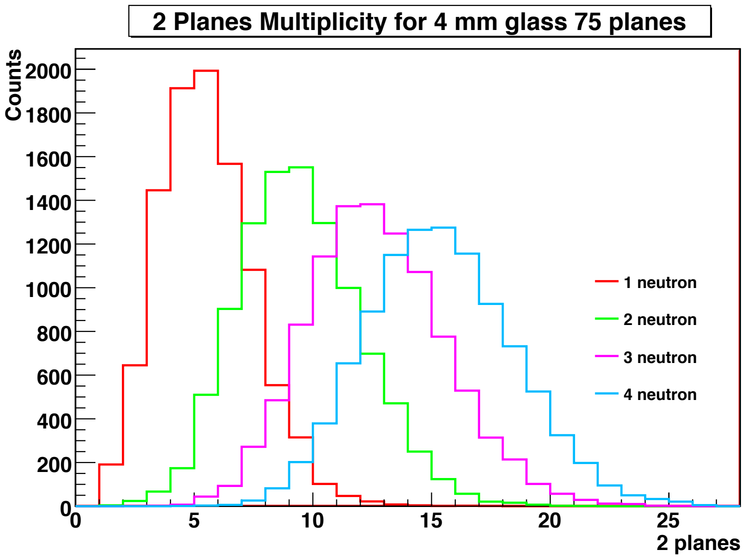

Figure A.31: Two plane multiplicity for the 1 mm 300 planes geometry for different number of incoming neutrons.

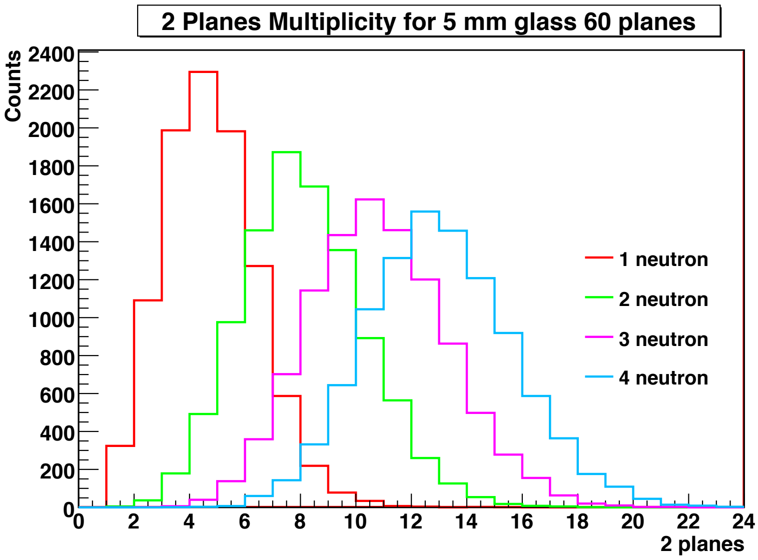

Figure A.32: Two plane multiplicity for the 5 mm 60 planes geometry for different number of incoming neutrons.

A.9 Linear regressions of the number of neutrons in function of the mean value of the multiplicity peak.

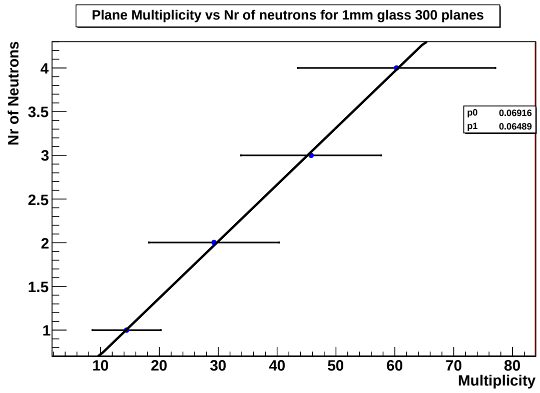

Figure A.33: Linear regression to the number of neutrons in function of the mean value of the plane multiplicity.

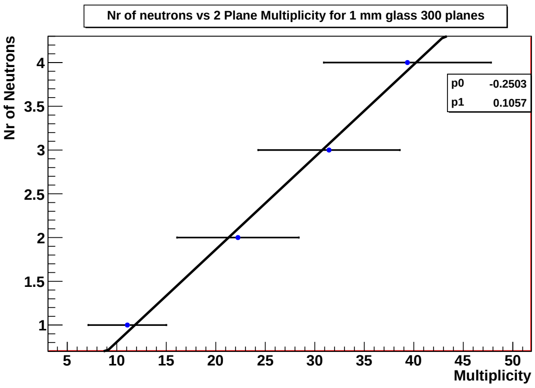

Figure A.34: Linear regression to the number of neutrons in function of the mean value of the two planes multiplicity.

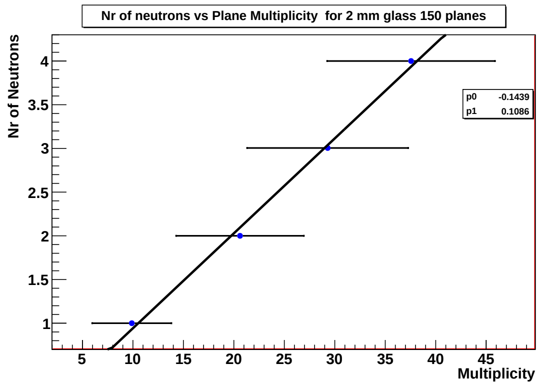

Figure A.35: Linear regression to the number of neutrons in function of the mean value of the plane multiplicity.

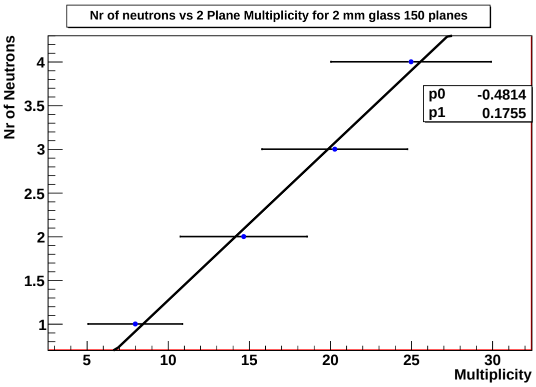

Figure A.36: Linear regression to the number of neutrons in function of the mean value of the two planes multiplicity.

A.9 Linear regressions of the number of neutrons in function of the mean value of the multiplicity peak.

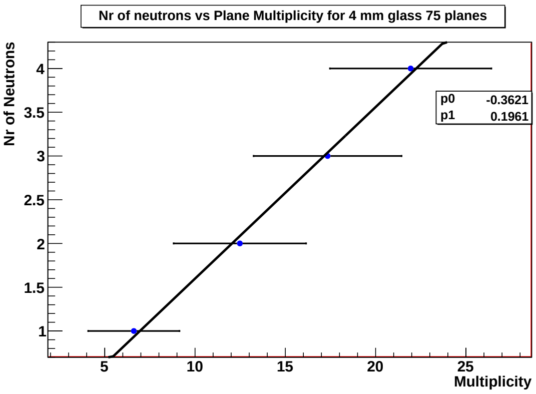

Figure A.37: Linear regression to the number of neutrons in function of the mean value of the plane multiplicity.

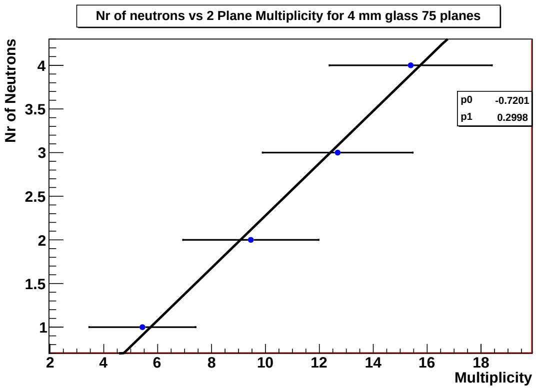

Figure A.38: Linear regression to the number of neutrons in function of the mean value of the two planes multiplicity.

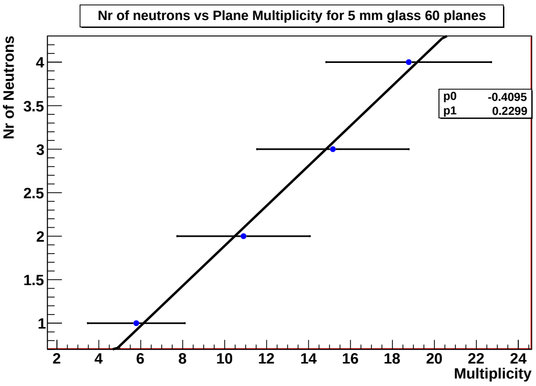

Figure A.39: Linear regression to the number of neutrons in function of the mean value of the plane multiplicity.

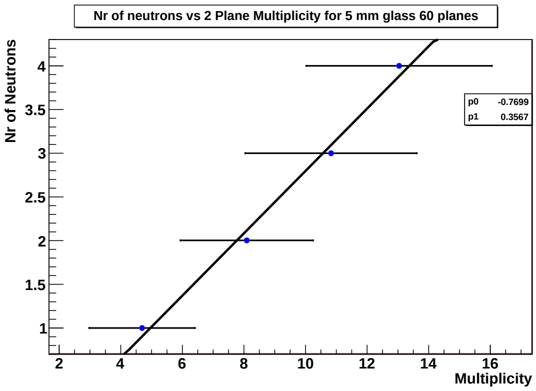

Figure A.40: Linear regression to the number of neutrons in function of the mean value of the two planes multiplicity.

A.10 Activated gaps per plane.

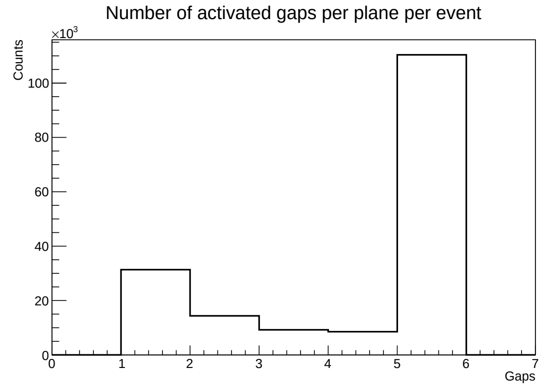

Figure A.41: Number of gas gaps activated per plane per event for the 1 mm glass 300 planes geometry.

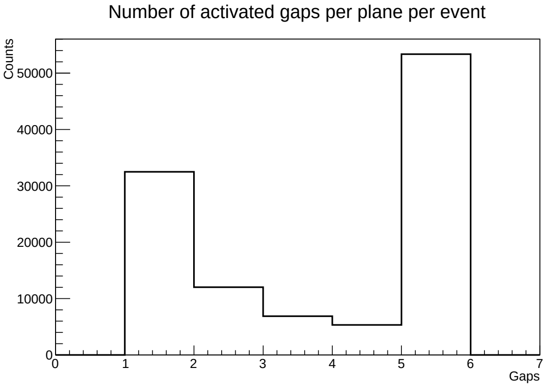

Figure A.42: Number of gas gaps activated per plane per event for the 2 mm glass 150 planes geometry.

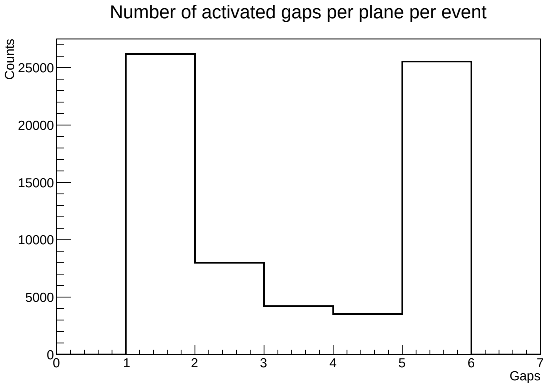

Figure A.43: Number of gas gaps activated per plane per event for the 4 mm glass 75 planes geometry.

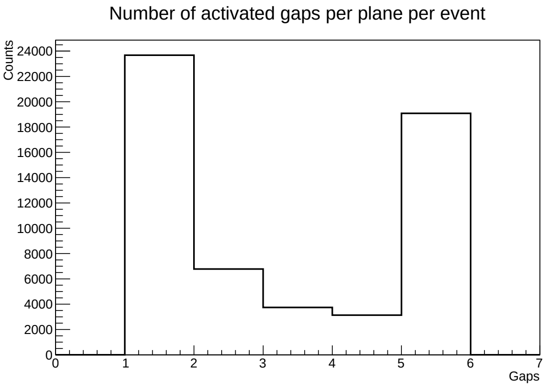

Figure A.44: Number of gas gaps activated per plane per event for the 5 mm glass 60 planes geometry.

A.11 Comparison of the two analysis choices for the momentum reconstruction of the neutron.

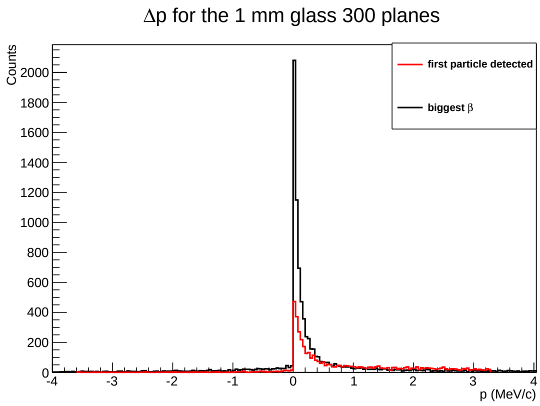

Figure A.45: Comparison of the analysis methods of the momentum reconstruction for the 1 mm glass 300 planes geometry.

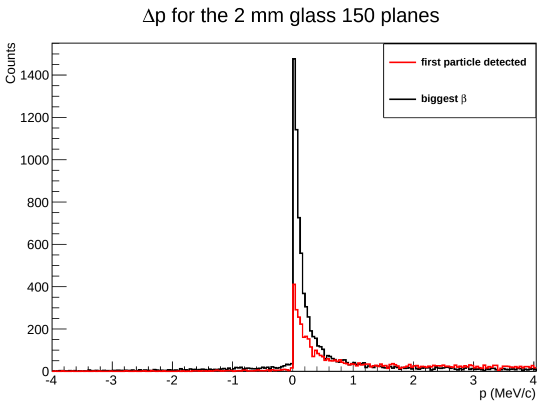

Figure A.46: Comparison of the analysis methods of the momentum reconstruction for the 2 mm glass 150 planes geometry.

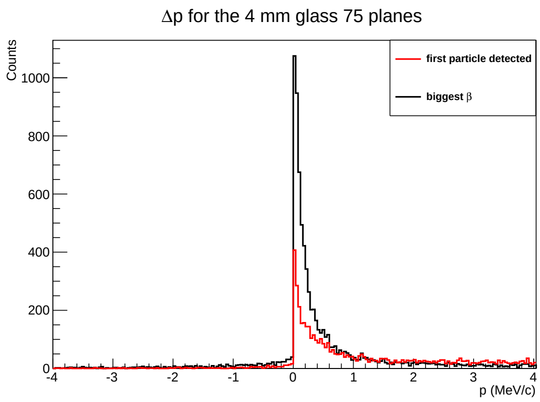

Figure A.47: Comparison of the analysis methods of the momentum reconstruction for the 4 mm glass 75 planes geometry.

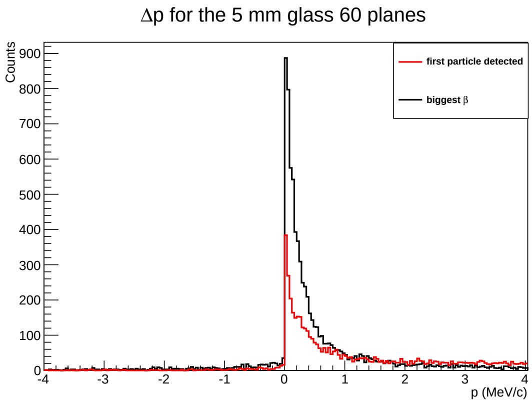

Figure A.48: Comparison of the analysis methods of the momentum reconstruction for the 5 mm glass 60 planes geometry.

Bibliography

[AKI-94] V. Akimov, A. Arefiev, A. Bizzeti, C. Civinini, E. Choumilov, R. D'Alessandro, A. Ferrando, Y. Kolotaev, S. Kuleshov, A. Malinin, A. Martemianov, L. Martinez-Laso, K. Mikhailov, V. Pojidaev, A. Rojkov, V. Serov, and A. Smirnitsky, "Ceramic ppc technology and performance," *Nuclear Instruments and Methods in Physics Research Section A: Accelerators, Spectrometers, Detectors and Associated Equipment*, vol. 344, no. 1, pp. 120 – 124, 1994. [Online]. Available: http://www.sciencedirect.com/science/article/pii/0168900294906580 32

[ALI-web] Alice software project webpage. [Online]. Available: http://aliceinfo.cern.ch/Offline/General-Information/User-Support.html 41

[ALT-10] Al-Turany, D. Bertini, R. Karabowicz, and F. Uhlig, "Status of the fair-root simulation and analysis framework," *GSI Annual Report*, 2010. 43

[BER-08] D. Bertini, M. Al-Turany, I. Koenig, and U. Florian, "The fair simulation and analysis framework," *Journal of Physics: Conference Series 119 032011*, 2008. 42

[BER-09] D. Bertini, "R3broot: a root based simulation and analysis framework for r3b," *GSI Annual Report*, 2009. 44

[BLAI-92] T. Blaich, T. Elze, H. Emling, H. Freiesleben, K. Grimm, W. Henning,

R. Holzmann, G. Ickert, J. Keller, H. Klingler *et al.*, “A large area detector for high-energy neutrons,” *Nuclear Instruments and Methods in Physics Research A*, vol. 314, pp. 136–154, 1992. 4

[BLA-02] A. Blanco, R. Ferreira-Marques, C. Finck, P. Fonte, A. Gobbi, A. Policarpo, and M. Rozas, “A large area timing rpc,” *Nuclear Instruments and Methods in Physics Research Section A: Accelerators, Spectrometers, Detectors and Associated Equipment*, vol. 485, no. 3, pp. 328–342, 2002. 35, 37

[BLA-03] A. Blanco, P. Fonte, L. Lopes, A. Mangiarotti, R. Ferreira-Marques, and A. Policarpo, “Resistive plate chambers for time-of-flight measurements,” *Nuclear Instruments and Methods in Physics Research Section A: Accelerators, Spectrometers, Detectors and Associated Equipment*, vol. 513, no. 1-2, pp. 8 – 12, 2003, lt;ce:title¿Proceedings of the 6th International Conference on Position-Sensitive Detectorslt;/ce:title¿. [Online]. Available: http://www.sciencedirect.com/science/article/pii/S0168900203021260 36

[BAT-07] P. S. F. C. A. F. R. S. G. Battistoni, S. Muraro, A. Fasso, and J. Ranft, “The fluka code: Description and benchmarking,” *AIP Conference Proceeding*, vol. 896, pp. 31–49, 2007. 45

[BOR-10] K. Boretzky, “Characterization of neuland prototypes and the land detector using fast “monoenergetic” neutrons,” *proposal for SIS experiment S406, unpublished*, 2010. 105, 107

[CAL-web] Calor website. [Online]. Available: http://www-rsicc.ornl.gov/codes/ccc/ccc6/ccc-610.html 45

[CHA-32] J. Chadwick, “Possible existence of a neutron,” *Nature*, vol. 129, no. 312, p. 1949, 1932. 11

[CHA-91] G. Charpak, P. Fonte, V. Peskov, F. Sauli, D. Scigocki, and D. Stuart, “Investigation of operation of a parallel-plate avalanche chamber with a csi photocathode under high gain conditions,” *Nuclear Instruments and Methods in Physics Research Section A: Accelerators, Spectrometers, Detectors and Associated Equipment*, vol. 307, no. 1, pp. 63 – 68, 1991. [Online]. Available: http://www.sciencedirect.com/science/article/pii/0168900291901319 32

[R3B-05] T. R. collaboration, “Technical proposal for the design, construction, commissioning and operation of r^3b,” GSI, Tech. Rep., 2005. 7, 9, 38

[CAR-88] R. Cardarelli, R. Santonico, A. Di Biagio, and A. Lucci, “Progress in resistive plate counters,” *Nuclear Instruments and Methods in Physics Research Section A: Accelerators, Spectrometers, Detectors and Associated Equipment*, vol. 263, no. 1, pp. 20–25, 1988. 33

[CAP-94] A. Capella, U. Sukhatme, C. Tan, and J. Tran Thanh Van, “Dual parton model,” *Physics Reports*, vol. 236, no. 4-5, pp. 225–329, 1994. 46

[CER-96] E. Cerron Zeballos, I. Crotty, D. Hatzifotiadou, J. Lamas Valverde, S. Neupane, M. Williams, and A. Zichichi, “A new type of resistive plate chamber: the multigap rpc,” *Nuclear Instruments and Methods in Physics Research Section A: Accelerators, Spectrometers, Detectors and Associated Equipment*, vol. 374, no. 1, pp. 132–135, 1996. 34, 35

[DAV-73] A. Davies and C. Evans, “Theory of ionization growth in gases under pulsed and static fields,” 1973. 28

[EID-04] S. Eidelman, K. Hayes, K. Olive, M. Aguilar-Benitez, C. Amsler, D. Asner, K. Babu, R. Barnett, J. Beringer, and P. Burchat, "Review of particle physics," *Physics Letters. B*, vol. 592, 2004. 20

[FAI-web] Fair website. [Online]. Available: http://www.fair-center.de/ 1, 3

[FAR-web] Fairroot framework website. [Online]. Available: http://fairroot.gsi.de/ 41

[FON-00a] P. Fonte, R. Ferreira Marques, J. Pinhão, N. Carolino, and A. Policarpo, "High-resolution rpcs for large tof systems," *Nuclear Instruments and Methods in Physics Research Section A: Accelerators, Spectrometers, Detectors and Associated Equipment*, vol. 449, no. 1-2, pp. 295–301, 2000. 35

[FON-00b] P. Fonte, A. Smirnitski, and M. Williams, "A new high-resolution tof technology," *Nuclear Instruments and Methods in Physics Research Section A: Accelerators, Spectrometers, Detectors and Associated Equipment*, vol. 443, no. 1, pp. 201–204, 2000. 35

[FON-02] P. Fonte, "Applications and new developments in resistive plate chambers," *Nuclear Science, IEEE Transactions on*, vol. 49, no. 3, pp. 881–887, 2002. 34

[FON-11] P. Fonte, A. Blanco, L. Lopes, and R. Marques, "Private comunication." 57, 59, 61, 62, 70, 76, 79, 101

[FLU-web] Fluka website. [Online]. Available: http://www.fluka.org/fluka.php 41

[FRS-web] Frs website. [Online]. Available: http://www-wnt.gsi.de/frs/index.asp 3

[GEA-web] Geant detector description and simulation tool. [Online]. Available: http://wwwasd.web.cern.ch/wwwasd/geant/ 41

[GEA4-web] Geant4 website. [Online]. Available: http://geant4.cern.ch/ 41

[GCA-web] The gcalor website. [Online]. Available: http://www.atlas.uni-wuppertal.de/zeitnitz/gcalor 45

[GRU-96] C. Grupen, *Particle Detectors.* Cambrish University Press, 1996. 24

[GSI-web] Gsi website. [Online]. Available: http://www.gsi.de/ 1, 2, 3

[HAG-02] K. Hagiwara, "Review of particle physics," *Physical Review D*, p. 66:1, 2002. 22, 23

[HRI-03] I. Hrivnacova, D. Adamova, V. Berejnoi, R. Brun, F. Carminati, A. Fasso, E. Futo, A. Gheata, I. G. Caballero, A. Morsch, and A. Collaboration, "The virtual monte carlo," 2003. [Online]. Available: http://arxiv.org/abs/cs/0306005v1 41

[JOH-88] J. Johnson and T. Gabriel, "A user's guide to micap: A monte carlo ionization chamber analysis package," Tech. Rep., 1988. 45

[KEU-48] J. Keuffel, "Parallel-plate counters and the measurement of very small time intervals," *Phys. Rev*, vol. 73, p. 531, 1948. 30

[LIP-web] Lip-coimbra's websit. [Online]. Available: http://coimbra.lip.pt/index.php 59

[MEE-78] J. Meek and J. Craggs, "Electrical breakdown of gases," 1978. 29

[NEU-rep] N. W. Group, "A high-resolution time-of-flight spectrometer for high-energy neutrons at r3b a high-resolution time-of-flight spectrometer for high-energy neutrons at r^{3}b - neuland," GSI, Tech. Rep. 6, 9, 37, 39

[PAL-75] V. Palladino and B. Sadoulet, “Application of classical theory of electrons in gases to drift proportional chambers,” *Nuclear Instruments and Methods*, vol. 128, no. 2, pp. 323–335, 1975. 27, 28

[PAR-71] V. Parkhomchuck, Y. Pestov, and N. Petrovykh, “A spark counter with large area,” *Nuclear Instruments and Methods*, vol. 93, no. 2, pp. 269–270, 1971. 31

[PES-98] Y. Pestov, “Timing below 100 ps with spark counters: Work principle and applications,” *Ric. Sci. Educ. Perm*, vol. 112, pp. 604–621, 1998. 31

[R3B-web] R3b website. [Online]. Available: http://www.gsi.de/forschung/kp/kr/R3B_e.html 6

[ROO-web] Root system website. [Online]. Available: http://root.cern.ch 41

[SAN-81] R. Santonico and R. Cardarelli, “Development of resistive plate counters,” *Nuclear Instruments and Methods in physics research*, vol. 187, no. 2-3, pp. 377–380, 1981. 19

[SAU-77] F. Sauli, *Principles of operation of multiwire proportional and drift chambers.* Cern, 1977, vol. 77, no. 09. 27

[SCH-78] G. Schultz and J. Gresser, “A study of transport coefficients of electrons in some gases used in proportional and drift chambers,” *Nuclear Instruments and Methods*, vol. 151, no. 3, pp. 413 – 431, 1978. [Online]. Available: http://www.sciencedirect.com/science/article/pii/0029554X78901519 27

[SUP-web] Super-frs website. [Online]. Available: https://www.gsi.de/forschung/fair_experiments/superfrs/ 3

[TOW-10] J. Townsend and S. Townsend, *The theory of ionization of gases by collision.* Constable & Company, ltd., 1910. 25

[TUR-07] J. Turner, *Atoms, radiation, and radiation protection.* Vch Pub, 2007. 13, 14

[YAO-06a] W. Yao *et al.*, “Review of particle physics,” *Journal of Physics G: Nuclear and Particle Physics*, vol. 33, p. 1, 2006. 12

[YAO-06b] W. Yao, C. Amsler, D. Asner, R. Barnett, J. Beringer, P. Burchat, C. Carone, C. Caso, O. Dahl *et al.*, “Particle data group,” *J. Phys. G*, vol. 33, no. 1, p. 164, 2006. 12